Measurement of a solid-state triple point at the metal-insulator transition in vanadium dioxide

Jae Hyung Park

A dissertation

submitted in partial fulfillment of the

requirements for the degree of

Doctor of Philosophy

University of Washington

2014

Reading Committee:

David H Cobden, Chair

Xiaodong Xu

Anton Andreev

Program Authorized to Offer Degree:

Physics

University of Washington

Abstract

Measurement of a solid-state triple point at
the metal-insulator transition in vanadium dioxide

Jae H Park

Chair of the Supervisory Committee:
Professor David H Cobden
Department of Physics

The first-ever accurate measurement of a solid-state triple point in vanadium dioxide (VO_2) was made by performing simultaneous optical and transport measurements on a purpose-built nanomechanical strain apparatus that actively controls the length of a single nanobeam with a nanometer precision. The nature of the metal-insulator transition (MIT) in VO_2 remains unsettled due to the presence of more than one insulating phase near the transition point, an observation that neither Mott nor Peierls picture of the transition suffices to explain. The triple point in VO_2, which has not been located, is a key to constructing its intrinsic phase diagram, a fundamental ingredient in the analysis and interpretation of any study of the MIT. The

striking result is that the triple point precisely is where the MIT occurs at zero stress. While the implication of the new findings is unclear, there is a little doubt they will be crucial ingredients to the correct theory of the MIT. The value and importance of working with a single-domain nanocrystal while actively applying controlled strain have been demonstrated. This approach to studying the phase transition may serve as an indispensable tool, a new paradigm, for mastering the physics of complicated phenomena in strongly correlated materials where strain plays a key role.

Table of Contents

List of Figures

List of Tables

Acknowledgements

As I reflect on my progress as a PhD student, I am at a loss of words at the sheer quality of many individuals I had the privilege of working with. It is my great pleasure to thank those, without whom this work would not have been completed.

Of course, it begins with Dave. The fact that Dave has endured me for the past six years speaks volumes about his patience and gentleness. I especially appreciated his candid approach to dealing with all sorts of things from my progress as a researcher to the problems in our experiments. Though he is a great scientist full of new ideas, he treats his graduate students as his colleagues, allowing the kind of intellectual space and freedom for ventures that is becoming a lost art in this fast-paced era of result-orientated research. More than anything, his constant pursuit of new ideas and uncompromising attention to important details has been infectious and instrumental in my graduate development.

I wish to express my gratitude for the kindness of Jiang Wei and Zenghui Wang, who welcomed me into the group and showed me a great deal on how experiments are conducted. I am deeply indebted to Jiang, who passed me the VO_2 torch and taught me all aspects of the project when I was a newbie. I will miss all my dear fellow Cobdenites: Serkan always gets the job done and is hard at work. Hao-Chun gave me more laughs than I could handle. Boris and I had so much fun exploring all sorts of cuisines. Zaiyao, remember me when you become famous. Jim deserves a special mention because I could not have completed the strain setup without his assistance.

Chunming really should have worked in the Pacific Time zone instead of the China Time zone. Gosh, I never imagined going to the lab each day would be so much fun. It was because of those guys.

Shout out to the guys in Professor Xu's group, some of the hardest-working people I have met. I should not forget to mention a number of undergraduate students who were involved in our group: Jacob, Vinny, Erik, Nick, Eli, Brad, Joe, Denise, John, and Paul. Again, remember me when you become famous. Special thanks to Eric the glass shop guy, who not only blows glass but blows my mind with his diverse experimental expertise.

I want to acknowledge all the members of my church, young and old. What a joy it has been to have my life shaped by a community of love and sincerity. I will cherish those moments of serving homeless with food at the Seattle downtown, our trips to Neah Bay and Taholah for summer VBS, and countless hours we spent together as we planned our future and wondered what would become of us. You helped me see a bigger picture and understand how much joy there is in giving and sharing my possessions without reserve.

Finally, I pour out my warmest and dearest thanks to my wonderful family. My wife, Alicia, has been so good to me always. Ty (4) and Noelle (2), I hope you would one day understand how much rest and peace I got simply by staring into your eyes. No day's work was too stressful when I could come home to this family. Of course, special thanks to my parents and in-laws for your unconditional support. #3 is coming.

Psalm 92:5

1 Introduction

1.1 Strongly correlated electron system

The overarching theme of condensed matter physics is that of emergent phenomena.[1] In other words, taking a reductionist approach to understanding a system of *N* particles, where *N* is a very large number, is quite difficult to say the least. Solving the equation of motion for the *N* particles is an insurmountable task and, even if solved, it is doubtful the answer would be of any utility. But somehow, and quite fortunately, a set of macroscopic laws or observables emerges that allows a simple, tenable description of the system despite the quite complex nature of interactions among its constituents and their microscopic details. Much of the condensed matter physics is endeavored with an attempt to link the macroscopic manifestations of a complex system to the microscopic properties of its parts. Though not always successful, this endeavor has been exemplified in the description of simple metal, insulator, and semiconductor. The main assumption is that an electron, the most active participant and important player in their properties, does not interact with another electron. Put another way, the possibility of the electron-electron (e-e) interaction as an origin of the system's macroscopic observables is completely neglected. At first this sounds outrageous because a typical metal is packed with a density of about 10^{23} electrons per cm^3, meaning the distance between neighboring two electrons is on the order of an angstrom. A rough estimate of the coulomb energy, $e^2/(1\ \text{Å})$, gives an order of a few eV, which is comparable to the Fermi energy of the electron, which seems to contradict the assumption that the electrostatic interaction may be negligible. In short, the justifications for the seemingly outrageous

assumption, without delving into the full rigors of the Fermi liquid theory, owe to the Pauli exclusion principle and adiabatic mapping from Fermi gas to the Fermi liquid of quasi-particles. A theory that neglects the e-e interaction explicitly is known as single electron theory. It starts by writing down the hamiltonian of a single electron in the absence of all other electrons and, once that has been solved, the macroscopic observables, such as electrical conductivity and heat capacity, are expressed in terms of the properties of a single electron such as its mass, momentum, and charge. Furthermore, solving the energy spectrum of a single electron in the absence of the e-e interaction is much more feasible calculation. What has been astonishing in the past decade is the number of observations in the condensed matter systems that exhibit the excitation spectrums reminiscent of the particles in high energy physics such as Dirac[2], Majorana[3], and Higgs[4]. Moreover, the field is even richer with systems that cannot be described on the basis of a single electron theory. Those systems are termed strongly correlated electron systems (SCES), meaning the e-e interaction cannot be ignored. In fact, the e-e interaction is strong in the sense that any perturbation theory is not applicable and only approximate methods to analyzing these systems exist that tend to be either too simplified to capture the essence or too complex to yield insightful solutions. The theoretical works, mostly numerical, in these systems are almost always *a posteriori* and highly dependent on the set of assumptions one starts with. It is the reason why the field is heavily reliant upon new experimental findings to discover and master the physics behind SCES phenomena such as high-T_c superconductivity[5], metal insulator transitions[6], heavy fermion physics[7], and quantum phase transitions[8]. Among those phenomena, the metal-insulator transition[9] (MIT) in vanadium dioxide (VO_2) is one of the

oldest, dating back to 1959, and the nature of MIT remains unsettled despite more than five decades of study.

1.2 Vanadium dioxide

There are several reasons why VO_2 may serve as a paradigmatic material for studying the SCES. VO_2 is arguably the simplest SCES in terms of chemical composition (binary compound), crystal structure (rutile and monoclinic), and electronic configuration ($3d^1$). This simplicity is likely to yield an easier analysis and more straightforward interpretation of the experimental results. The MIT in VO_2, however, presents a number of experimental challenges. In the past, taking a systematic approach to studying VO_2 was difficult due to the irreproducibility associated with the first-order nature of the transition, which resulted in cracking and ferroelastic domains when the crystal symmetry is reduced. But the availability of high quality VO_2 nanocrystals smaller than the characteristic domain size, the stability and robustness of the nanocrystals in the ambient condition, and the ease of synthesis alleviate those difficulties of studying the transition greatly. (chapter 2 & 3) The fact that MIT is readily accessible slightly above the room temperature makes the experimentation simpler. (Chapter 4) In these VO_2 nanobeams, the phase composition can be completely identified and controlled with high reproducibility (Chapter 5), something that was impossible for the bulk counterpart. Consequently the effects that originate from the domain structure, and hence the non-uniformity of strain and phase composition in the bulk crystals, can be avoided completely in order to infer the intrinsic properties. It is no surprise that the availability of VO_2 nanocrystals[10] since 2005 has led to a quite resurgence in the study of VO_2 and its MIT as shown on figure 1-1.

A number of new aspects have been discovered in the past decade but the nature of MIT is an unsettled because of the incapability of either Mott or Peierls picture to fully explain the existence of more than one insulating phase that are involved at the MIT. Therefore, an understanding of the relationship between different phases is a crucial ingredient to the correct theory of the MIT.

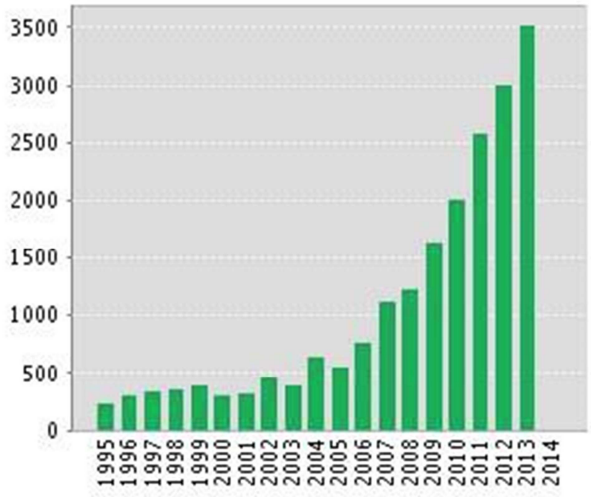

Figure 1-1 Citation number of the Morin's paper versus year. The citation number in each year is plotted from 1995 to 2013. There is a sharp increase after 2005, when the first synthesis of VO_2 nanocrystals was reported. (Figure courtesy of Web of Science)

1.3 Thesis summary

The metal-insulator transition (MIT) in VO_2 is accompanied by a large and rapid change in the conductivity[11] and optical properties[12,13], with potential uses in switching[14] and sensing[15]. VO_2 has recently received renewed attention as a convenient strongly correlated material for the application of new ultrafast[16,17,18] and microscopy[19,20] techniques, ionic gating[21], and

improved computational approaches[22,23]. However, the problems associated with bulk or film samples that consist of a complex of multiple solid phases and domains under highly nonuniform strain, as well as compositional variations such as oxygen vacancies[24] and hydrogen doping[25], make it almost impossible to disentangle the underlying parameters on which rigorous understanding can be built. The experiments described in this work eliminate these problems, allowing unprecedented control of the MIT and accurate determination of the underlying phase stability diagram of pure VO_2 near its triple point for the first time.

2 Background

Comprehensive reviews of the studies performed on VO_2 are available elsewhere[6,26,27,28,29,30]. A brief history of VO_2 studies is discussed first, with emphasis on the distinct phases in the system and their crystal structure. (section 2.1) Next, general remarks are made about the difficulties of studying the solids that undergo first-order phase transition. (section 2.2) Those difficulties are mostly absent in high-purity VO_2 nanocrystals that have been synthesized in the past decade. (section 2.3) The nanocrystals of VO_2, when suspended, provide a unique situation, coexistence (section 2.4) that can be exploited to tune the phase transition. A general review of phase diagram (section 2.5) is followed by a brief literature survey of the phase diagrams in VO_2. Finally our approach to constructing a VO_2 phase stability diagram with high precision is discussed. (section 2.6)

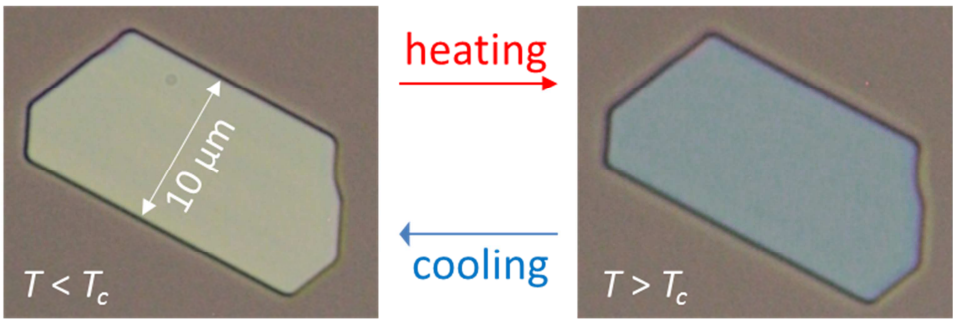

Figure 2-1 Microscope image of a VO_2 crystal before and after the metal-insulator transition. The metal-insulator transition in VO_2 can be easily identified under a microscope because of the sudden change in color. The above sample was prepared by transferring a VO_2 crystal to a sapphire substrate on which the crystal sits loosely. If there is a significant adhesion or friction between the sample and substrate, the transition may develop a domain structure, which is discussed in section 2.2 and 2.4.

2.1 Phases in VO_2

Structural analysis of VO_2 began as early 1954 before the discovery of the MIT by Andersson[31] who performed the powder x-ray diffraction on various stoichiometric vanadium oxides before the discovery of the MIT. In 1959 Morin at the Bell Labs discovered a number of oxides which showed MIT[9] and, among them, VO_2 has been noted for its transition temperature T_c slightly above the room temperature. Soon after the discovery, it was established that high-temperature VO_2 is metallic with the rutile ($P4_2/mnm$) structure while low-temperature VO_2 is insulating with the monoclinic ($P2_1/c$) structure. The different crystal structure systems are shown in figure 2-2 with the respective unit cell and primitive vectors.

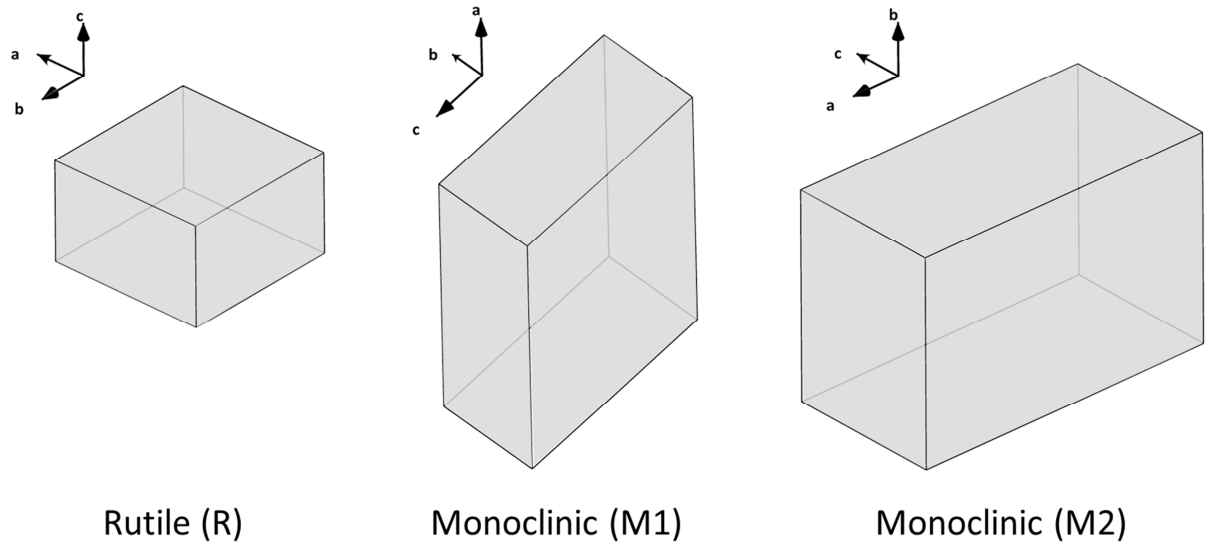

Figure 2-2 Respective unit cell of the different phases in VO_2. R is metallic while M1 and M2 are insulating. In each unit cell, R has two vanadium atoms, M1 four, and M2 eight. The primitive vectors are denoted by a, b, and c. The directions along the vanadium chain axis are c_R, a_{M1}, and b_{M2}, also known as the pseudo-rutile c axis direction.

In 1969 MacChesney and Guggenheim reported their extensive results on introducing a small concentration of various impurity ions into the single crystals of VO_2, though not for the first time, in an attempt to observe a systematic change affecting the transition due to the modified the charge carrier concentration[32]. This sparked a series of studies on the doped VO_2 crystals. In 1971 Villeneuve et al reported the results of the x-ray diffraction on $V_{1-x}Cr_xO_2$ solid solution[33]. In 1972 Marezio et al discovered distinct insulating phases of monoclinic structures, which he denoted M1, M2, and M3, in Cr-doped VO_2 single crystals[34]. In 1973 Villeneuve et al corrected M3 as having the triclinic (T) structure[35]. In 1975, Pouget et al observed M2 and T in pure VO_2 crystals by applying uniaxial pressure along the $[110]_R$[36].

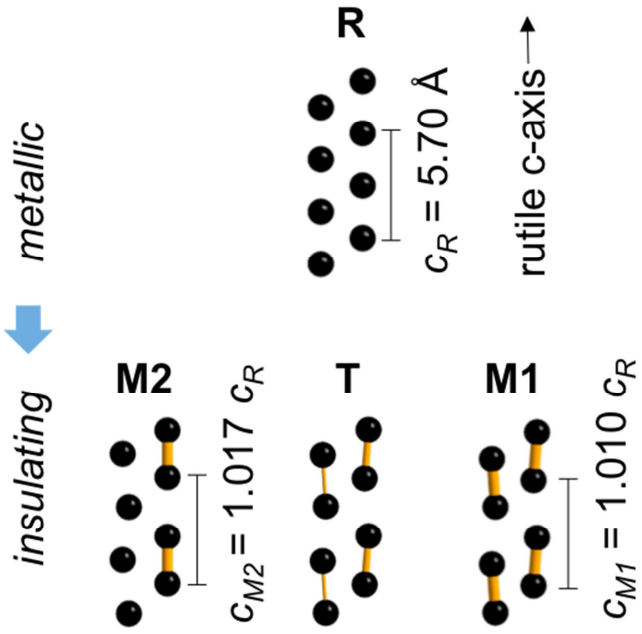

Figure 2-3 Different phases and their crystal structure. A simplified view of the crystal structures in different phases of VO_2 is illustrated. It is noted that the lattice constant along the rutile c axis, or the vanadium chain axis, experiences as large as 1.7% elongation due to the structural phase transition from R to M2.

Figure 2-3 illustrates a simplified illustration of the structures of the phases involved in the MIT. In every phase there are two interpenetrating sets of parallel chains of vanadium atoms each surrounded by six oxygen atoms forming a distorted octahedron (the oxygen atoms are not shown). As shown in figure 2-3, we defined $c_{\mathrm{R}} \equiv 2\mathrm{c}_{\mathrm{R}}, c_{\mathrm{M1}} \equiv \mathrm{a}_{\mathrm{M1}}, c_{\mathrm{M2}} \equiv \mathrm{b}_{\mathrm{M2}}$ for more direct comparisons of the fractional change in the lattice constant along the vanadium chain axis between the three phases. (see the caption, figure 2-2) Their numerical values were chosen based on the proximity of the x-ray measurement temperature to the T_c. (see Table 2-1) The largest difference in unit cell shape between R, M1 and M2 is along the pseudo-rutile *c* axis (the vanadium chain axis), with $c_{\mathrm{R}} = 5.700$ Å, $c_{\mathrm{M1}} = 5.755$ Å, and $c_{\mathrm{M2}} = 5.797$ Å, as indicated in figure 2-3. Compressive strain along this axis in an epitaxial film can lower the transition to room temperature[24,37], and thus applying uniaxial tensile stress P_c along it can be used to control the transition[37,38].

Year	Author	M1 c_{M1} (Å)	M2 c_{M2} (Å)	Rutile $c_R/2$ (Å)	Note
1956	Andersson	5.743 (21 °C)			
1970	Longo	5.7517 (25 °C)			
1971	Villeneuve			2.862 (>116.85 °C)	10 % Cr
1972	Marezio		5.7970 (<71.85°C)	2.8537(>71.85 °C)	2.4 % Cr
1974	McWhan			2.8514 (86.85 °C)	
1977	Ghedira		5.8 (38-73 °C)	2.8528 (73 °C)	1.5 % Al
1979	Kucharczyk	5.75488 (64.75°C)		2.84944 (65.05 °C)	

Table 2-1 X-ray measurements of the lattice constants in different phases. Only the lattice constants along the pseudo-rutile c axis are shown for their relevance to our work.

The electron configurations of a vanadium atom and an oxygen atom are respectively [Ar] $4s^2$ $3d^3$ and [He] $2s^2$ $2p^4$. The oxidation state of vanadium in VO_2 is four (IV) and each vanadium atom loses a total of four valence electrons to a pair of oxygen atoms. This ionic description, in which each vanadium atom is left with a $3d^1$ electron, forms the basis of its molecular orbital description[39]. In the high-temperature metallic (rutile, R) phase all the chains are straight and periodic, whereas in the low-temperature insulating (monoclinic, M1) phase every chain is dimerized, suggestive of the Peierls instability. In this view, the energy gap arises from the splitting between the bonding and anti-bonding of the V-V dimers. But as mentioned, there are also two other known insulating phases: monoclinic M2, in which only one set of chains is dimerized; and triclinic T, which is intermediate between M1 and M2. In view of the other insulating phases, Mott in 1975 stressed the importance of the Hubbard correlation energy in formation of the gap[28]. The existence of both M1 and M2, with similar dielectric yet different magnetic properties, provides constraints on the theory of the MIT; for example, it rules out a purely Peierls-type mechanism[40]. In the older literature the MIT is taken to occur between R and M1, although recent studies[20,41,42,43] have shown that M2 domains occur in most VO_2 samples near the MIT, raising the question of its role in the transition. The theoretical description of the MIT in VO_2 has a long, unsettled history[39, 40,44,45] due to the extent to which one should emphasize either the electron-phonon or the electron-electron interaction although both may play a significant role in the transition[22,46,47,48].

2.2 Complexities of the first-order phase transition in solids

A spontaneous formation of ferroelastic domains[49] in VO_2 is a direct consequence of the symmetry lowering structural phase transition, leading to a domain structure[50]. This is quite analogous to the spontaneous formation of ferromagnetic domains below the Curie temperature. Presence of domain structure is a recipe for disaster during the transition as the abrupt change in the crystal symmetry as well as its volume builds non-uniform internal stresses within a crystal that may be large enough to break itself. Many authors have expressed the difficulties of working with VO_2 due to such cracking[51,52,53]. Even when a transition does not break the crystal, the spontaneous nature of the domain formation is irreproducible, greatly aggravating a systematic approach to studying the transition. This is because twinning boundary may be a source of non-uniform stress, and many properties in VO_2, most notably its transitions, are sensitive to such stress. The transformation that takes the crystal from R to M1 has four-fold degeneracy, which can be paired into two sets with distinct optical response[49] that can visually distinguished under a microscope with a linearly polarized light. (see figure 2-4) Some speculate on the possibility of a twinning boundary as the nucleation site for the high-symmetry metallic phase[54]. Not only that, these twinning structures can also develop as a result of external strain accommodation. In other words, it is no surprise that a systematic approach was very difficult because the VO_2 crystal is extremely sensitive to both internal and external strains, on which many of its properties depend. Such inhomogeneity of the strain field across the crystal, and therefore the non-uniform nature of the properties that arise, have hampered deducing the intrinsic properties and made a proper interpretation of experimental results difficult.

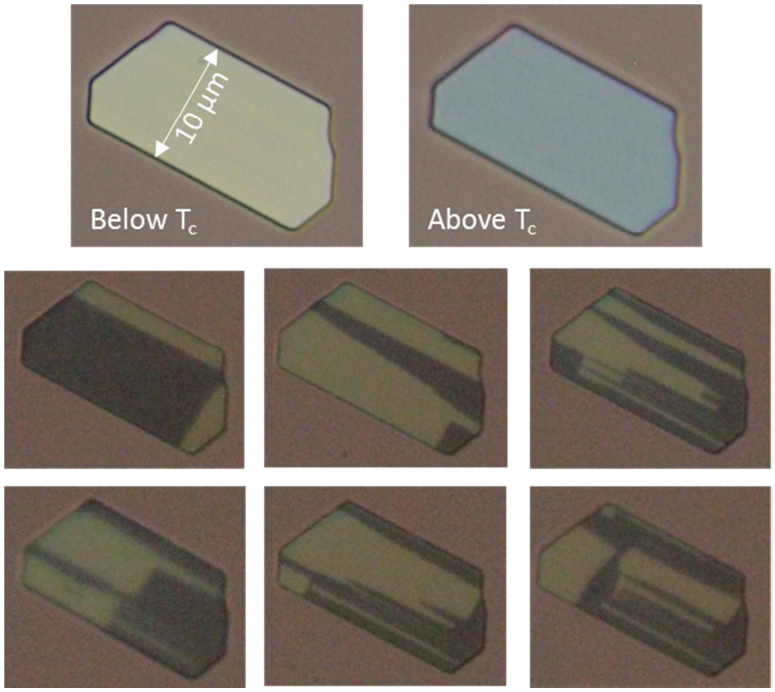

Figure 2-4 Microscope image of twinning in VO_2. Microscope images of a VO_2 crystal below and above the transition temperature. (top row) Microscope images of the same crystal under linearly polarized light reveal twinned structure when cooled below the T_c. (bottom two rows) Each time the crystal turns insulating, a distinct ferroelastic domain pattern is observed. This is not reproducible or controllable. Though there are four possible twinned structures, there are only two distinct optical responses. This crystal has been transferred from a SiO_2 to Al_2O_3 substrate, sitting loosely on the surface.

The problems of cracking and complicated domain structure in the bulk samples of VO_2 may be somewhat alleviated by working with smaller crystals. But unlike bulk samples, handling smaller crystals requires an appropriate substrate, usually one on which the synthesis takes place. Between the sample and the substrate, there can be mismatch of the lattice constants, differential thermal expansion, and random pinning potential as well as friction. Basically any of these adds a layer of complication onto the already spontaneous nature of the first-order phase

transition. A typical sample of the VO_2 crystals as grown on a SiO_2 substrate is shown in figure 2-5. VO_2 crystals grow firmly pinned to the oxide surface. Compared with figure 2-4, the pattern is more complicated with smaller domain sizes, in other words more twinning boundaries, probably because they provide external strain accommodation[54].

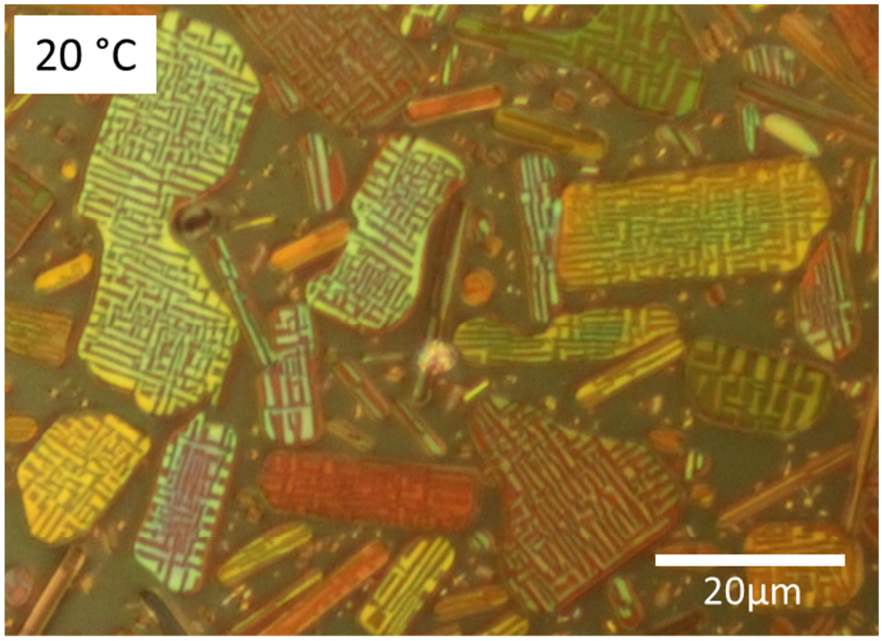

Figure 2-5 Microscope image of twinning in VO_2 crystals as grown on SiO_2/Si substrate. With the aid of a linearly polarized microscopy, two distinct types of ferroelastic domains can be distinguished. VO_2 crystals, as grown on the SiO_2 surface, are pinned to the substrate and show much more complicated twinning structure.

When heated above the transition temperature, the crystals that are pinned on a substrate do not turn completely metallic at an instant. Instead metallic domains form in various parts of the crystal, growing their size with an increasing temperature until they are completely metallic. (see figure 2-6) The competition of free energy with elastic energy, which originates from the boundary conditions imposed by the pinning substrate, leads to this

configuration of the alternating metallic and insulating domains[38,55]. The interpretation of any measurement performed on the film samples of VO_2, which also have this type of broadened phase transition, needs a careful attention since the measured quantity may have averaged over the properties of many domains of different phases. To reiterate, since the physical properties of this system are sensitive to stress, the non-uniform nature of the stress induced on the film sample makes the analysis that much more difficult, if not impossible. Without the intrinsic phase stability diagram of VO_2 with high accuracy and precision, any discussion of more complicated phase dynamics is only speculative and without a solid base.

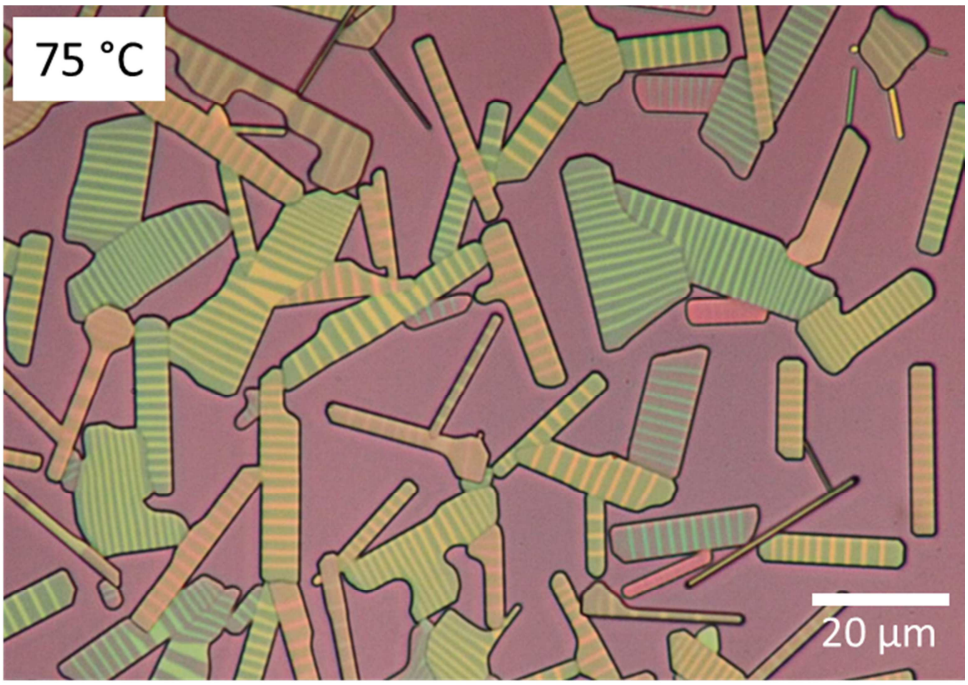

Figure 2-6 Alternation of metallic and insulating domains. At 75 °C, substrate-pinning combined with a mismatching thermal expansion produces coexistence of the insulating (yellow, brighter) and the metallic (green, darker) phases.

2.3 Advantages of suspended VO_2 nanobeams

As seen on figure 2-4, a large crystal may develop multiple twins but each domain has certain characteristic size. If a crystal has dimensions comparable or smaller than this size, it is unlikely that multiple domains develop and single nucleation suffices for the transition of the entire crystal. We observe that our VO_2 nanobeams with the typical dimensions of about <1 μm width, 50-500 nm height, and <100 μm are absent of the domain structure in the lateral dimensions. In other words, such nanobeam is single domain laterally and domain structure is only possible along the length of the nanobeam, hence it is effectively a quasi-1D system because we need not worry about the phase composition perpendicular to the vanadium chain axis. VO_2 nanobeams do not crack or degrade through thermal cycling[38,55,56], and are extremely robust against applied stress[37,57,58, 59] as expected of high-purity single crystal, not to mention the ease with which these high quality nanocrystals can be grown[10,60]. In order to realize even simpler system, it is desirable to avoid the domain structure along the nanobeam resulting from the substrate pinning such that it remains a single-domain crystal through the phase transitions. It has been shown that by removing the SiO_2 underneath the middle section of a nanobeam, using a buffered oxide etchant (BOE), a single-domain study of the suspended nanobeam under a uniform stress is possible and proved to be fruitful in discovering several new aspects[38] of the MIT. More importantly, VO_2 nanobeams are grown elongated along the vanadium chain axis, which is the ideal axis for strain application in order to tune the transition. (section 2.1) In summary, a systematic approach to studying the MIT is best exemplified in a suspended VO_2 nanobeam that allows superior control of the strain and other parameters.

2.4 Phase coexistence in VO_2 nanobeams

There are several features to note in coexistence of two phases in VO_2 nanobeam. First, the uniaxial stress and temperature of the nanobeam are not independent. (see Gibbs' phase rule) Another feature of coexistence is the divergent compressibility, where the uniaxial stress P of the nanobeam in coexistence is independent of changing L at a fixed temperature T. In coexistence, the fact that Gibbs free energies of the two phases are equal ($\Delta G = 0$) implies that it does not cost energy to switch from one phase to another, which is to say there is a degree of freedom in the proportion of the one phase to another. Therefore an external application of length change ΔL can be simply accommodated by the change in the proportion of the two phases with different lattice constants, without having to change its stress, or strain, along the beam. We will proceed with a concrete example in VO_2.

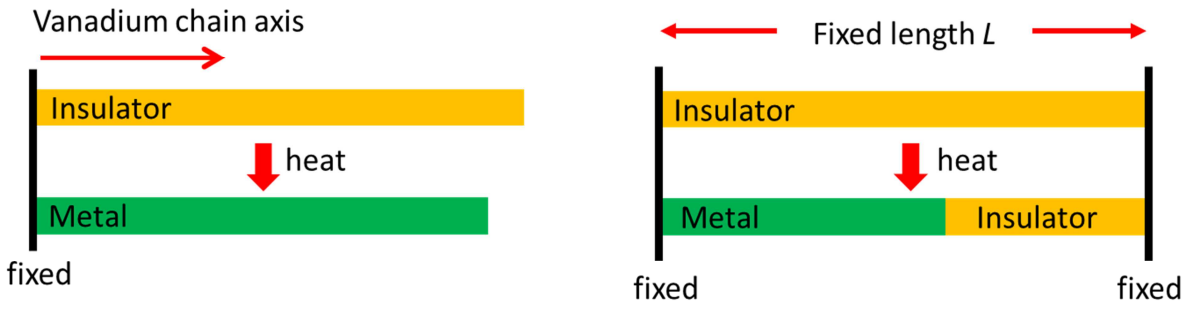

Figure 2-7 Metal-insulator transition in VO_2 at a fixed length. A suspended nanobeam fixed at both ends goes into coexistence at the MIT in order to minimize a combination of free and elastic energy costs. (see text) Controlling the length and temperature, the coexistence may involve any pair combination of M1, M2, or R phase.

When heated above the T_c, a cantilevered VO_2 nanobeam undergoes 1% contraction in length (R to M1) along the pseudo-rutile c axis as it turns fully metallic. In some long cantilever beams, the change in length at the transition can be visually observed under optical microscope. If the two ends of the nanobeam are fixed with the distance L in between, what we observe at the transition is quite different because of the imposed constraint. After heating above the transition temperature, a portion of the clamped nanobeam turns metallic, as opposed to the whole beam, dividing the nanobeam into two regions, one metallic and other insulating, with a sharp boundary. (see figure 2-7) Because the nanobeam must maintain its length through the transition, changing the whole beam metallic (1% contraction) would put the nanobeam under tension, incurring an elastic cost corresponding to one percent strain. The fact we always observe coexistence at the MIT on our devices suggests that such elastic cost that would be incurred by a fully metallic nanobeam is high compared to the energy cost of creating an interface. On the other hand, if the beam were to stay an insulator through this process, the situation is also unfavorable because metallic phase has lower free energy than insulating phases above the transition temperature. In other words, coexistence of two phases is the direct consequence of minimizing the combination of elastic and free energy, provided that the beam length is maintained at the transition. This is why we never observe a full transition from one phase to another in our devices with a fixed beam length. Conversely, a device without coexistence often suggests that the nanobeam is not anchored properly; it is a faulty device where the nanobeam is allowed to change its length freely as in cantilevered nanobeam.

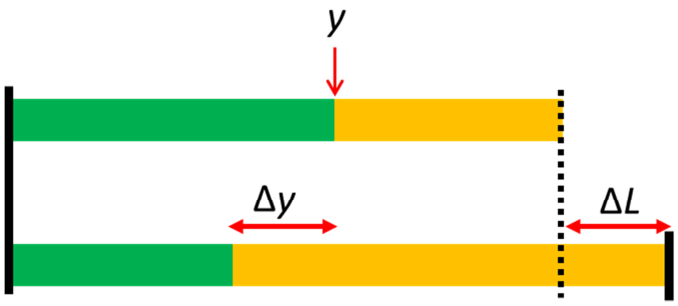

Figure 2-8 Response of a clamped VO_2 nanobeam to a length change in coexistence. Consider a coexistence of metallic (green) and insulating (yellow) phase. Because the insulating phase has a longer lattice constant along the length of the nanobeam, increasing the fraction of the insulating phase allows the nanobeam to elongate, while conserving the number of unit cells.

When changing L at a fixed temperature in coexistence, the strain of the nanobeam remains constant. Put another way, the change in L is accommodated by proportioning two phases with different lattice constants without having to stretch or contract. We will derive the mathematical relationship between the length L of a clamped nanobeam and the position y of the phase boundary wall. Because the nanobeam is clamped, the number of unit cells N is constant. Coexistence at length L_1 consists of a fraction x_1 of phase *i* and $(1 - x_1)$ of phase *j*. (*i,j* denote any two different phases in VO_2) Similarly coexistence at length L_2 consists of a fraction x_2 of phase *i* and $(1 - x_2)$ of phase *j*.

$$L_1 = Nc_i x_1 + Nc_j(1 - x_1)$$

$$L_2 = Nc_i x_2 + Nc_j(1 - x_2)$$

We consider an application of small length change δL such that $L_2 = L_1 + \delta L$,

$$\delta L = L_2 - L_1 = N(c_i - c_j)(x_2 - x_1)$$

The fraction x can be also written as the position y of the phase boundary wall divided by the length of the nanobeam, $x \equiv y/L$. (see figure 2-8) Rewriting the x's in terms of y and L, we also expect a small deviation $y_2 = y_1 + \delta y$,

$$x_2 - x_1 = \Delta x = \frac{y_2}{L_2} - \frac{y_1}{L_1}$$

Using $1/(1+\epsilon) \approx (1-\epsilon)$,

$$\frac{y_2}{L_2} = \frac{(y_1 + \delta y)}{(L_1 + \delta L)} = \frac{(y_1 + \delta y)}{L_1(1 + \delta L/L_1)} \approx \frac{(y_1 + \delta y)(1 - \delta L/L_1)}{L_1} \approx \frac{(y_1 + \delta y)}{L_1}$$

Plugging in $\Delta x = \delta y/L_1$ into the expression for δL gives,

$$\delta L = \frac{N}{L_1}(c_i - c_j)\delta y = \frac{c_i - c_j}{c_j}\delta y$$

where we have used $L_1/N \approx c_j$. We define a quantity $\alpha_{ij} \equiv c_i/c_j - 1$, which is the fractional change in the lattice constants of the different phases *i* and *j* with the phase *i* having the larger lattice constant. Finally a simple expression relating δL and δy is derived.

$$\delta L = \alpha_{ij}\, \delta y$$

Since α_{ij}'s can be calculated from the x-ray measurements (section 2.1), if we can measure the shift in the position of the phase boundary wall, we can calculate the change in the length of the nanobeam. Conversely, we can also deduce α_{ij}'s based on our measured changes in the length and the interface position. As we will see in chapter 4 and 5, this expression provides a basis for testing the accuracy of our measurement setup as well as the quality of the devices we fabricate.

2.5 Phase diagram

A phase diagram is a graphical representation that is used to show the distinct equilibrium phases of a matter at various conditions. In general the diagram is *n*-dimensional with *n* being the number of equilibrium conditions that characterize the system. The most common example is that of H_2O as a function of temperature and hydrostatic pressure. (see figure 2-9) Study of phase diagram is fundamental because it provides a natural nomenclature for classification of the properties that different phases manifest. Also it serves as a basis for further study of non-equilibrium dynamics, material engineering, and disentangling intrinsic properties from that of arising from complex domain structure. Furthermore, a phase diagram may contain the physical quantity of theoretical interest such as entropy of transition.

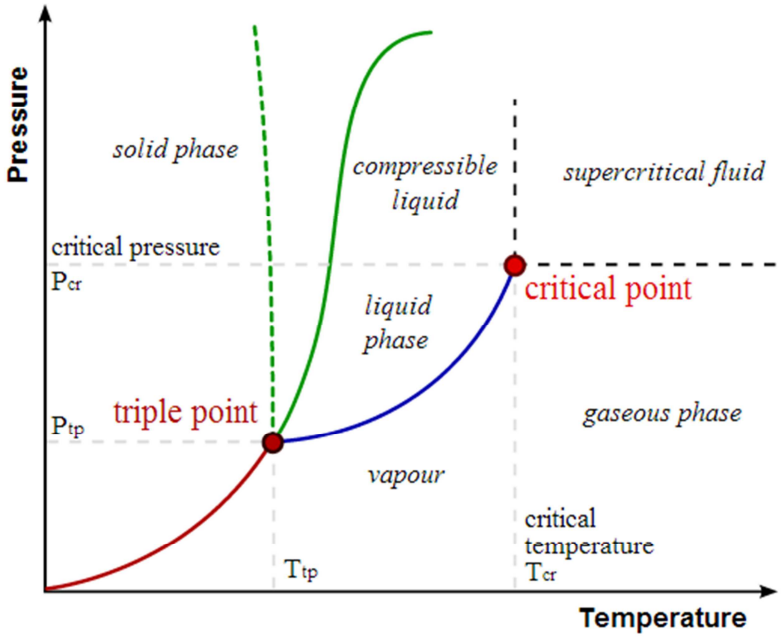

Figure 2-9 A phase diagram of water.

Figure 2-10 illustrates a coexistence line that separates two regions, phase 1 and phase 2. G denotes Gibbs free energy with the canonical variables of temperature T and pressure P. A coexistence line represents the equilibrium conditions (P, T) at which the Gibbs free energies of two distinct phases across the line are equal and hence their difference is zero. It also marks the locations of discontinuous phase transition.

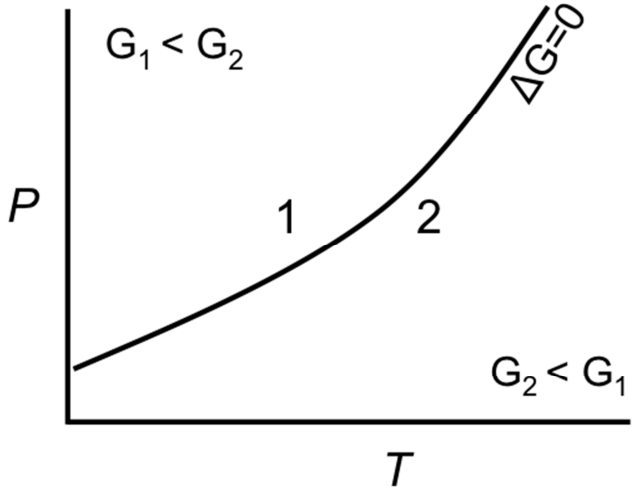

Figure 2-10 Schematic $P-T$ phase diagram. 1 and 2 denote different phases. The coexistence line separates the two phases and represents conditions (P, T) at which G_1= G_2 or $\Delta G = 0$, where G denotes Gibbs free energy.

From figure 2-10, the slope of the coexistence line can be written with the aid of the triple product rule,

$$\left(\frac{\partial P}{\partial T}\right)_{\Delta G} = -\left(\frac{\partial \Delta G}{\partial T}\right)_P \Big/ \left(\frac{\partial \Delta G}{\partial P}\right)_T$$

Since $dG = -SdT + VdP$, then it follows $d\Delta G = -\Delta S dT + \Delta V dP$. Evaluating the partial derivative on the right-hand side (RHS) yields,

$$\left(\frac{\partial P}{\partial T}\right)_{\Delta G} = \frac{\Delta S}{\Delta V}$$

Given that $\Delta G = 0$ along the phase boundary, we may write $\Delta G = \Delta H - T\Delta S = 0$.

$$\left(\frac{\partial P}{\partial T}\right)_{\Delta G} = \frac{\Delta H}{T\Delta V} = \frac{\Delta H/V}{T(\Delta V/V)}$$

The above equation is exact thermodynamically and can be further simplified by utilizing fractional volume change $\varepsilon = \Delta V/V$ or a combination of mass density ρ and molar mass m_a such that $\frac{\Delta H}{V} = \frac{\rho}{m_a}\left(\frac{\Delta H}{\text{mol}}\right)$. The molecular weight of VO_2 is 82.94 g/mol. The mass density is not constant since there is a volume change at the transition due to the structural phase transition and also thermal expansion. The volume in different phases can be calculated from a number of x-ray diffraction data on VO_2 crystals as discussed. We proceed with the mass density of 4700 Kg/m^3, using the x-ray diffraction data of the rutile structure nearest to the phase transition temperature as reported by Kucharcyzk[52].

In 1969, the work[61] by Berglund and Guggenheim included the unpublished work of Ryder et al that reported the value of 1020±5 Cal/mol (a mole of VO_2) for the latent heat. When unspecified, the transition is inferred to take place between R and M1 as the authors were unaware of the transition between R and M2 at the time. The value of 1020 Cal/mol equates to roughly the change of 1.51 k_B in entropy per vanadium atom. In the same year, Ladd and Paul reported $(dT/dP) = -1.2 \times 10^{-3}$ °K/bar, or $(dP/dT) = -83.3$ MPa/°C, by applying uniaxial stress *P* (here positive pressure implies compression) but the reliability of this value cannot be judged since there are few words on their experimentation or errors. More recently, these

values have been obtained by using bent[37,57] and suspended[38] nanobeams. Wei et al reported[38] $(dP/dT) \approx -18\ \mathrm{MPa/^{\circ}C}$, which is quite different from the literature value probably because the transition involved M2 and R instead of M1 and R. Calculating the exact value depends on the accuracies of several parameters such as Young's modulus[62,63,64,58,59,65], lattice constants, and thermal expansion coefficients[62,66,67,68,] as we will discuss in section 2.6. The accurate measurements of those parameters, as some authors pointed out, have been challenging because of the domain structure and the resulting inhomogeneity that are either intrinsic or caused by the active application of stress from the measurement.

2.6 Construction of the phase diagram in VO_2

A stability diagram in the $P_c - T$ plane (tensile pressure along the pseudo-rutile c-axis with all other stress components zero) is expected to have the layout indicated in figure 2-11. A shaded region indicates where the T phase occurs[36,69]. The effect of P_c on the phase stability resembles that of stress along the $[110]_R$ axis[36] and of doping[34] by Cr. Rough ideas of the locations of the three phase boundaries have been obtained by modeling bent nanobeams[37]. The triple point (T_{tr}, P_{tr}) has not been located, although M1 and M2 are known to be very close in free energy near the transition[36]. P_{tr} is normally taken to be positive (tension), implying that a perfect unstrained crystal exhibits a direct transition from M1 to R at T_c.

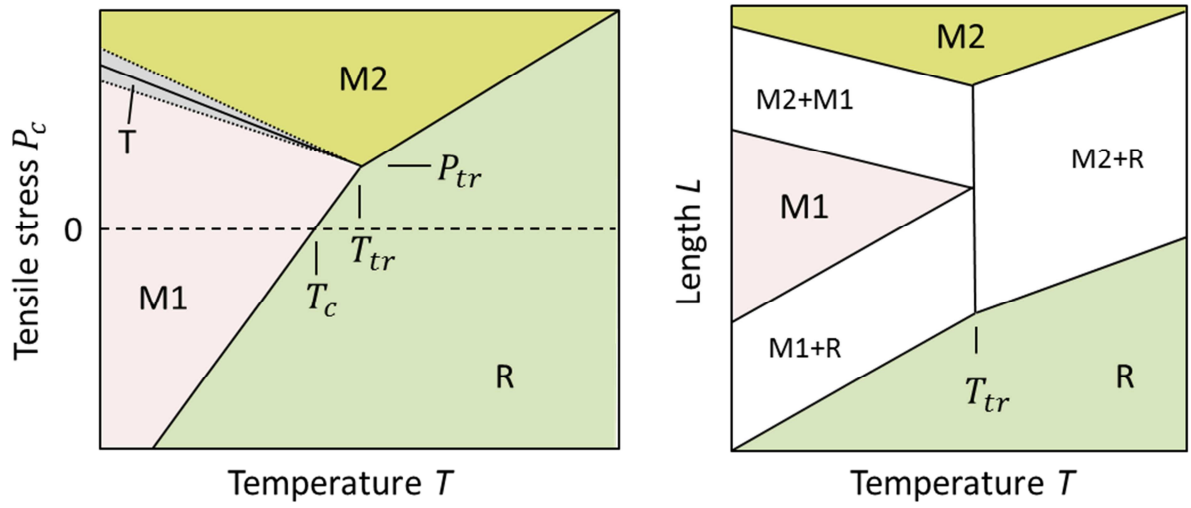

Figure 2-11 Expected layout of a phase diagram in VO_2. $P - T$ (left) and $L - T$ (right) diagrams are shown. Coexistence lines in a $P - T$ diagram have finite widths in the corresponding $L - T$ diagram. (see text) It is a useful construction since we control L, not P_c, experimentally. Also it helps us visualize our phase trajectory as we vary L and T.

The state of the nanobeam as a function of L and T, as opposed to P and T, should include regions of two-phase coexistence as sketched in figure 2-11. As mentioned in section 2.4, the stress of the beam is independent of the length change at coexistence. In other words, what used to be a point on the coexistence line of the $P-T$ diagram has a finite vertical width on the $L-T$ diagram, which represents varying proportion of the two coexisting phases in the nanobeam depending on its length. By controlling L and T, we find that indeed the suspended part of the nanobeam can be brought into coexistence between any pair of the three phases. (section 5.1) It should be noted that while the control of L and T should in theory allow us to explore any trajectory on the diagram, it is often complicated by nucleation and hysteresis.

Since the stress in coexistence must take the phase equilibrium value, consideration of a variation of the strain η with T yields[38],

$$\frac{1}{E}\frac{\partial P_c}{\partial T}\bigg|_{ij} = \frac{d\eta}{dT}\bigg|_{ij} = -\frac{\alpha_{ij}}{L_0}\frac{dy_{ij}}{dT} - \Delta K$$

Here it is assumed that the Young's modulus E is the same in each phase. (there is more discussion on this assumption in section 5.3) The axial strain has a uniform value $\eta = P_c/E$ throughout the beam. The first term on the right is the change in strain due to movement of the interface y_{ij} and L_0 being the effective clamped length. (see section 2.4 for the definition of α_{ij}) The second, ΔK, is the thermal expansion mismatch between nanobeam and silicon substrate that produces some correction. (section 5.3)

The slopes of the boundaries should be consistent with the constraint of the Clausius-Clapeyron relations given in section 2.5, where we have modified the form appropriately for a

nanobeam under uniaxial stress along the beam. A positive stress as used in the Clausius-Clapeyron relation is compression while a positive stress as applied to the nanobeam is defined to be tensile for consistency with a positive strain being elongation. This explains the negative sign in the below expression for the phase boundary slope,

$$\left.\frac{\partial P_c}{\partial T}\right|_{ij} = -\frac{\Delta S}{\Delta V} = -\frac{S_i - S_j}{b^2\left(a_i - a_j\right)} \approx \frac{S_j - S_i}{\alpha_{ij} V_c}$$

where S_i is the entropy per vanadium pair in phase i, a_i is the height of the pseudo-rutile unit cell in phase *i*, *b* is the base length of the rutile unit cell, and V_c is the rutile unit cell volume. We can evaluate the above expression at the triple point,

$$\left.\frac{\partial P}{\partial T}\right|_{M2M1} = \frac{S_{M1} - S_{M2}}{b^2\left(a_i - a_j\right)} = \frac{(S_R - S_{M2}) - (S_R - S_{M1})}{b^2\left(a_i - a_j\right)}$$

$$= \frac{b^2(a_{M2} - a_R)\left.\frac{\partial P}{\partial T}\right|_{M2R} - b^2(a_{M1} - a_R)\left.\frac{\partial P}{\partial T}\right|_{M1R}}{b^2(a_{M2} - a_{M1})}$$

Rearranging,

$$(a_{M2} - a_{M1})\left.\frac{\partial P}{\partial T}\right|_{M2M1} = (a_{M2} - a_R)\left.\frac{\partial P}{\partial T}\right|_{M2R} - (a_{M1} - a_R)\left.\frac{\partial P}{\partial T}\right|_{M1R}$$

$$\frac{(a_{M2} - a_{M1})}{a_R}\left.\frac{\partial P}{\partial T}\right|_{M2M1} = \frac{(a_{M2} - a_R)}{a_R}\left.\frac{\partial P}{\partial T}\right|_{M2R} - \frac{(a_{M1} - a_R)}{a_R}\left.\frac{\partial P}{\partial T}\right|_{M1R}$$

$$(\alpha_{M2R} - \alpha_{M1R})\left.\frac{\partial P}{\partial T}\right|_{M2M1} = \alpha_{M2R}\left.\frac{\partial P}{\partial T}\right|_{M2R} - \alpha_{M1R}\left.\frac{\partial P}{\partial T}\right|_{M1R}$$

Plugging in the expression for $\frac{1}{E}\left.\frac{\partial P_c}{\partial T}\right|_{ij}$ from above,

$$(\alpha_{M2R}-\alpha_{M1R})E\left(-\frac{\alpha_{M2M1}}{L_0}\frac{dy_{M2M1}}{dT}-\Delta K\right)$$

$$=\alpha_{M2R}E\left(-\frac{\alpha_{M2R}}{L_0}\frac{dy_{M2R}}{dT}-\Delta K\right)-\alpha_{M1R}E\left(-\frac{\alpha_{M1R}}{L_0}\frac{dy_{M1R}}{dT}-\Delta K\right)$$

Assuming ΔK and E are equivalent in all three phases, they cancel out on both sides.

$$-(\alpha_{M2R}-\alpha_{M1R})\,\alpha_{M2M1}\frac{dy_{M2M1}}{dT}=-\alpha_{\mathrm{M2R}}^2\frac{dy_{\mathrm{M2R}}}{dT}+\alpha_{\mathrm{M1R}}^2\frac{dy_{\mathrm{M1R}}}{dT}$$

Since $\alpha_{M2R}-\alpha_{M1R}=\alpha_{M2M1}+\alpha_{M2M1}\alpha_{M1R}\approx\alpha_{M2M1}$, the Clasius-Clapeyron relation simplifies to

$$\alpha_{\mathrm{M2M1}}^2\frac{dy_{M2M1}}{dT}+\alpha_{\mathrm{M1R}}^2\frac{dy_{\mathrm{M1R}}}{dT}=\alpha_{\mathrm{M2R}}^2\frac{dy_{\mathrm{M2R}}}{dT}$$

The equation can also be written in terms of the phase boundary slopes in strain versus temperature diagram.

$$\alpha_{\mathrm{M2M1}}\frac{\partial\eta}{\partial T}\bigg|_{M2M1}+\alpha_{M1R}\frac{\partial\eta}{\partial T}\bigg|_{M1R}=\alpha_{M2R}\frac{\partial\eta}{\partial T}\bigg|_{M2R}$$

In conclusion, simple measurements of y versus T in coexistence allow us to calculate the phase boundary slopes with a few other parameters. Although the above equation constrains the slopes of the phase boundaries at the triple point, they are not sufficient to construct a phase diagram.

3 Vanadium Dioxide Nanobeams

The study of any oxides is complicated by its stoichiometry[70]. Kosuge in 1966 reported the phase diagram from V_2O_3 to V_2O_5 including a family of vanadium oxides known as the Magnéli phases[71]. While it is difficult to precisely measure oxygen concentration, and therefore determine the stoichiometry, distinct characteristics of the metal-insulator transition in VO_2, such as the transition temperature and sharpness of the transition, are often used as a guide for guessing the purity of a VO_2 sample. VO_2 crystals can be prepared by a number of growth methods such as physical vapor transport[10,66], decomposition[60,72] of V_2O_5, chemical vapor deposition[73], sol-gel[74,75], pulsed laser deposition[76], hydrothermal[32,77], and sputtering[78]. The epitaxial growth[24,79,80] of VO_2 on a TiO_2 (rutile) substrate offers preferential growth direction and strain engineering by mismatch of the lattice constants, allowing some tuning of the phase transition temperature. As discussed in section 2.3, the success of our proposed work hinges critically on working with single nanocrystals of VO_2, as opposed to bulk or film samples. Our desired nanobeam is just wide enough to be visually inspected for its domain composition and long enough to be made into a suspended device while remaining free of ferroelastic domains. Since the morphology of the crystals is determined by the growth conditions and the type of substrate used in the process, various parameters that were explored in this project are presented in this chapter to the extent of our experimental utility. It should be emphasized that the goal of our crystal synthesis was to provide useful crystals for our experiments quickly and reproducibly, purposely avoiding the rigor and wholeness on the topic. Hence a number of observations are presented in the chapter without their possible origins and implications. Much

of what we observed, however, can be interpreted in light of the recent work[60] by Strelcov et al, who constructed an image oven, capable of in situ visual inspection of the growth process.

3.1 Growth procedure

VO_2 nanobeams, typically 50-100 μm long, less than 0.5 μm thick, and about 1 μm wide, were grown by physical vapor transport on SiO_2 from a V_2O_5 (Alfa Aesar) source. The growth setup is depicted in figure 3-1. Inside a tube furnace (Lindberg Blue M), a substrate, usually a 1 cm^2 cleaved chip of 500 μm thick silicon wafer with oxide, was placed 3-7 cm downstream from an alumina crucible (AdValue AL-5003) containing 40-60 mg of the source, all inside a quartz tube with a glass-to-metal seal at the ends. Vacuum flanges with metal gaskets were used for baking the system if needed. Copper tubing was used for gas handling with Swagelok valves and fittings. A helium leak detector was used to check any leak on tube interconnects as well as valves. Using an oil pump, the tube was evacuated and heated to 950 °C. The pressure inside the tube was kept in a few mbar argon carrier gas during the growth that takes less than half an hour. Our controlled parameters to the growth were the oven temperature, the amount of the V_2O_5 source, the position of the alumina crucible, the position of the substrate, the material and surface preparation of the substrate, the gas flow rate, the pressure inside the tube furnace, and the gas flow start/end time. Sometimes the oven lid was opened intentionally to increase the cooling rate. The parameters of each growth was carefully controlled and recorded in a Microsoft Access database created by Serkan Kasirga. The resulting growth was observed under a Zeiss optical microscope equipped with 100x objective and a 15 megapixel digital camera.

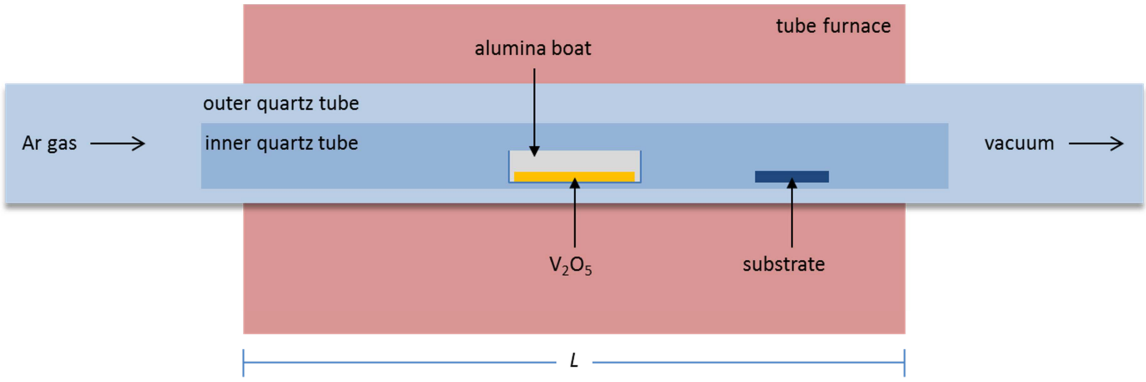

Figure 3-1 Growth setup. The schematic shows the essential ingredients of the physical vapor transport method. The argon gas cylinder and oil pump are not shown in the picture. Swagelok fittings are used for gas handling. The quartz tube gets dirty and becomes opaque after a few growths. Therefore an inner tube is used to prevent deposition on the outer tube, which should remain transparent, and the inner tube can be easily replaced once it gets dirty. (Quartz tubes from Technical Glass Products Inc.) *L*=38 cm

3.2 Growth optimization

The task of exhausting all parameter space in order to optimize the growth conditions is not a feasible option. So some preliminary experiments were performed in order to identify the controllable parameters with greatest impacts on VO_2 growth. Several difficulties, however, made it nearly impossible to draw proper conclusions at first. The results of the growths that were conducted under identical conditions were often uncorrelated. To make the matter worse, there was a wild variation of crystal morphology present even on a single chip. (see figure 3-2) As it turns out, the main causes of the irreproducibility of VO_2 synthesis were VO_2 source and preparation methods used for cleaning the substrate prior to the growth. The optimization of growth parameters, such as temperature, gas flow, placement of source and substrate, and so on, followed after establishing high level of reproducibility.

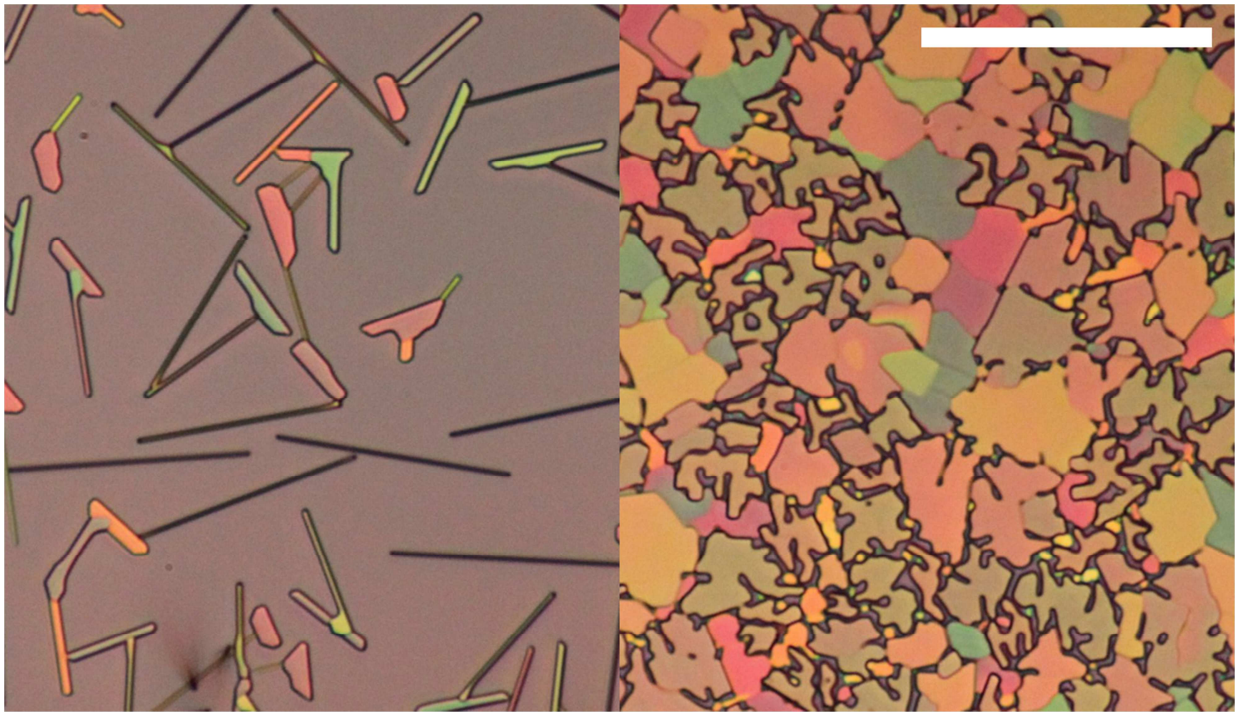

Figure 3-2 Variation of crystal morphology on a single chip. These micrographs are taken from a single chip. (1 cm^2 in size, growth #51) Even on a same chip, regions with distinct crystal morphology exist, making it difficult to analyze the effects of the growth parameters. Scale bar 30 μm.

Prior to using the V_2O_5 decomposition method, we had used pure VO_2 powder as our source material. But the growth time was on the order of hours probably because of low vapor generation from the source. The melting point of VO_2 is 1967 °C, well above the maximum temperature of the tube furnace around 1100 °C. After some experiments with V_2O_5 source, it became apparent that above 750 °C (as read by the tube furnace) and at some range of pressures around a few mbar, only VO_2 will crystallize on oxide (SiO_2) surface. The exact ratio of vanadium to oxygen is not as a critical factor as previously thought, as evidenced by the fact we are using V_2O_5 source. There are a number of advantages to be gained from using V_2O_5 instead of VO_2 because V_2O_5 has lower melting point and V_2O_5 is stable at room temperature, less likely

to oxidize and change its properties from hydration. High vapor generation from the low melting point allows quicker growth of the VO_2 crystals in matter of minutes and the growth could be performed at a temperature several hundred degrees lower. Overall, changing the source had its greatest impact on the efficiency of our experimentation, allowing tens of growth attempts per day to explore much larger parameter space.

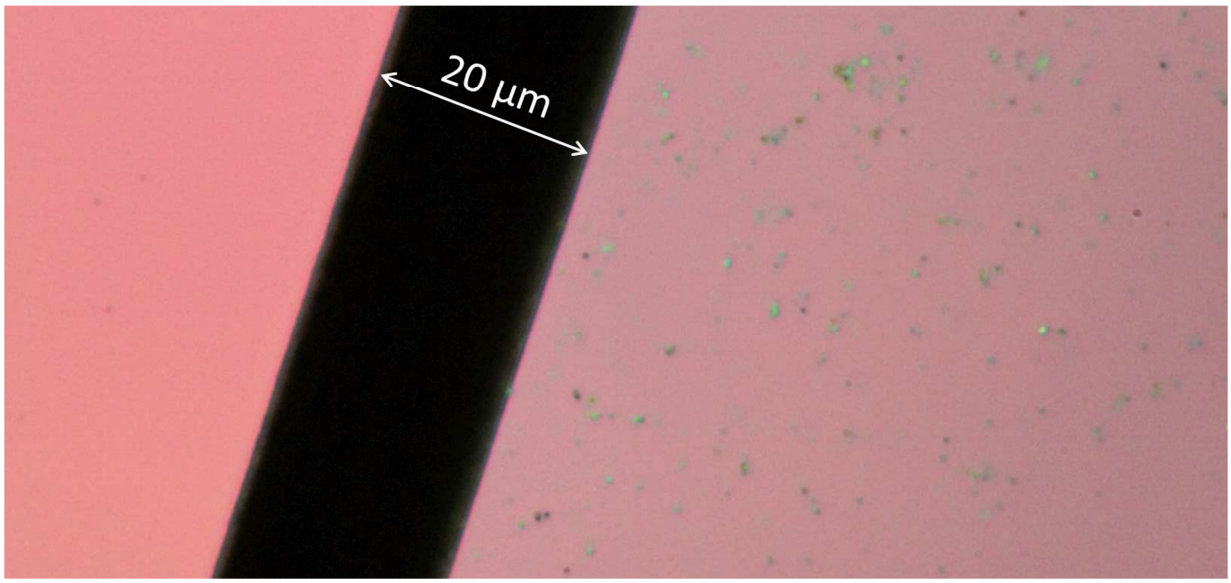

Figure 3-3 Comparison between cleaned and as-is silicon chip surface. A Si chip was intentionally left uncovered under a fume hood for several days and subsequently cleaned with BOE on the left side and left as-is on the right.

The preparation of the substrate surface is a very important key in ensuring the reproducibility of VO_2 synthesis. Though the wafers were kept in an air-tight chamber, handling wafers in a lab environment (non-cleanroom) tends to accumulate some residues on the surface. To test the effects of these residues and explore how to clean them, a Si wafer (4-inch [100] 500 µm thick with 500 nm oxide) was cleaved into a multiple 1 cm^2 chips, which were left uncovered in the lab for various amounts of times, from several days to a week. Over time, the

surface of each silicon chip accumulated deposits that could be seen under a microscope. By observing the microscope images before and after the growth, we observed a correlation between the areas of surface contamination and the concentrated regions of VO_2 crystals, suggesting either enhanced nucleation of VO_2 crystals or catalyzed growth at those spots. Rinsing or sonicating the wafer with acetone and/or IPA did not have a noticeable effect of removing the residues. In some cases, piranha etch was performed with no avail. So buffered oxide etchant (BOE) was used to slightly etch the oxide underneath, removing these residues effectively. For a note, it can be a cumbersome task to prepare each growth substrate using BOE because of the cautionary steps that are necessary for handling such dangerous chemical but its benefits far outweigh the unpredictability of the surface condition. Another important issue with silicon wafers is the silica surface that can be hydrated or modified with a alcohol presence[81] that alters the hydrophobicity, or hydrophilicity. We prepared the growth substrates by cleaning with BOE, which made the surface completely hydrophilic, rinsing with water, and blowing dry with a nitrogen gun. In this way, every chip surface could be prepared in an identical condition without any surface contamination. Indeed, after such procedural change, we started to observe uniform distribution of nanocrystals (see figure 3-4) except at spots where tweezers were used to grab the chip.

There are other nuances of the growth system that may affect the reproducibility. One example is the deposition of vanadium oxide on the inner quartz tube. Each growth coats the inner wall of the quartz tube with some vanadium oxide, which decreases the visibility for positioning the source boat and the growth substrate. (the visibility is completely lost after about five growths) Outer quartz tube has metal-to-glass seals on both ends that make the

replacement of the quartz tube more difficult and costly. Hence, inner quartz tube is a useful component as it protects the outer tube from the material deposition and can be easily replaced. But with each growth, the increased amount of deposited material on the inner wall of the tube could actually act as another source of vanadium oxide alongside the source boat.

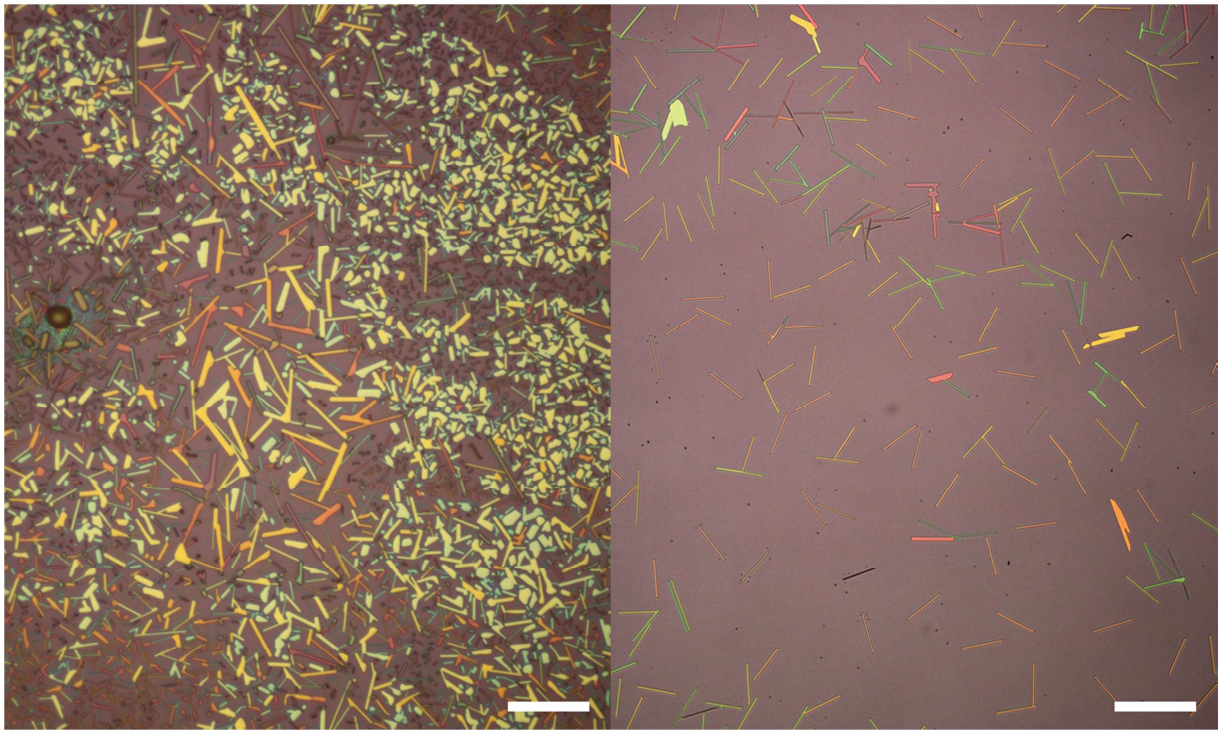

Figure 3-4 Growth comparison between Si chips with different cleaning procedures. A typical growth without using BOE to clean the surface (left) and after using BOE (right). Scale bar 100 µm.

The oven's temperature reading was measured by the type-k thermocouple embedded in the center of insulation material right under where a quartz tube sits. The readout more or less corresponds to the temperature of the source boat. The variation of the temperature inside the tube furnace, however, was unknown. An electric feed-through was used to insert a type-k thermocouple to measure the temperature variation inside the tube. The insulation

around the quartz tube spans about 15 cm both ways from the center. The rapid drop-off in the temperature at this position is evident. (see figure 3-5) The temperature of the growth substrate was approximated from the plot.

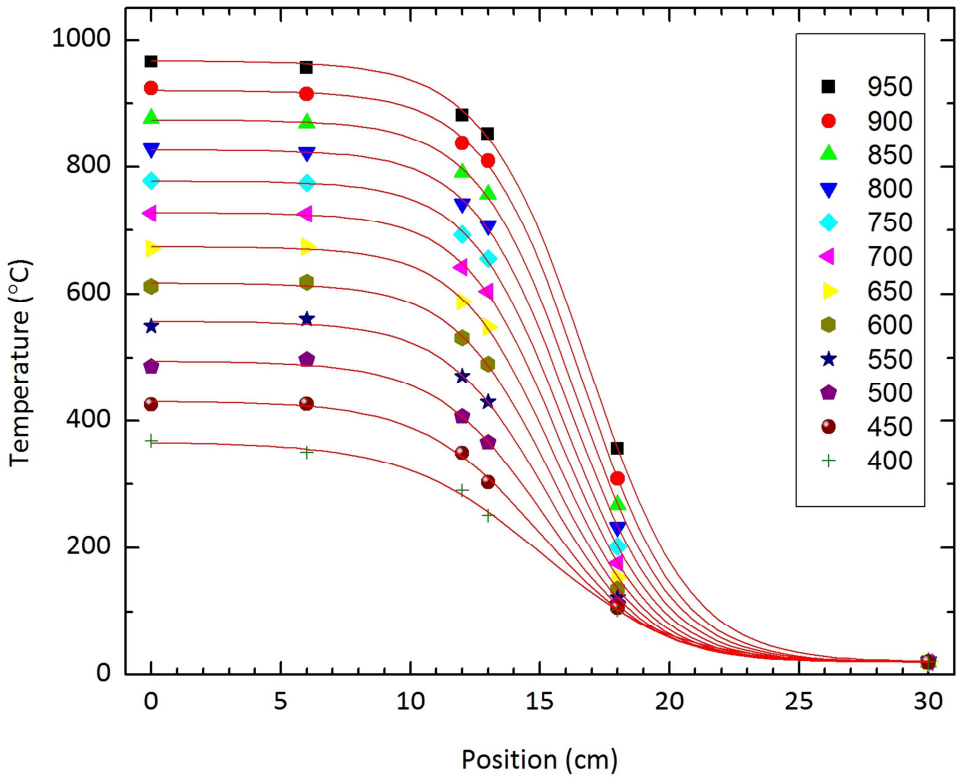

Figure 3-5 Furnace temperature profile. While fixing the tube furnace temperature (see legend), the temperature inside was measured by a type-k thermocouple in vacuum as a function of the position from the center (zero) of the furnace. (No gas flow)

Some general statements about the growth can be made: There is no growth without any source but too much of it cause an overgrowth. The absence of the Ar carrier gas flow leads to no growth of VO_2 crystals. The duration of this flow is a crucial factor for the sizes of the crystals and so on. But these statements are of little practical value since the relationship

between the growth parameters and their effects are much more complicated. This is because changing one parameter inevitably changes another parameter that may also affect the growth condition. In other words, very little can be said with certainty about the effects of changing one parameter without specifying all other parameters. But doing so is a daunting task. So growth parameters of various extremes were chosen first to home in on the likely window of optimal values. Hundreds of growths were performed by varying one growth parameter while all other controllable parameters were fixed. A window of the optimal parameter values can be guessed because the growth should behave distinctly on either side of the window. By repeating this process and ensuring the reproducibility of each result, a set of working ranges for each parameter was determined and used subsequently for fine-tuning the growth further.

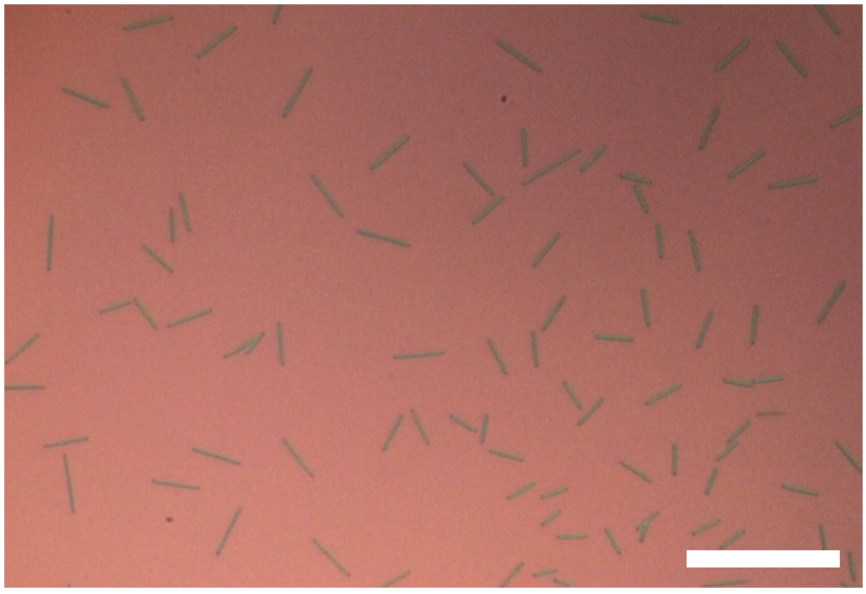

Figure 3-6 An example of premature growth. The crystals are too narrow and thin to work with. (Growth #59, scale bar 40 μm bar)

Starting with the growth parameters that yield no visible crystal, the parameters were slowly adjusted until some crystals were obtained. Figure 3-6 shows a typical result of the

growth with some crystals but is premature. Comparable sizes of all the crystals on the chip are a positive sign that these crystals were nucleated and grown uniformly. But their small sizes suggest more source, longer time of growth and gas flow may be needed.

On the other hand, the growth parameters were eventually tuned to yield overgrowth as seen on figure 3-7. In this case, the crystals of VO_2 covered the entire substrate surface and start to grow wires in the out-of-substrate direction.

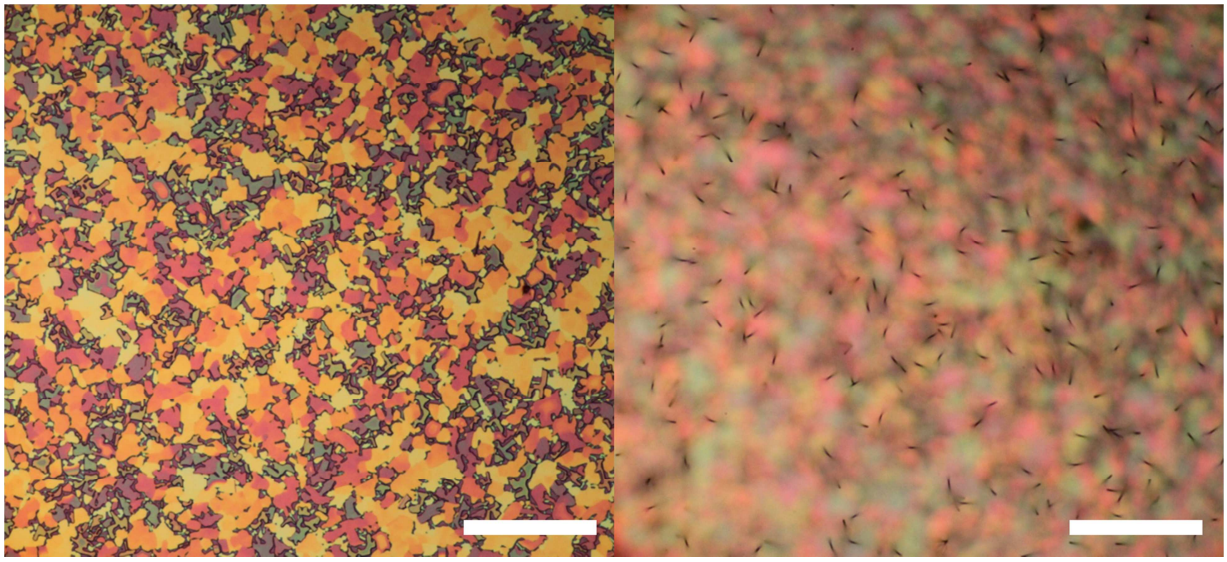

Figure 3-7 An example of overgrowth. VO_2 crystals cover the entire surface. They are reminiscent of a bulk film sample with grain boundaries. (left) The same sample at a different focal plane shows the VO_2 wires that are sticking out of the substrate. (right) (Growth #62, Scale bar 40 µm)

An optimal condition can be obtained by going back and forth between these two types of growth. The nanobeams as shown on figure 3-8 are long enough to be suspended across 40 µm slits and wide (approximately 1 µm) enough for clear phase identification. They have an appropriate size for poking with a probe needle for position and angle adjustments. The optical

contrast between M1 and M2 is visible unlike the very narrow nanobeams in figure 3-6. The growth conditions used in this chip are 22 mg of V_2O_5 source inside a boat placed at the center of the oven and a BOE-cleaned SiO_2/Si chip placed 7 cm away from the boat. The oven ramped to 1000 °C in 18 minutes, kept at 1000 °C for 12 minutes, and let cooled. Argon gas was on at 950 °C on the way up and off at 800 °C on the way down.

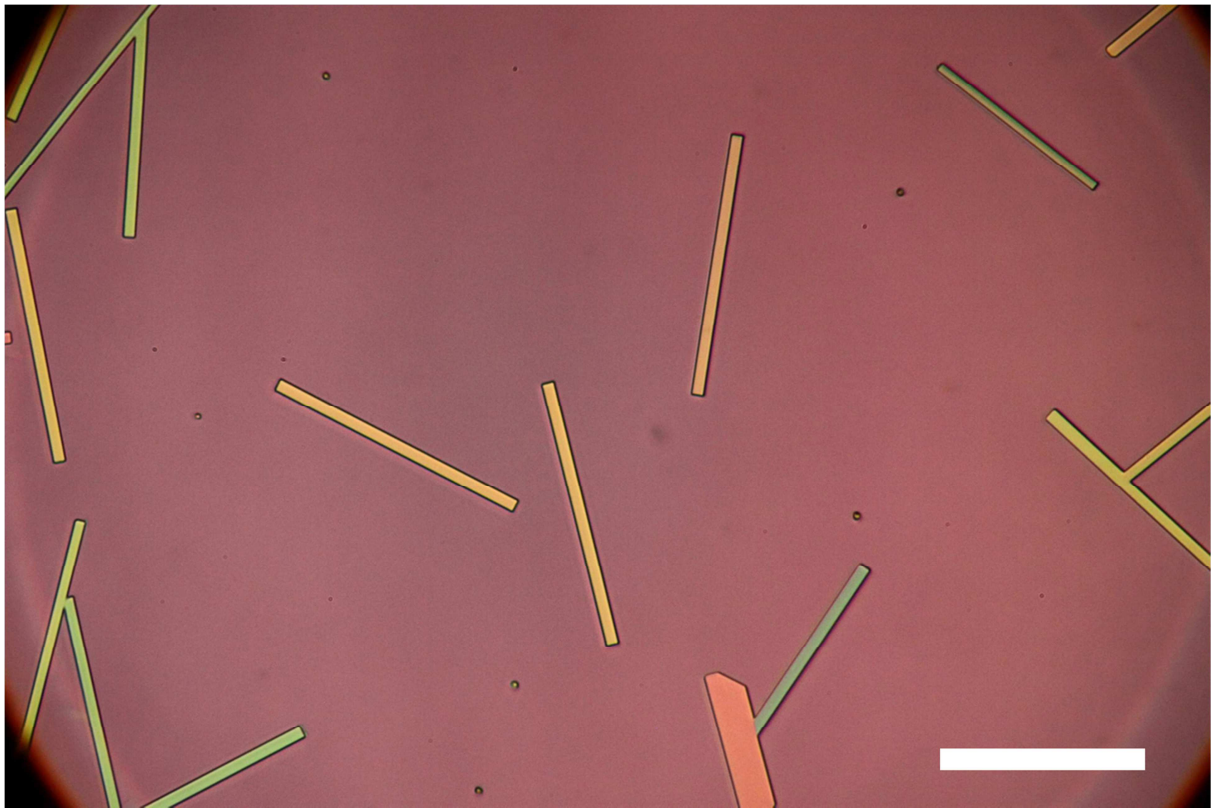

Figure 3-8 An example of optimal growth. (Growth #177, scale bar 40 μm)

3.3 Crystal modification

By precisely controlling the shape and size of VO_2 crystals, not only it is possible to study their properties in various experimental platforms that may require different crystal

morphology but it would be also interesting to simply study the effects of morphology on the phase transition. To this end, annealing (heating in vacuum) and regrowth (growth with pre-existing crystals) were performed on some samples. There are several interesting questions like: i) is it possible to start with a seed nanobeam and indefinitely grow it to a single bulk crystal? ii) starting with a bulk crystal, can it be reduced down to a single nanobeam? Figure 3-9 shows a series of pictures, demonstrating the effects of either annealing or regrowth on a VO_2 crystal. In summary, heating a crystal in the absence of V_2O_5 source leads to the reconfiguration of the crystal shape into more rounded feature probably because it reduces the surface energy. It was inconclusive as to whether the crystal size actually reduced. On the other hand, crystals became enlarged and faceted after the regrowth, showing it may provide a viable route to enlargement on a pre-existing VO_2 crystal.

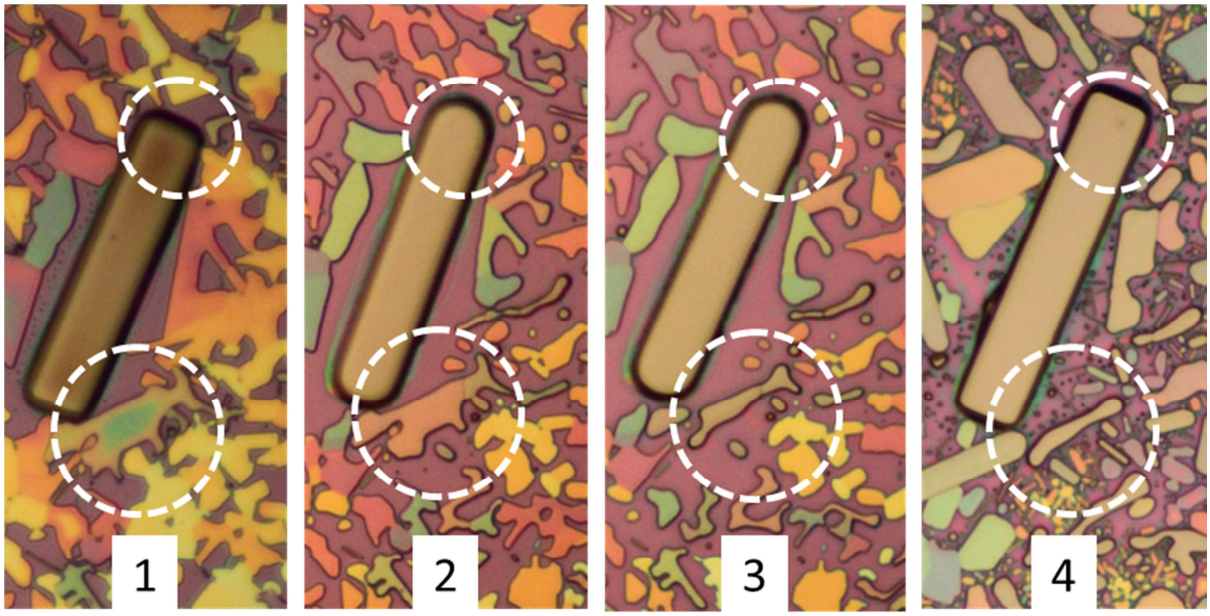

Figure 3-9 Annealing and regrowth. 1) As grown sample 2) After annealing at 950 °C for 10 minutes 3) After annealing at 950 °C for 25 minutes 4) After regrowth

4 Experimental Methods

The central issue of the thesis is the phase diagram of VO_2 system near the triple point, where the relationship between the metallic (R) phase and the two insulating (M1 and M2) phases, and their first-order solid-state phase transitions, remains intriguing. In section 2.3, we discussed the advantages of working with a single VO_2 nanobeam. Also due to the different lattice constants of the three phases along the pseudo-rutile c axis, controlling this length of a VO_2 nanobeam allows us to study the transitions between them methodically as a function of temperature and strain. Working with nanocrystals, however, presents a set of experimental challenges because of their small size. i) The Euler buckling pressure, the maximum compression before buckling, is low due to the small cross-section and long length of a nanobeam. In other words, it constrains the construction of the phase diagram in the compressive regime. ii) The manipulation of a single nanocrystal, in order to position on a suitable substrate for a given experiment, is not simple. iii) The method and nature of clamping down the both ends of a nanobeam to a substrate is not at all straightforward. The effects the clamping has on the nanobeam properties are unknown. iv) There are a number of possibilities for controlling the length of a single nanocrystal but not many with both high accuracy and precision. v) The direct measurement of applied strain in a nanobeam is difficult, especially on a table-top experiment. (ie, not using a TEM) To address these issues, we have developed a detailed approach to applying controlled strain to a suspended nanostructure while carrying out optical and transport measurements. In this chapter, our methods from building the unique apparatus to the experimentation and their technical aspects are discussed.

4.1 Overview

It is not difficult to see why one would start with a silicon (Si) wafer. The abundance of Si in the earth's crust makes it cheap and fabrication processes, which are extensively documented and have a huge library, are readily accessible in a number of fabrication facilities. It is arguably the most studied and well-characterized element, which makes it easy to account for in experiments. A Si wafer provides a rigid substrate but can be made flexible after micromachining process, e.g. thinning by dry etch. The surface of Si wafer can be polished down to a nanometer roughness, and oxide is readily available, which provides a smooth, insulating surface. Si wafer is a convenient substrate to position a VO_2 nanobeam and perform lithography as well as metallization, not to mention bonding well with epoxy for adhesion applications. Si also has a coefficient of linear thermal expansion comparable to that of invar, which is uniquely known for its low thermal expansion. This is helpful for minimizing position drifts while performing thermal measurements. Si, unlike plastic substrates, has a high melting point that makes it compatible with high-temperature processes such as crystal synthesis, annealing, drawing molten indium, metal deposition, and epoxy curing. All of these points strongly suggest using Si wafer as a device substrate.

There are a number of ways in which the length of a suspended nanobeam can be controlled[59,82,83,84]. In order to arrive at our eventual approach, the two most common methods, three point bending and comb drives, were considered first. (see appendix for more details) In short, they did not meet at least one of the requirements necessary for the experiment, which include active application of length change (both positive and negative), accurate and precise

measurement of the length change, feasibility of device fabrication, and compactness to fit under a microscope. The current approach to controlling the strain has been developed after considering all of the above criteria. In this approach, the key purpose of a fabricated Si chip is to serve as an intermediary between a nanobeam and the strain apparatus. The Si chip simply provides a substrate, a slit on which nanobeams are suspended, and converts the mechanical actuation by a piezo-controlled pusher into a length change of a nanobeam. (see figure 4-1) It also provides electrical contacts as well as means to measure the applied length change. A Si chip with at least one suspended nanobeam, clamped on both ends, is considered a device. Below is a quick summary of the device fabrication process.

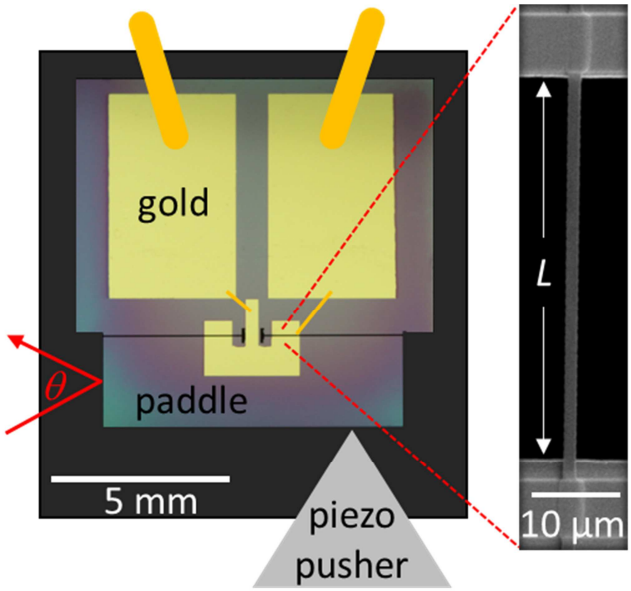

Figure 4-1 Si device picture. Experimental geometry, showing an electron micrograph (right) of a VO_2 nanobeam suspended across a slit of width L in a silicon chip (left, optical micrograph) whose width is controlled by pushing on the paddle with a piezo pusher. Depending on the placement of the piezo pusher on either left or right side, negative or positive length change is applied. The change in the position of the deflected laser beam off the sidewall of the Si chip varies linearly with L. The yellow lines represent gold wire bonds.

The bare minimum requirement for controlling the length of a suspended nanobeam is a slit of adjustable width across which two ends of the nanobeam are fixed. Optical lithography and deep reactive-ion etching were used to micromachine slits in a 1 cm^2 silicon chip with 2 μm wet oxide to form the paddle. (section 4.2) VO_2 nanobeams, typically 50-100 μm long and <0.5 μm thick, grown by physical vapor transport on SiO_2 from a V_2O_5 source and loosened with buffered oxide etch, were placed across the slit using a micromanipulator. (section 4.3) UV-curable epoxy was then applied to the both ends of the nanobeam and cured. The epoxy wets the interface between nanobeam and chip, effectively clamping the nanobeam close to the edges of the slit. (section 4.4) In some cases the nanobeam was contacted electrically either by electron-beam induced Pt deposition or by drawing molten indium wires, gold-wire-bonded to Au/Ti contacts which were patterned using shadow-mask evaporation. In one case electron-beam induced Pt deposition was used both to clamp the nanobeam and to make contacts, but the Pt pads quickly fractured. (section 4.5)

The Si chip is then mounted on the strain apparatus, a term to designate all equipment besides the device, where both clamped length L and temperature T of the single VO_2 nanobeam can be actively controlled by piezo actuator (section 4.6) and heating stage (section 4.7). By varying L and T, the three phases R, M1 and M2 can be induced and can be differentiated by reflection contrast microscopy as well as by Raman spectroscopy and electrical resistance measurements. The device is then tested for coexistence and reproducibility. Linearly polarized light also reveals twinning, allowing us to select devices where twinning is absent. The layout of the measurement system is depicted in figure 4-2.

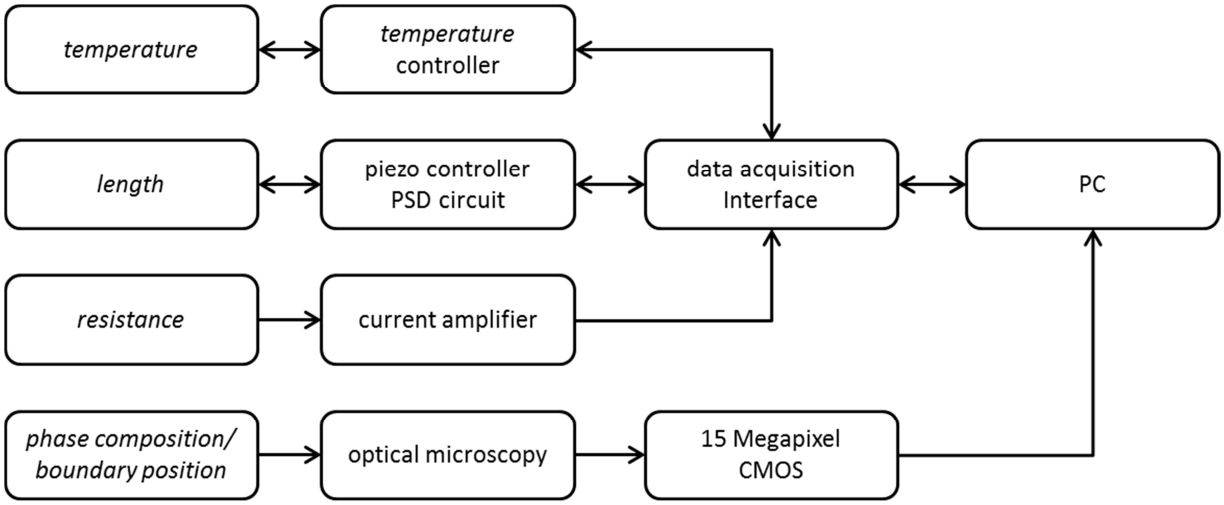

Figure 4-2 Schematic diagram of the strain apparatus. The diagram shows the measurement process of the relevant physical variables in the experiment and how various components are connected. Double-arrow indicates feedback.

4.2 Silicon chip fabrication

Here is how we chose the appropriate dimensions for the Si device chip. Smaller Si chip means more chips per wafer, saving time and money by decreasing the number of necessary fabrication runs. But more importantly, it is crucial that the chip was large enough to interface with piezo pusher, laser beam, heating stage, and electrical probes simultaneously. The chip area of 1 cm^2 is a reasonable comprise between the two factors, making it easy to handle and locate. The size is also compatible with the tube furnace that allows direct growth of VO_2 on the chip as well as annealing procedure if necessary. Next, finite element analysis (FEA) tool (AutoCAD Multiphysics) was used to simulate the response of the Si chip under load. More specifically the motion of the paddle is simulated as a function of various hinge dimensions when a pusher comes into a contact while the top portion of the chip is held fixed. (see figure

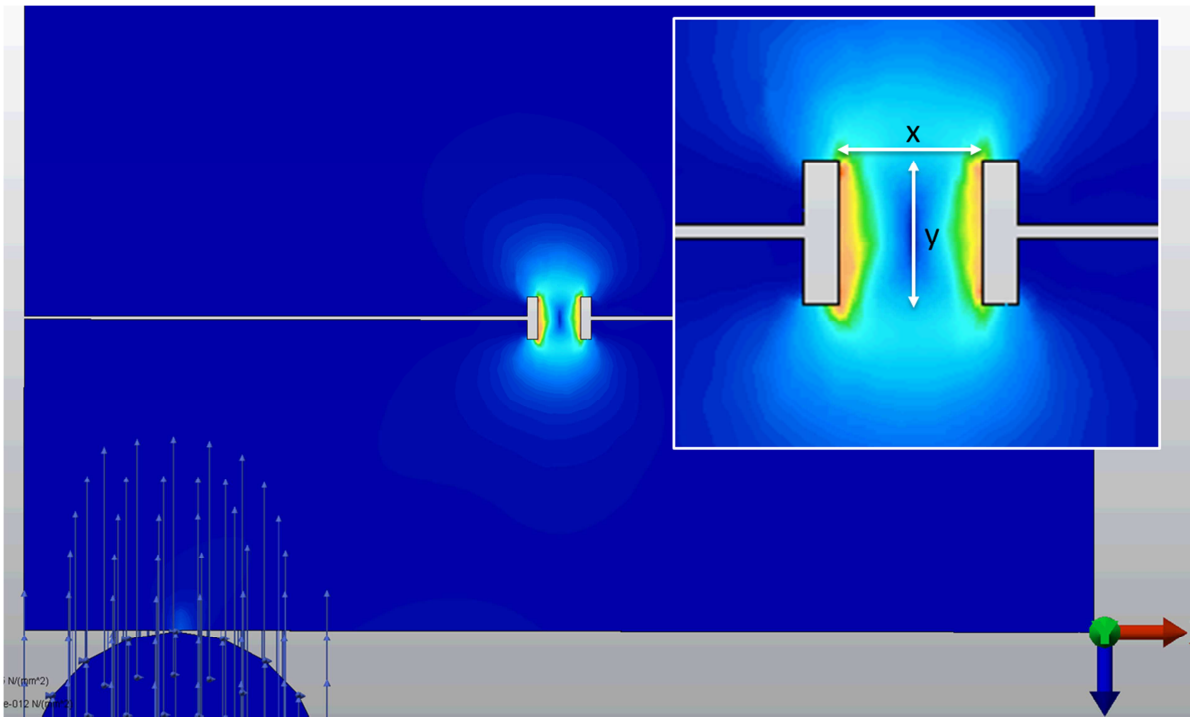

Figure 4-3 Simulation of a Si paddle response under load using finite element analysis. 1 cm^2 chip (500 µm thick)with the top portion fixed. Here the hinge dimensions are x=500 µm and y=500 µm. (inset) Colors correspond to the stress distribution. Here the response is nearly symmetrical around the hinge.

4-3) The hinge is characterized by two parameters, x and y. (see inset, figure 4-3) In the limit of $x/y \gg 1$, the two ends of the paddle become decoupled, meaning only the pushed side of the paddle responds while other remains still. In the opposite limit $x/y \ll 1$, it becomes difficult to apply strictly uniaxial length change as the paddle is prone to sliding in the x-direction. Symmetric motion – equal and opposite displacement of the slit widths on the opposite sides of the hinge – about the hinge is desirable since we always deflect the laser from one side of the chip. That way, one calibration suffices for pushing either side. (see section 4.6 for the method of measurement) A smaller, more point-like hinge would bend in nearly symmetric manner because most of the bending is concentrated at the hinge. If the hinge is very stiff against the

bending motion, the bending motion is distributed throughout the hinge and the paddle on the side that is pushed, which produces asymmetry. But a reduction in the size of the hinge comes at the price of strength and rigidity; the clamped nanobeam must remain intact through the fabrication process. If x is significantly larger than the thickness of the substrate, $t = 500\ \mu\text{m}$, bending out-of-plane is a possibility. This can be a problem when performing optical measurements because the nanobeam may shift away from the focal plane of the optical microscope. After all of these considerations, appropriate dimensions were chosen and drawn on KLayout as well as AutoCAD for 4-inch wafers.

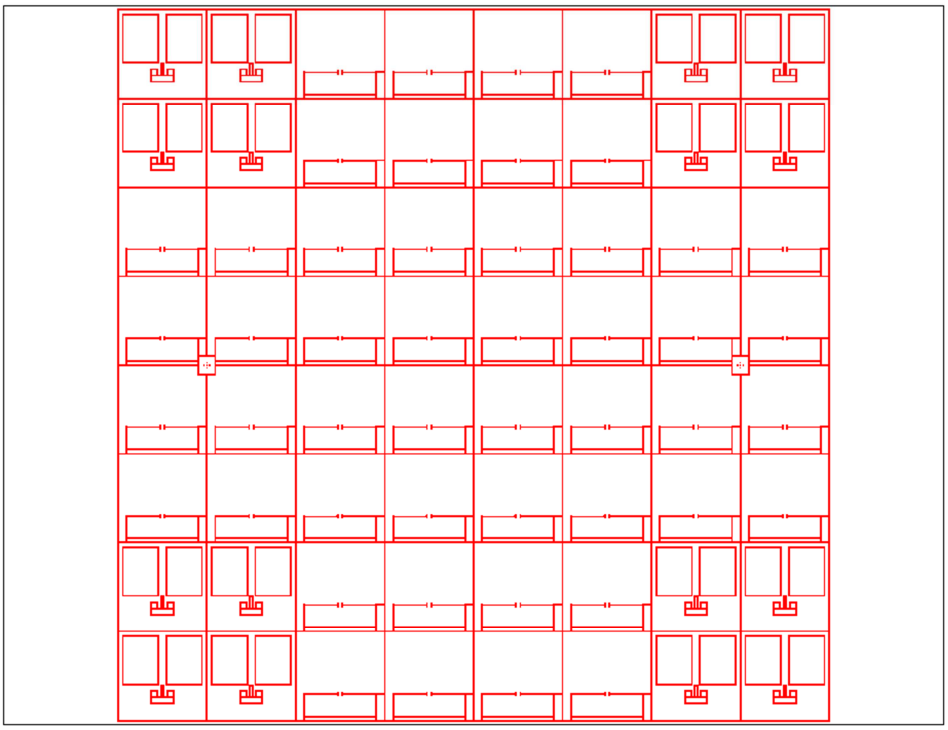

Figure 4-4 Mask design. 80 mm by 80 mm design for a 4-inch wafer. The design has sixty four 1 cm^2 Si chips: device chips (48) and shadow masks (16). Two masks, front and back, are required for back-aligned photolithography.

The (micro- and macro-) loading effects[85] involved in deep silicon etching[86] made it impossible to prepare the device chips in a single run. In order to etch through $t = 500\ \mu m$ wafers with ability to prepare fine features of several microns, double-side etching method (see figure 4-5) was used. Two masks were prepared (Heidelberg µPG 101) for back-aligned photolithography (Karl-Suss MA-BA-6). The backside mask consisted of thick lines with uniform widths ($100\ \mu m$) such that bulk of the wafer (about $450\ \mu m$ out of $500\ \mu m$) could be etched quickly and uniformly whereas the front-side pattern consisted of desired slit sizes and fine features where necessary. The masks were prepared at the UW Nanofabrication Facility and sent to UCSB Nanofabrication Facility where photolithography and dry etching (SiRIE Based Flourine Etcher for Bosch MEMS Processes) were performed. The detailed step-by-step procedure of the fabrication process is available in the appendix.

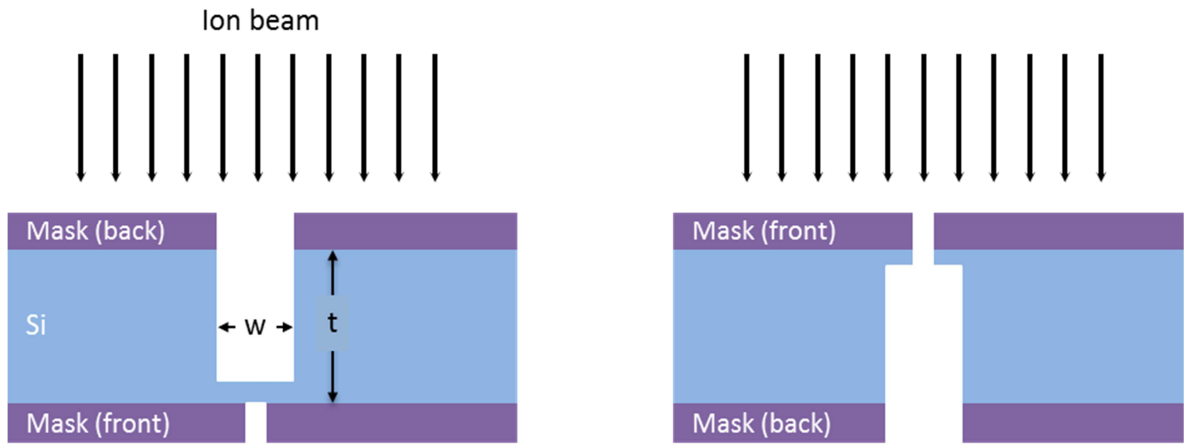

Figure 4-5 DRIE fabrication process. Starting from $t = 500\ \mu m$, the bulk of silicon is etched from the back. $w = 100\ \mu m$ on the backside. Then the whole wafer is flipped and etched again on the front side.

A fabricated Si chip is shown on figure 4-6. One side of the paddle is open to a laser beam exposure that deflects off the side wall, measuring the motion of the paddle by using the principle of optical lever[87] or autocollimator. As we will see, the etched sidewall of Si has nearly specular reflection, allowing a direct relationship between the deflection angle of the laser beam and the motion of the paddle. (section 4.6)

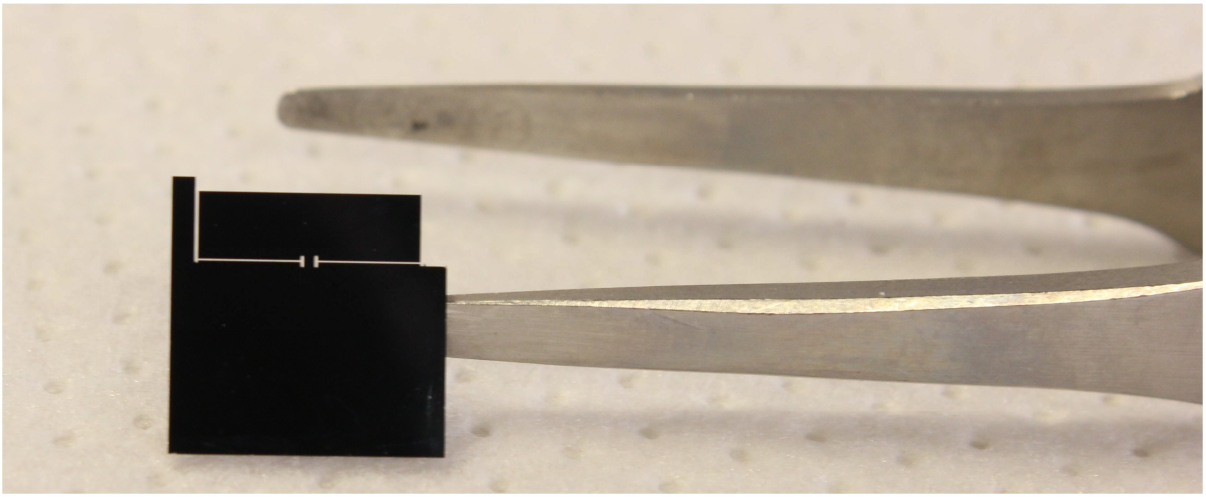

Figure 4-6 Si paddle chip. A silicon paddle chip (1 cm^2) with 40 μm wide slits is shown.

4.3 Transferring VO_2 crystals

Most experiments are limited not only in the number of things that can be measured but also with the range and resolution of that which is being measured. Therefore the different aspects of a physical process, though they may originate from the same physics, are measured with a variety of specialized experiments that dictate the experimental geometry. In optics for example, transmission studies require that the sample is suspended or placed on a transparent substrate. The types of experiment may also dictate the use of either insulating or conducting

substrate. Furthermore, the preparation of a sample in certain position and/or orientation may greatly benefit the experimentation and the analysis of the measured data. Therefore we developed a number of techniques for manipulating the position and orientation of our grown VO_2 crystals, as well as transferring them between different substrates, for use in various experiments.

Our most extensively used method is direct manipulation of a single VO_2 nanobeam using a 3-axis stepper-controlled motorized manipulator. (Märzhäuser SM 3.25, 25 nm resolution) The manipulator is mounted on a microscope stage for in-situ transferring.

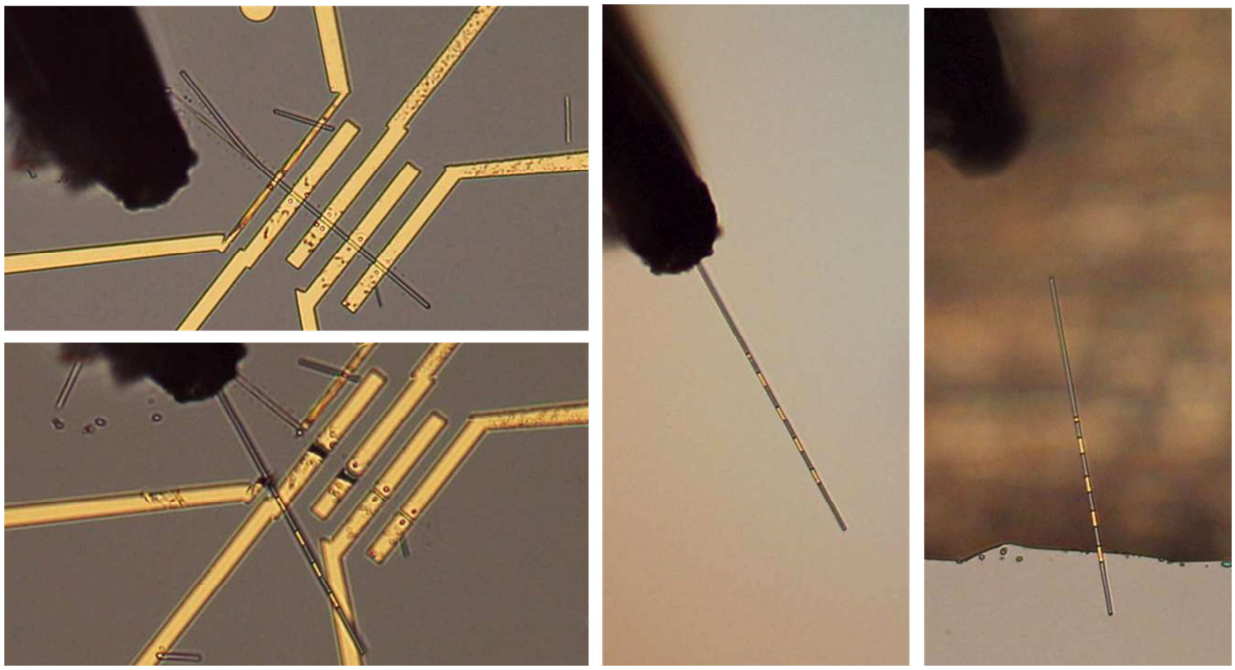

Figure 4-7 Microscope images of transfer procedure.

Since VO_2 nanobeams grow pinned to the oxide surface, they are first loosened with a light BOE etching. A nanobeam is then picked up probably due to a van der Waals attraction,

using a probe needle (usually tungsten needle from Quater Research) attached to the manipulator. Most of our devices for the strain project were prepared this way.

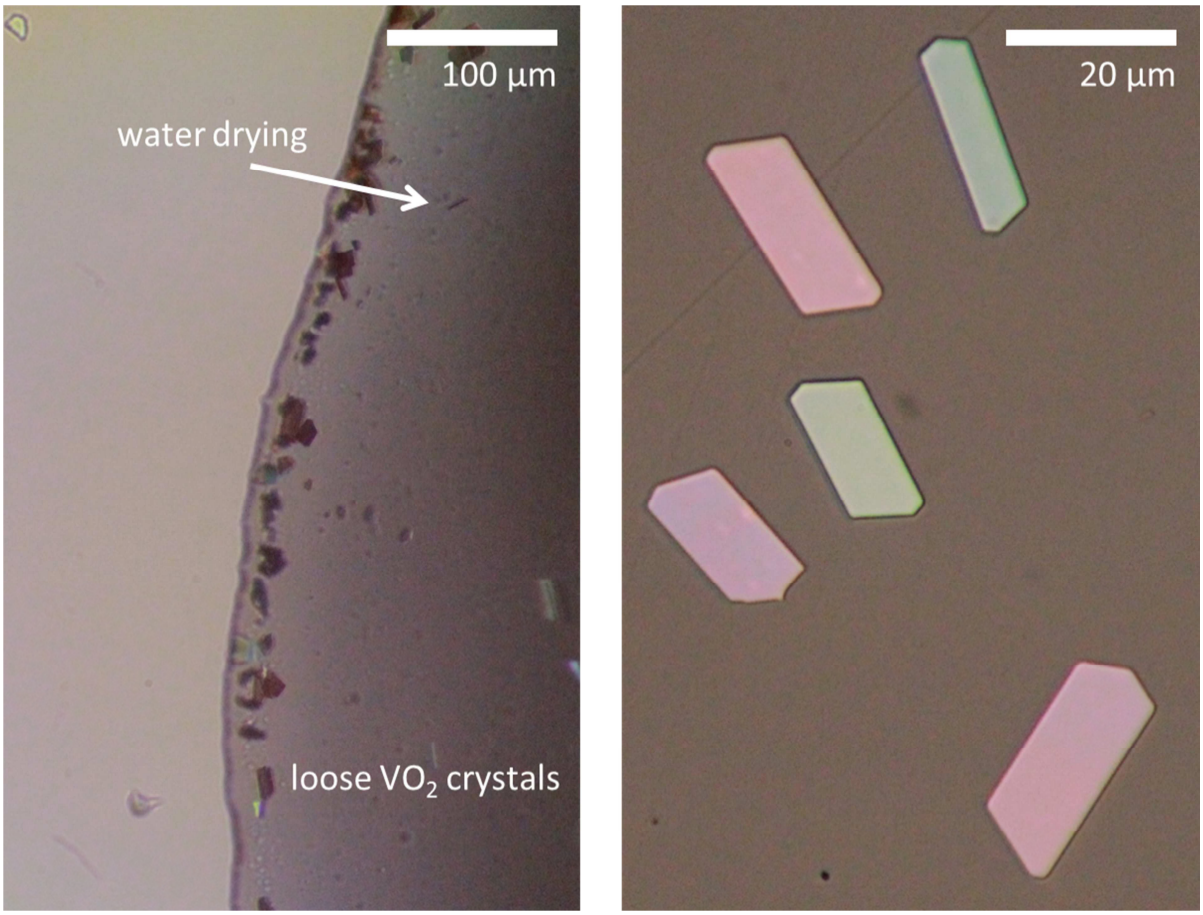

Figure 4-8 PVA Transfer. Microscope image of floating VO_2 crystals after PVA is dissolved in water. (left) VO_2 crystals are placed loose on a sapphire substrate. (right)

The previously described method works well with most nanobeams but fails when transferring a crystal of large area – what we call VO_2 sheets. In such cases, we used polyvinyl alcohol (PVA) tapes (3M 5414) that dissolve in water. Again, the sheets of VO_2 crystals are loosened first with BOE. (takes a bit longer than the nanobeam case) Then a strip of PVA tape is rubbed over the silicon chip and peeled off. The strip with VO_2 crystals is applied to a new

substrate of choice, which is then put in warm water that dissolves the PVA. Finally after rinsing with water, the VO_2 crystals are placed on a new substrate. This method is best for transferring a large number of nanocrystals when a precise placement is not necessary. The samples prepared this way were used for ultrafast pump-probe measurements in collaboration with Aaron Jones in Professor Xu's group[88].

In some cases, it was necessary to transfer a specific nanocrystal onto certain location but the crystal may be too small to be picked with a needle. So a combination of PVA and PMMA was used to transfer the sample, using the method[89] for transferring a graphene sheet made famous by Hone's group at Columbia.

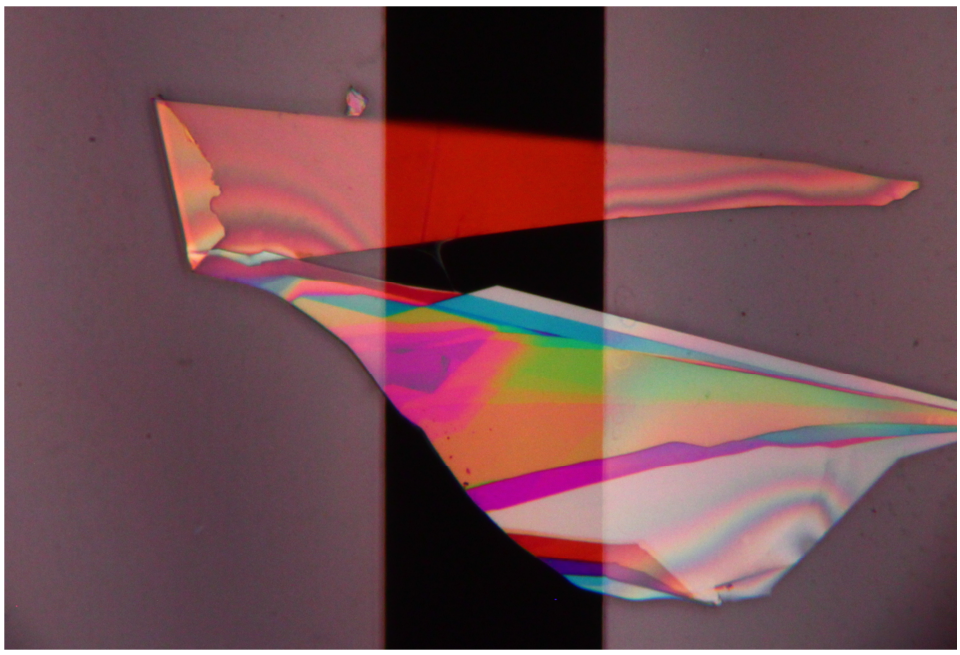

Figure 4-9 Boron nitride suspended on a 40 µm slit. hexagona-boron nitride (hBN) was exfoliated onto a Si chip spincoated with PVA and PMMA. The thin film of PMMA with h-BN, after dissolving PVA and liftoff, can be positioned and deposited onto a desired location, in this case a 40 µm slit, under a microscope. (see text for the reference to the method)

4.4 Adhesion

It is imperative that the change in the slit width accurately corresponds to the change in the length of the nanobeam. This is very important point as we infer the strain in a nanobeam by measuring the gap change. In other words, a good adhesion is necessary for our measurement to be physically significant. Therefore both ends of a nanobeam across the slit must be fixed down firmly. Not only is it important that we know how to fix the nanobeam but also know exactly how well it works. Luckily the MIT in VO_2 provides the solution. A VO_2 nanobeam under a length constraint demonstrates coexistence at the phase transition. An applied length change induces the interface motion by an amount consistent with both the length change and the fractional change in the lattice constants of the two phases involved. (section 2.4) Therefore whether a proper adhesion is made can be checked by observing coexistence. If no coexistence is observed, this indicates that the nanobeam's length is not constrained, probably loose on at least one end. Indeed coexistence is only observed in devices with some degree of adhesion between the nanobeam and substrate. A question then is the quality of the adhesion. Therefore the position of the interface, nucleation process, and domain formation are recorded extensively for a number of transitions for each fabricated device. We infer good adhesion in a device by testing its reproducibility over countless thermal cycling and repeated application of length change. As we will see in section 4.6, a device with good adhesion not only shows reproducibility but also an excellent agreement with the expected response of the interface motion for a given width change in the slit.

There are various methods to bonding a VO_2 nanobeam to its substrate. They include growth, regrowth, annealing in vacuum, and epoxy. Each method has pros and cons in terms of ease of application, curing procedure, flexibility/compatibility, strength of adhesion, procedure difficulty, time, and cost. For our purpose, UV curable epoxy was the best option for its convenience above all other methods though other methods would have worked equally as well.

The direct growth of VO_2 on SiO_2 surface produces the nanobeams that are firmly stuck on the substrate. (section 2.2) The possibility of growing nanobeams across the slit was explored by performing the synthesis on the Si paddle chips. The main advantage of this method is the absence of any processing or chemical for adhesion.

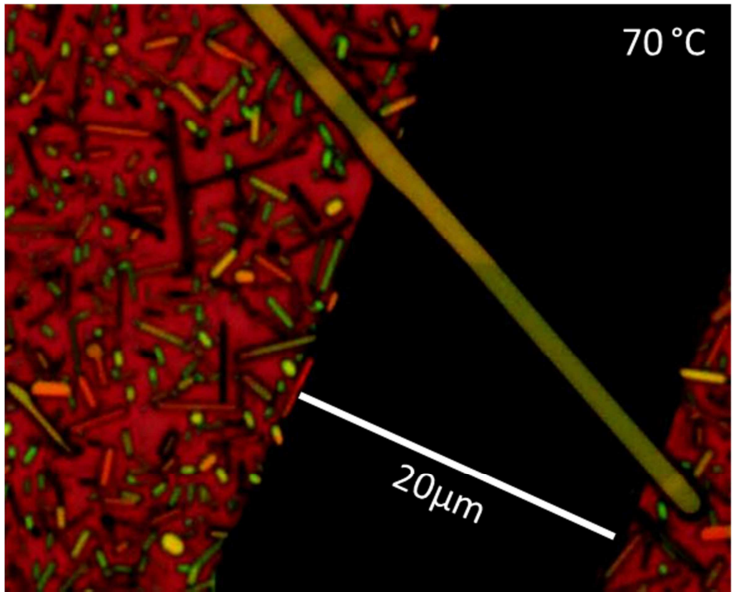

Figure 4-10 Microscope image of a VO_2 nanobeam across a slit. The nanobeam is grown across the 20 μm wide slit, firmly attached at both ends. (otherwise it would not have a coexistence) This method suffers from extremely low probability of success, not to mention poor orientation of the nanobeam that is uncontrollable.

But hundreds of growth produced maybe a couple of nanobeams that may have worked. (see figure 4-10, one of a few successes) Besides the extremely low success rate, the few nanobeams that managed to grow across the gap were almost always useless because of their poor orientation relative to the slit and non-uniform cross-section as seen on figure 4-11.

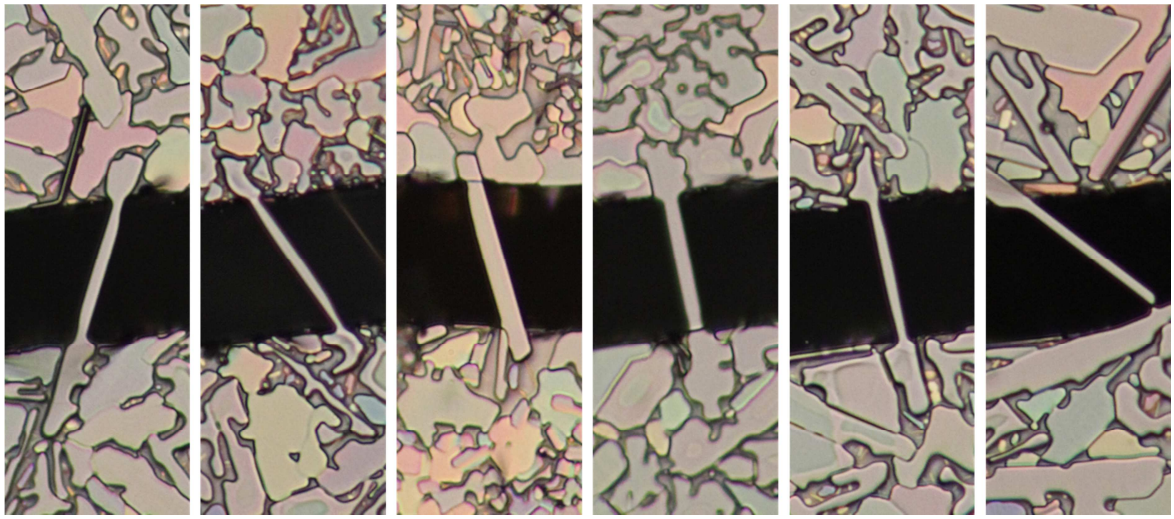

Figure 4-11 As-grown VO_2 nanobeams on the slits. (20 μm gap) Growth #512 shows various VO_2 nanobeams that could have been suspended devices. But their poor orientation (not perpendicular to the slit) and non-uniform cross-section prevent a serious consideration of using the direct growth method.

The idea of regrowth from the section 3.3 is incorporated with transfer technique discussed in section 4.3 to overcome the above shortfalls. The twist is transferring a VO_2 nanobeam of our choice onto a precise position and orientation on a pristine Si paddle chip prior to VO_2 synthesis. Knowing a VO_2 nanobeam grows firmly attached on an oxide surface, it was speculated that the same type of bonding that took place during the growth would occur between the transferred nanobeam and the SiO_2 surface. Growth parameters with lower oven temperature (700-800 °C) and less V_2O_5 source amount were used to avoid overgrowth. At

lower temperatures, metal films have higher chance of survival, in other words metal contacts may be prepared prior to a growth, adding flexibility in fabrication procedure. Also we prefer for the nanobeam to stay its size and not get too large to avoid domain structure. The very first device made this way is shown in figure 4-12.

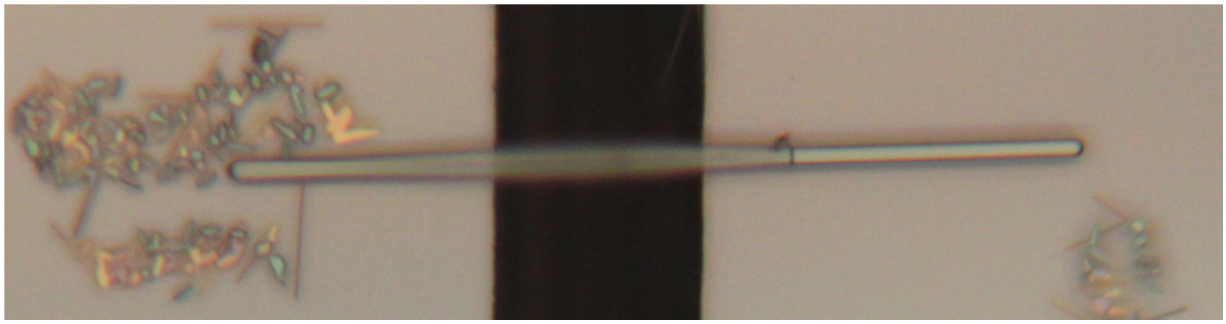

Figure 4-12 Regrowth on a transferred VO_2 nanobeam. A VO_2 nanobeam is transferred from another growth chip to a pristine Si paddle chip and subsequently undergoes a VO_2 synthesis. The pre-existing nanobeam grows on the oxide surface, bonding with the SiO_2 as in an original growth. The clusters of tiny crystals are the results of the second growth. The devices made this way show Euler buckling.

The devices that are made with the two previous methods show Euler buckling because those nanobeams were bonded to the substrate at high temperatures. As they cool from 1000 °C, the metallic phase in VO_2 experiences an increasing tension due to the greater thermal expansion coefficient than the Si substrate. The suspended VO_2 nanobeam then experiences coexistence when an insulating domain nucleates around T_c. Finally, when the nanobeam turns fully insulating, sudden one-percent length expansion actually puts the beam at compression, causing Euler buckling. The nanobeam remains buckled until the MIT. A more significant problem is that the cross-section size of nanobeam was not a controllable parameter. Even if

we started with a nanobeam of desirable dimensions, the regrowth could make the crystal too large to work with.

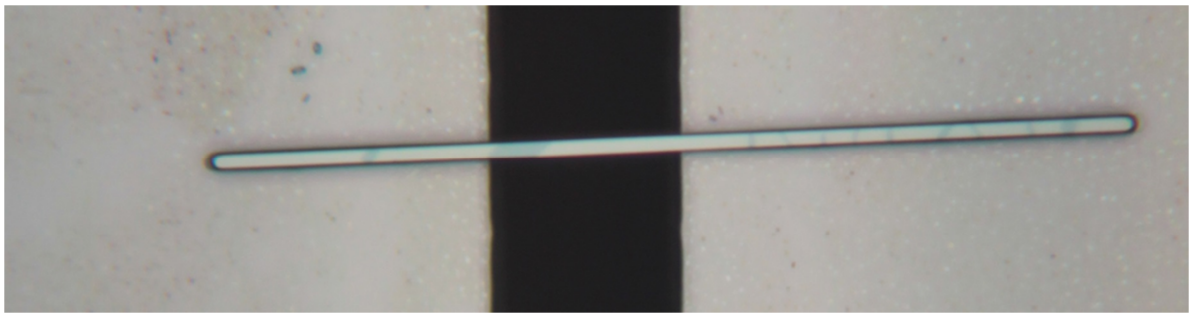

Figure 4-13 Transferred VO_2 nanobeam on a paddle chip with spincoated TEOS. TEOS was spincoated on a paddle chip before transferring a VO_2 nanobeam. The chip, after proper positioning of the nanobeam, is placed in an oven in vacuum and annealed above 600 °C, at which TEOS decomposes into SiO_2 providing adhesion between the nanobeam and the substrate.

In some cases, tetraethyl orthosilicate (TEOS) was spin-coated onto the Si chip before transferring devices. Above 600 °C, TEOS decomposes into silicon dioxide and diethyl ether

$$\mathrm{Si(OC_2H_5)_4 \rightarrow SiO_2 + 2(C_2H_5)_2O}$$

Several improvements over the previous methods are the lower temperature, no need to use the V_2O_5 source, and therefore no change in the size of the transferred nanobeam. But the sticky nature of TEOS hindered the maneuvering of the nanobeam once it landed on the chip, making it difficult to orient with ease. The consistency of the adhesion was also an issue, probably because the spincoated film near the edges is not very uniform.

Epoxies come in many forms because of their varied functions. Most epoxies require mixing with a resin, which activates the curing agent and hardens the epoxy over time. Once

curing agents activate, the viscosity of epoxy quickly changes and its application on small objects like our nanobeams becomes increasingly difficult, if not impossible. For our purpose, a UV curable epoxy (Norland NEA121) was an ideal candidate for several reasons. i) It was chosen for its appropriate viscosity (300 cps, comparable to a motor oil). Too low, it runs everywhere. Too high, it goes nowhere. ii) There is no need to mix with a resin. iii) It is not solvent-based. The viscosity does not change while using it. iv) The curing process can be initiated by either UV light or heat. Without UV source or heat, the epoxy does not cure, allowing a plenty of time for application and other procedures. v) The epoxy is optically clear. This allows visual inspection of the domains under epoxy.

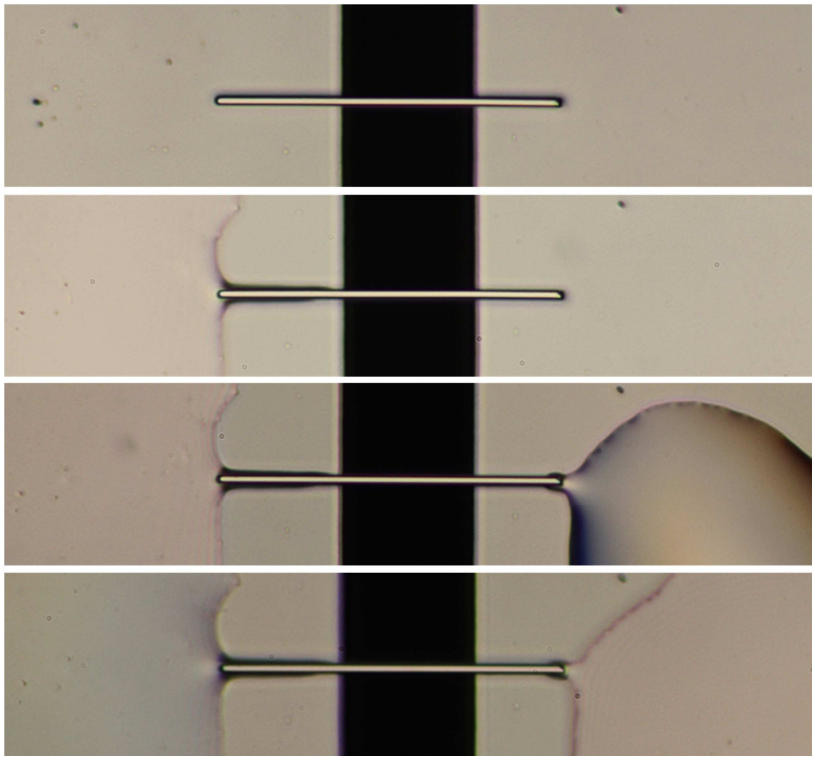

Figure 4-14 Application of UV curable epoxy on a VO_2 nanobeam. (20 μm gap) Epoxy is applied on both ends of the VO_2 nanobeam suspended across a slit. Epoxy wicks along the sides of the nanobeam and stops at the slit edge.

Using a needle mounted on a nanomanipulator, an epoxy puddle is drawn near to an end of the nanobeam. Epoxy wicks along the sides of the nanobeam upon contacting and stops at the edge of the slit due to surface tension. The chip is then placed in a UV light source for ten minutes and subsequently heated at 80 °C for more than three hours for curing. The whole process is conveniently performed without the use of the tube furnace or vacuum system and allows visual inspection in between steps for a better quality control. But once the nanobeam is coated in epoxy, which is insulating, electrical contacts cannot be made. So the electrical contacts should be made prior to the adhesion.

4.5 Metal contacts

Metal contacts to a VO_2 nanobeam are necessary for measuring the resistance, which is sensitive to its phase composition. A careful analysis of the change in resistance as a function of both length change and temperature should yield useful parameters such as the strain dependent gap and the respective resistivity in different phases. Metal films are usually deposited, either by sputtering or evaporation, to produce electrical contacts on a sample after patterning. As it turns out, the Si paddle chips were incompatible with some of the procedures involved in the standard patterning process. First, spincoating a resist of uniform thickness proved to be difficult near the slits. Second, spincoating of a resist caused the transferred a nanobeam to disappear or shift its position. Third, the hinge was prone to cracking during the lithography procedure. A different approach was needed. In 1975 Fisher utilized drops of indium amalgam to make electrical contacts to a VO_2 needle[90]. Indium is a soft metal with the low melting point of 156.6 °C. A sharp needle of indium can be prepared by first dipping a

tungsten needle in a puddle of molten indium and slowly retracting the tungsten needle out with some molten indium that cools and solidifies into a sharp needle. The indium needle is then positioned above the VO_2 nanobeam sitting on a hot surface, usually a Si chip with prefabricated gold pads for probe tips or gold ball wirebonds. As the indium needle is lowered, the indium melts onto the nanobeam and the substrate. Indium forms an alloy with gold but does not stick well to the SiO_2 surface. All of this is done with a nanomanipulator mounted under a microscope equipped with a heating stage.

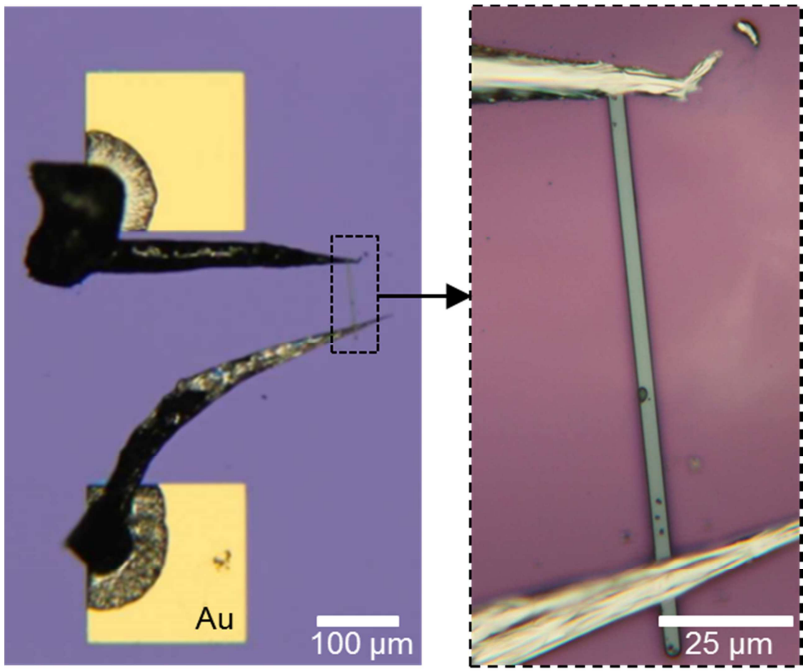

Figure 4-15 VO_2 nanobeam contacted by indium needles. A VO_2 nanobeam is transferred to a SiO_2/Si substrate with pre-patterned gold contact pads. Indium needles connect the ends of the nanobeam to two separate gold pads that can be contacted by probing tips or wirebonded into a package.

Figure 4-15 shows a typical VO_2 nanobeam contacted by indium. The nanobeam with only indium metal contacts generally shows no coexistence, turning completely metallic upon

heating. In some devices with thin indium strips, the conductance was lost probably due to oxidation as suggested by discoloration of the contacts. In some devices with thick strips of indium, there was no observable change in the resistance of the device over months. Figure 4-16 shows a typical resistance versus temperature curve, showing the MIT.

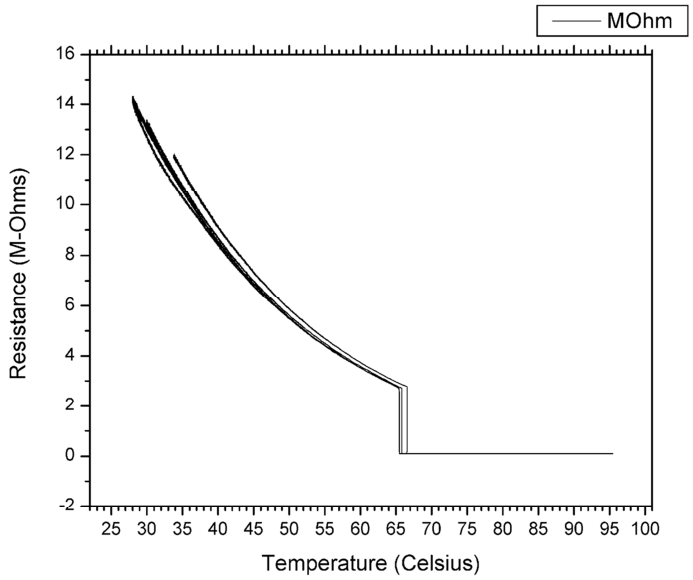

Figure 4-16 Resistance versus temperature plot of a VO_2 nanobeam contacted with indium. (the device from figure 4-15) As mentioned in section 2.3, the result is reproducible over multiple thermal cycling without degradation.

Platinum deposition by either electron beam deposition (EBD) or focused ion beam deposition (FIB) offers an alternative approach to contacting the sample. These methods offer greater control on the shape and size of the deposited metal and, unlike indium, have been used in anchoring applications[59,83]. But there is a concern of sample damage from the energetic ions. Fracture of the deposited metal (made by EBD) was common at the MIT.

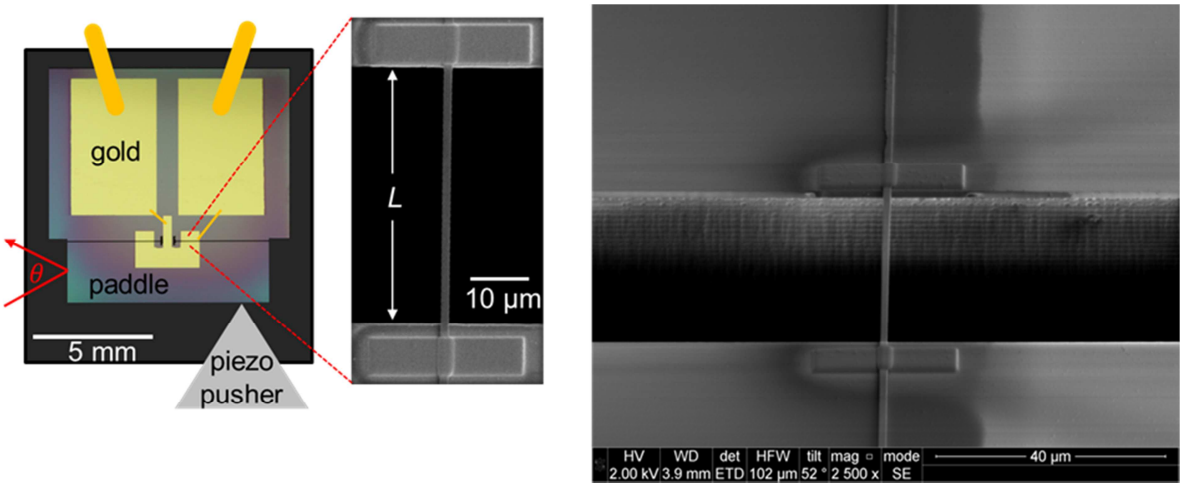

Figure 4-17 Device with EBD electrodes. On a Si paddle chip with shadow-evaporated gold pads, a VO_2 nanobeam is transferred and subsequently anchored with FIB-assisted Pt deposition. Yellow lines indicate gold wirebonds.

Beam deposition methods were outsourced at Cornell and Oregon. Due to the high cost, logistics, and time delay involved in the process, molten indium was the preferred method. With indium contacts, there was an added step of epoxy application to clamp down the nanobeam that was significantly more reliable than any of the metal deposition methods.

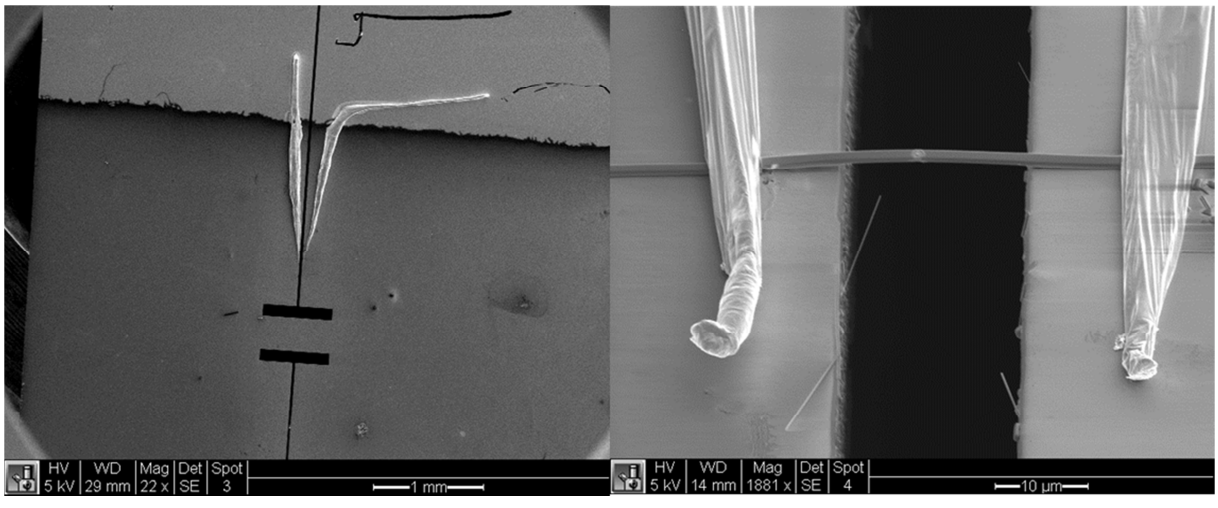

Figure 4-18 SEM image of a device with indium contacts.

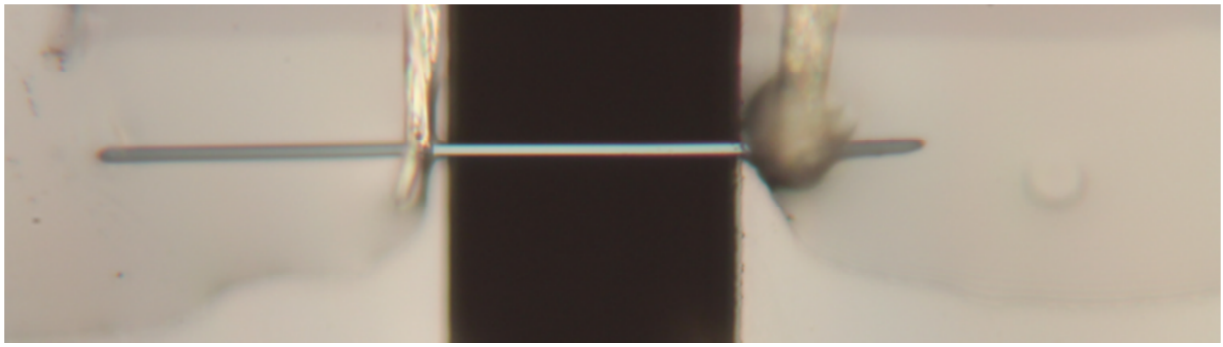

Figure 4-19 VO_2 nanobeam device with indium contacts and epoxy adhesion. (40 μm slit)

4.6 Measurement and control of length change

The slot width is controlled by displacing the paddle which rotates around the thin hinge stalk. The paddle is pushed using a pusher mounted on a single-axis horizontal piezo-actuator (Physik Instrumente P-611.1) and the slot width can be increased or decreased by pushing on either one or other side of the paddle. (see figure 4-19) The pusher is made out of steel for its strength and relatively low thermal conductivity since the piezo-actuator has a limited temperature range and the heater is a few centimeters away. The piezo-actuator is controlled by a computer software, using a series of DAQ card and voltage amplifier.

A collimated and intensity-modulated laser diode beam is reflected from the side wall of the paddle and its deflection measured using a position sensitive detector (PSD, OSI Optoelectronics Duo Lateral SL5-2), to detect the angular deflection of the paddle. The PSD signal modulation is calibrated to the slot width by recording the full-range deflection of the paddle which can be seen in the microscope. The setup could also be retrospectively calibrated

using measurements such as those in figure 5-4 of the coexistence interface position combined with the known lattice constants of the phases.

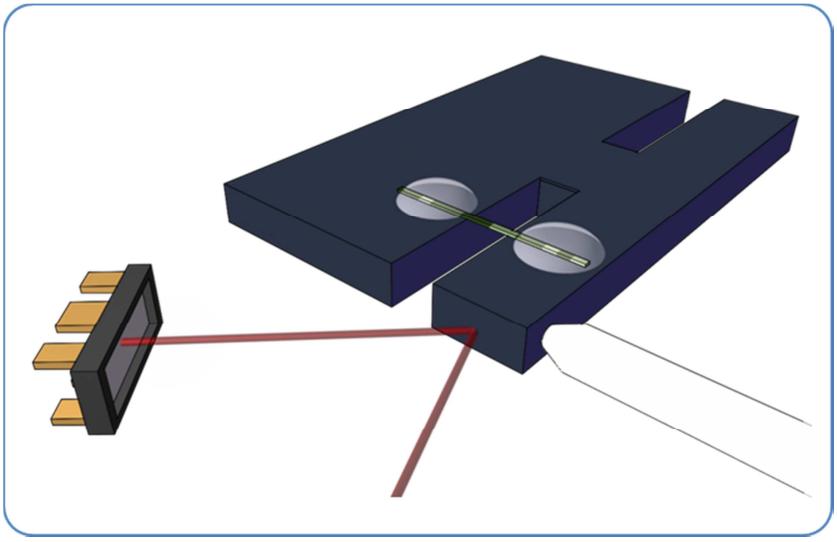

Figure 4-20 Simplified illustration of the length measurement. The point of contact between the Si paddle and pusher may degrade over repeated application of stress. In other words, the measurement of length change cannot be substituted with the motion of the closed-loop piezo. Our method does not suffer from this since we measure the gap directly.

The overall layout of the optoelectronic components is illustrated in figure 4-20. A 50/50 beam splitter (non-polarizing, thorlabs BS016) is used for compactness, where the beam path length is to be maximized in a given dimensional constraints. (optical lever principle) The quartz tube placed in between the beam splitter and the Si paddle chip is a crucial element that prevents the convection or turbulence of hot air around the heating stage from interfering with the laser signal[87].

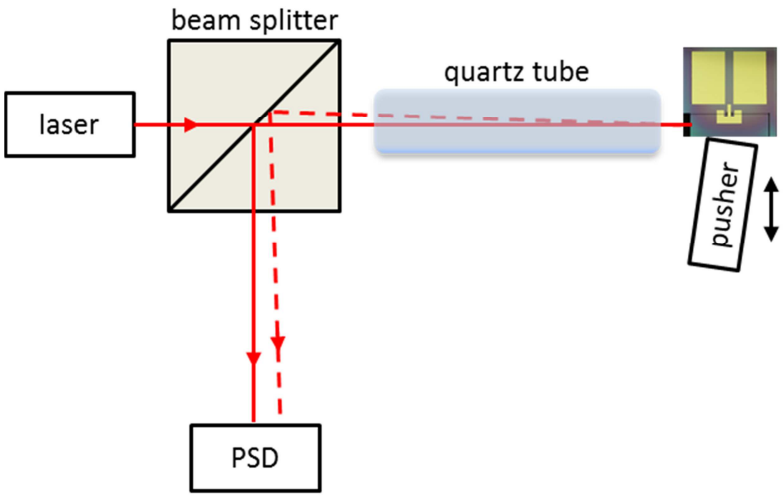

Figure 4-21 Optoelectronics for the measurement of length change. Components for the laser deflection measurement are shown. All the components are fixed in space except the PSD, which sits on a translation stage for adjusting position offsets. The pusher is mounted on a piezo-actuator and can rotate to push on either side.

The main advantage of using a PSD is the output linearity with the position displacement and insensitivity to the beam shape. Figure 4-22 shows the electrical layout behind the PSD measurement. A photon creates an electron-hole pair, which is then separated by the electric field in the depletion region. The flow of these charges produces a current that can be measured in voltages via operational amplifiers (LMC6082). The amount of measured current depends on the position of the pair creation relative to the metal contact. If the laser beam is closer to one of the contacts, more current is generated there simply due to a greater number of pair generations in the vicinity, which creates an imbalance between i_1 and i_2. In order to isolate from the ambient light source, a lock-in technique was utilized.

Finally, active control of the nanobeam length and accurate measurement of the gap width allow, for the first time, active control of the phase transition in VO_2 with high

reproducibility. Our method does not suffer from the degrading point of contact between the pusher and the Si paddle since we directly measure the quantity that is proportional to the gap width, not the piezo-actuator motion.

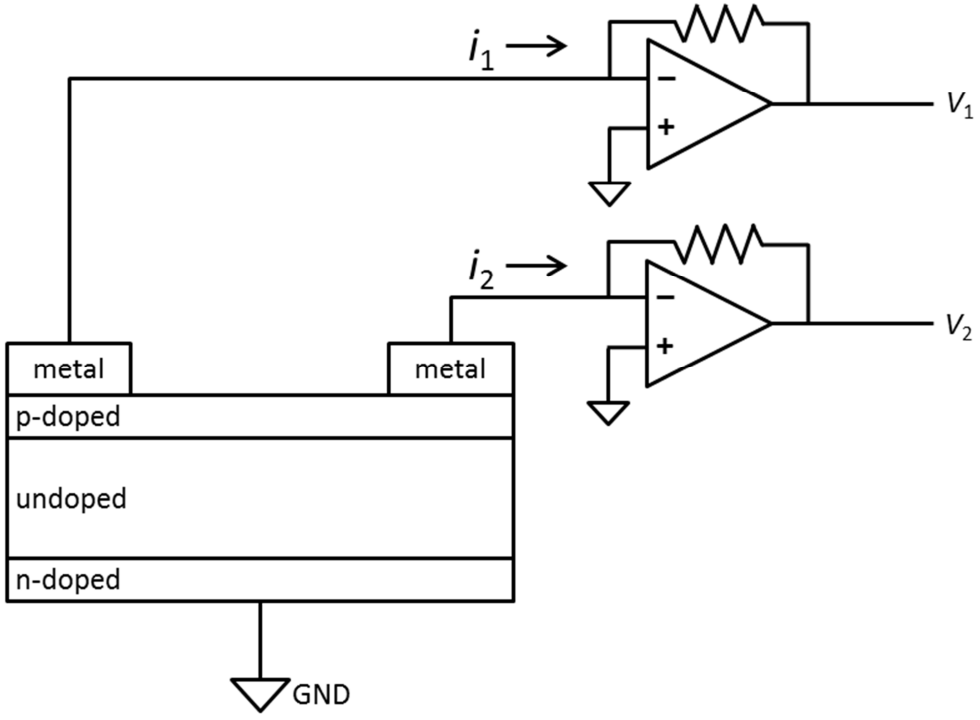

Figure 4-22 PSD measurement. Op-Amps (LMC6082) and 5 MΩ resistors were used to convert the output currents into voltage signals that were fed into a DAQ card. The voltage difference V_1-V_2 is directly proportional to the laser position.

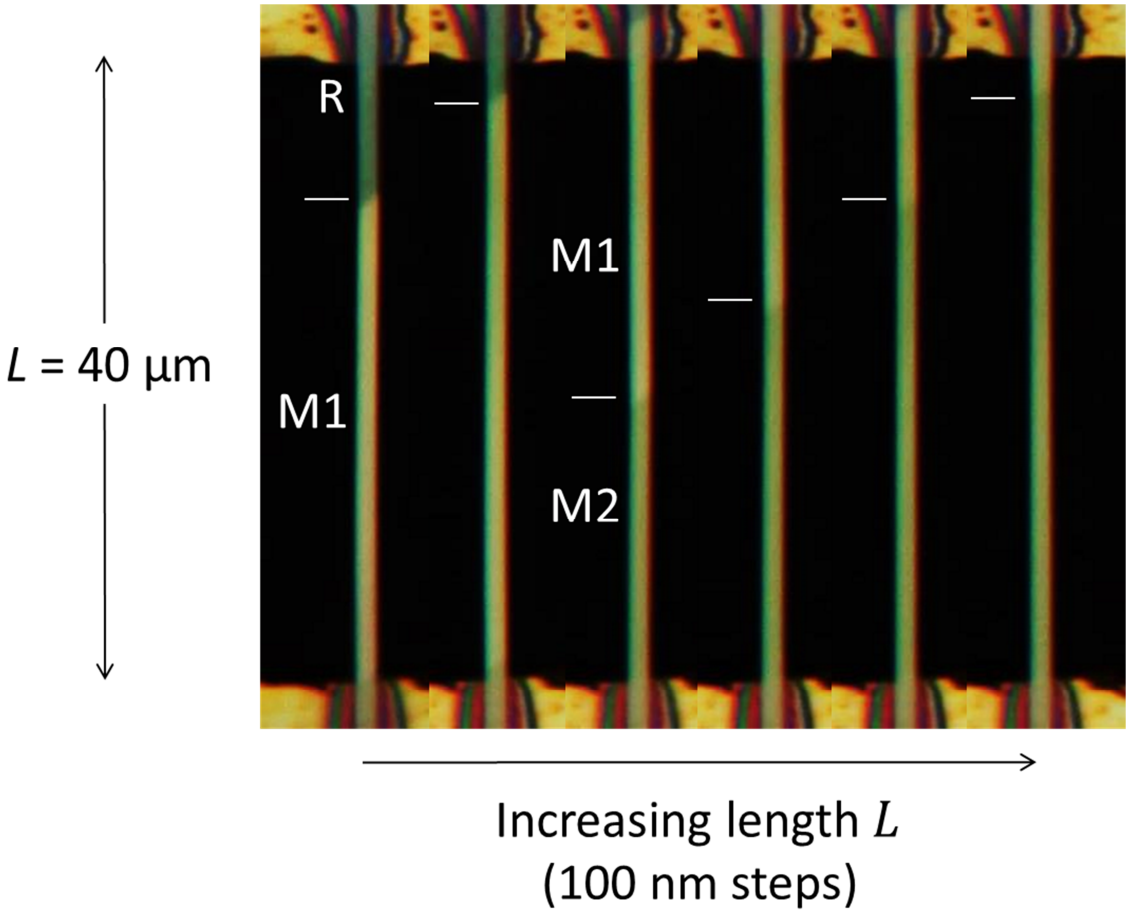

Figure 4-23 Active control of the length. (Device P7, 64 °C) Series of optical images showing movement of the M1-R and M2-M1 interfaces as L is increased.

4.7 Measurement and control of temperature

The home-built heating stage is made out of an invar block to minimize thermal expansion. The stage is fixed at the top by screws such that the top plane of the stage stays nearly fixed even when thermal expansion occurs. A heater (6W resistor) and sensor (PT100) are separately embedded in the block and the temperature is actively controlled. Several PT100

platinum sensors were configured for four-terminal sensing and calibrated against the melting and boiling points of water. Their readings were found to be accurate to within 0.1 °C. One sensor was embedded in the invar stage and the wires were anchored on the thermal stage to minimize the heat transfer the wires away from the sensor. The stability of the measured temperature was better than ±0.05 °C.

To correct for a temperature differential between the sample and sensor, due mainly to heat loss to the surrounding air, we placed small oil-coated crystals of the metals gallium (melting point 29.77 °C) and potassium (63.38 °C) on a silicon chip close to a nanobeam. Their melting could be seen under the microscope, and the calibration of the system was adjusted accordingly. This procedure was carried out on several chips. In this way the temperature difference between the chip body and the paddle was found to be less than 0.1 °C.

5 Phase Diagram of VO_2

As discussed in section 2.6, the phase boundary slope dP/dT can be calculated from measuring the quantity dy/dT in phase coexistence. Three slopes obtained this way do not suffice to complete the phase diagram because even if the triple point temperature can be known, the pressure at the triple point remains unknown. The main purpose of the setup is an application of controlled length change, which is not the same as controlling the absolute value of the uniaxial stress along the nanobeam. Though we cannot directly measure the stress, it is possible to prepare the system in a way that the stress is always zero. Once all that can be measured has been extracted from a device, the nanobeam is purposely broken to produce two opposing cantilevers. Carefully measuring the transition temperature at zero stress, T_c, provides an absolute pressure calibration. If T_{tr} and T_c are known, their relative positions dictate the shape of phase stability. For example, if $T_{tr} > T_c$, then M2 phase is stable only under tension, otherwise M2 phase could be stable at a slight compression near T_{tr}. M2 phase is known to be stable under a slight tension, $P_{tr} > 0$. We find that this is not in fact the case and, remarkably, T_{tr} is identical to T_c to within ±0.05 °C, or one part in 10^4 in absolute temperature. We further determine T_c to be 65.0 ± 0.1 °C. In addition we present evidence that in the neighborhood of T_c the M1 phase can distort continuously under tension into the metastable T phase. These discoveries have deep implications for the physics of the MIT, for the interpretation of many measurements on VO_2 crystals and films, and for mastering the transition with a view to applications.

5.1 Measurement of the triple point

The position of the interface changes smoothly and reproducibly with both L and T in between sudden reconfigurations. The MIT in VO_2 is usually studied as a function of T, without paying close attention to strain or to interconversion between M1 and M2. In undoped samples it is seen in the range 65 – 68 ° C, with a hysteresis of several degrees Celsius, and the value of T_c is not known more precisely than this[9,91,92,93,32,11,94]. As T is varied at fixed L we see the behavior shown in figure 5-1, which can be understood with reference to the color-coded lines in the inset phase diagrams.

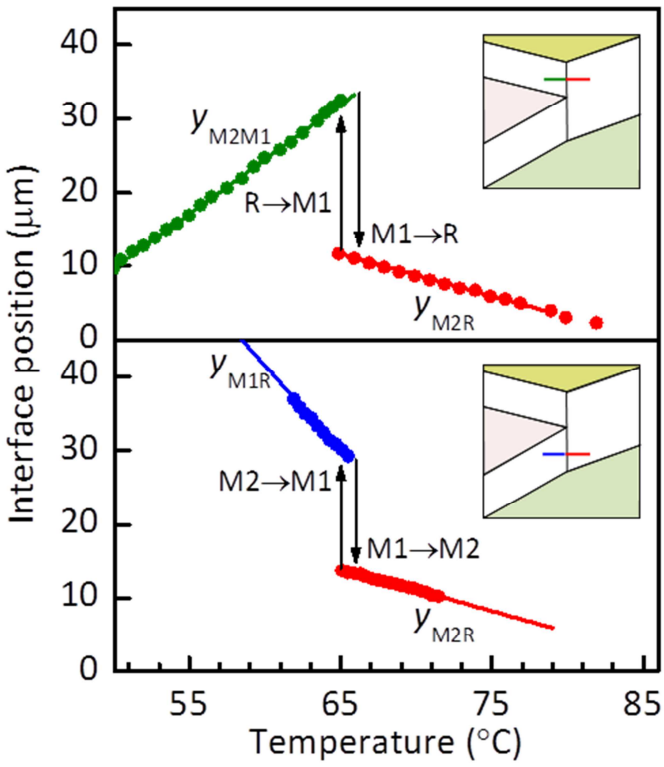

Figure 5-1 Variation of interface positions with T at fixed L. (corresponding to moving along the lines in the insets) The interface position which is measured optically. (see chapter 4) The sudden jump in the interface position indicates a phase transition. (upper: device P11, 40 μm gap; lower: P9, 20 μm gap).

If we start in M2+M1 coexistence (figure 5-1, upper panel, green) and increase T, the interface position y_{M2M1} first moves smoothly as the stress required for phase equilibrium changes[38]. Then at a temperature $T_{\mathrm{M1\rightarrow R}}$ there is a sudden reconfiguration to M2+R coexistence (figure 5-1, upper, red) after which the interface position y_{M2R} moves smoothly again. On cooling, the reverse reconfiguration occurs at temperature $T_{\mathrm{R\rightarrow M1}}$. Starting instead at a smaller length, in M1+R coexistence (figure 5-1, lower panel, blue), a jump to M2+R coexistence (again red) occurs at $T_{\mathrm{M1\rightarrow M2}}$, while the reverse occurs at $T_{\mathrm{M2\rightarrow M1}}$.

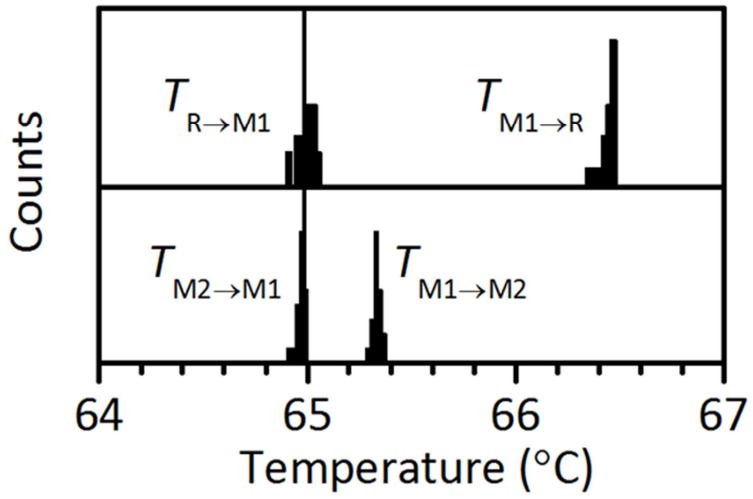

Figure 5-2 Histograms of temperatures at which reconfigurations occur. For 20 cycles sweeping at 0.1 °C min^{-1} (device P14, 40 μm).

Histograms of the reconfiguration temperatures on repeated cycling at 0.1 °C/minute are shown in figure 5-2. For this device $T_{\mathrm{M1\rightarrow R}}$ and $T_{\mathrm{M1\rightarrow M2}}$ are narrowly peaked at 66.4 °C and 65.3 °C respectively; for other devices different values are found. This can be explained by superheating of M1, which varies between devices because the ease of nucleation of the high temperature phase (R or M2) depends on microscopic details.

In contrast, $T_{R\rightarrow M1}$ and $T_{M2\rightarrow M1}$ are both peaked at the same temperature of 65.0 °C, indicated by the dotted line. In a number of nanobeams of different sizes, grown on different occasions, these two temperatures always lay in the narrow range between 64.9 and 65.2 °C; moreover, storage in air for six months, and heating to 200 °C for an hour, did not change them, indicating that effects of oxygen vacancies[95] and hydrogen doping[25] were minimal. This observation can be explained as follows. A small amount of M1 is often visible at the interface in M2+R coexistence, probably because it reduces the elastic energy. On cooling there is therefore no need for nucleation of M1, and reconfiguration occurs as soon as the triple point is reached. In fact, the dynamics of this process can sometimes be observed. Figure 5-3 shows a sequence of images taken in less than a second during the reconfiguration of a nanobeam after bringing it slowly down to 65.0 °C in M2+R coexistence. A small pre-existing wedge of M1 at the M2+R interface rapidly expands to completely replace the R part of the nanobeam. All the above observations thus suggest that the triple-point is between 64.9 and 65.2 °C.

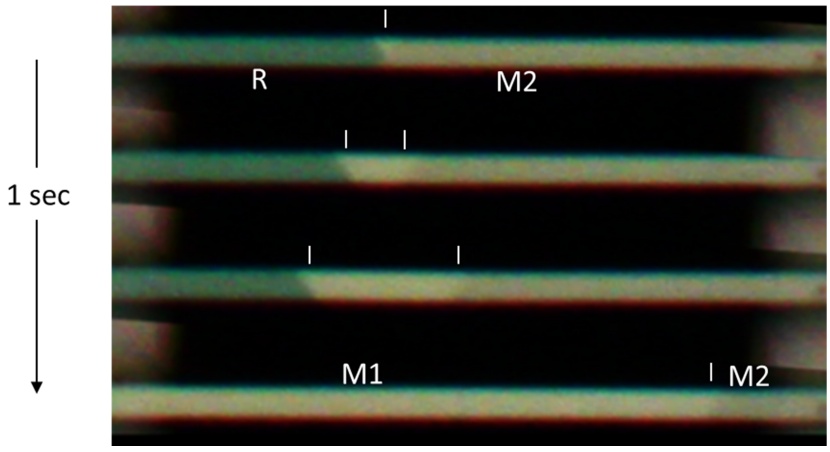

Figure 5-3 Sequence of images during reconfiguration from M2+R to M2+M1 in a nanobeam at the triple point. The bright spot in between R and M2 is M1 domain, which rapidly expands to replace R at 65.0 °C. (P8B, 20 μm).

We now consider varying L at fixed T. First, in coexistence between any pair of phases the interface position is linear in L, as shown in figure 5-4. This follows from the fact that the interface moves so as to maintain P_c at the phase equilibrium value. A length increase δL causes an interface shift δy_{M1R} which changes the natural length by δL to keep the strain constant. This implies $\delta L = \alpha_{\mathrm{M1R}} \delta y_{\mathrm{M1R}}$, where $\alpha_{\mathrm{M1R}} \equiv c_{\mathrm{M1}}/c_{\mathrm{R}} - 1$. (see section 2.4) Hence δy_{M1R} should vary according to $dL/dy_{\mathrm{M1R}} = \alpha_{\mathrm{M1R}}$, and likewise $dL/dy_{\mathrm{M2M1}} = \alpha_{\mathrm{M2M1}} \equiv c_{\mathrm{M2}}/c_{\mathrm{M1}} - 1$ and $dL/dy_{\mathrm{M2R}} = \alpha_{\mathrm{M2R}} \equiv c_{\mathrm{M2}}/c_{\mathrm{R}} - 1 \approx \alpha_{\mathrm{M2M1}} + \alpha_{\mathrm{M1R}}$. Best linear fits to the data shown give $\alpha_{\mathrm{M2M1}} = 0.0074$, $\alpha_{\mathrm{M1R}} = 0.0100$ and $\alpha_{\mathrm{M2R}} = 0.0174$, close to the values of 0.0073, 0.0098, and 0.0172 calculated from the known lattice constants[34,52].

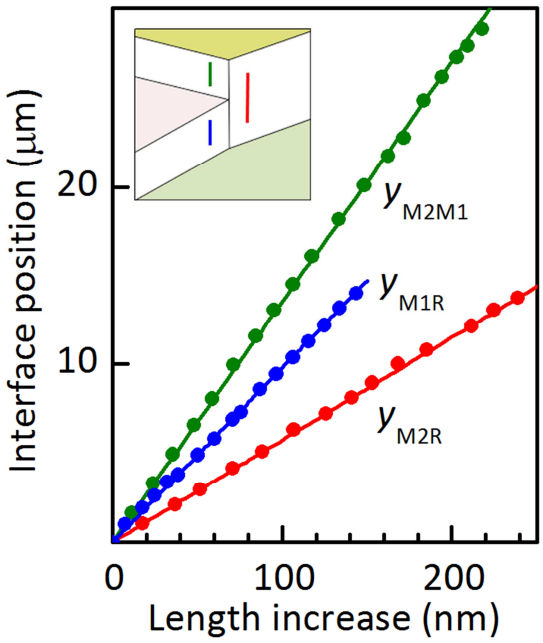

Figure 5-4 Variation of interface positions with L at fixed T. (corresponding to moving along the vertical lines in the inset**)** The inverse of these slopes provide the values for the fractional change in lattice constant.

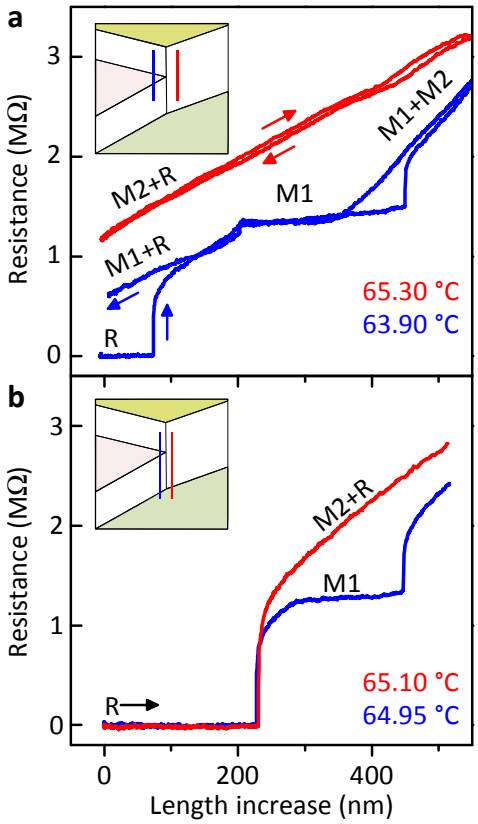

Figure 5-5 Resistance-length measurements at below and above the triple point.

The ability to control L allows us to confirm the temperature of the triple point and to determine the behavior very close to it. We exploit the fact that the electrical resistance R_n (not to be confused with the rutile phase R) is sensitive to the phase composition, since each phase has a different resistivity[38,56]. The measurements in figure 5-5 are for a device (P10) with indium contacts. Figure 5-5a shows that at 65.3 °C R_n changes smoothly with L, due to a smoothly changing M2+R interface position for $T > T_{tr}$ (see inset, red line). In contrast, at 63.9 °C it changes in a more complicated way, reflecting the sequence M1+R→M1→M2+M1 expected for $T < T_{tr}$ (see inset, blue line). Jumps and hysteresis here show that M1 and M2

both require nucleation, consistent with the transitions being first-order. To establish T_{tr} we measured R_n at a series of closely spaced temperatures, each time preparing the nanobeam in a fully metallic R state by cooling at sufficiently small L for R to be stabilized by compression, and then increasing L until an insulating domain nucleated. At 64.95 °C and below, the domain that appeared was always M1, while at 65.10 °C and above it was always M2, implying that T_{tr} was between these two values. This is perfectly consistent with the range of T_{tr} deduced above from the T-sweeping measurements. Including uncertainties from variation between samples, temperature fluctuations and calibration, we conclude that $T_{tr} = 65.0 \pm 0.1$ °C.

5.2 Measurement of the T_c

Although we cannot measure the axial stress P_c directly, we can realize the condition $P_c = 0$ simply by breaking a nanobeam using a micromanipulator after other measurements have been completed. This produces opposing cantilevers, as illustrated in figure 5-6. If the cantilevers are prepared in the fully M1 state by warming from lower temperature to around T_c and are then brought together, the compression produces a domain of R phase in one of them. After retraction, this domain persists only above a certain temperature, and shrinks and disappears below it. We identify this temperature with T_c, the transition temperature at zero stress. By carrying out the procedure on a number of devices we obtained the striking result that in every nanobeam T_c was equal to T_{tr}, to within an uncertainty of $\delta T \approx 0.05$ °C governed by temperature fluctuations. We thus conclude that $T_c = T_{tr} = 65.0 \pm 0.1$ °C. Since the transition temperature that we found was on the lower side of the range of values in the literature, we carried out a number of checks. In the most rigorous, we constructed a separate

aluminum thermal stage, with a different sensor, in an air-tight chamber having a glass lid through which the melting and the MIT in an unstrained device could be seen. The results were all consistent with $T_{tr} = 65.0 \pm 0.1$ °C. The reproducibility of the temperature measurements is illustrated in Table 5-1, in which we show the peak positions in the histograms of the jump temperatures (as illustrated in figure 5-1) for six devices. Sample images of the same devices are also shown. The images were taken after extensive measurement runs during which in some cases (noteably P4B and P14) surface contamination had accumulated. This contamination had no discernable effect on the MIT behavior.

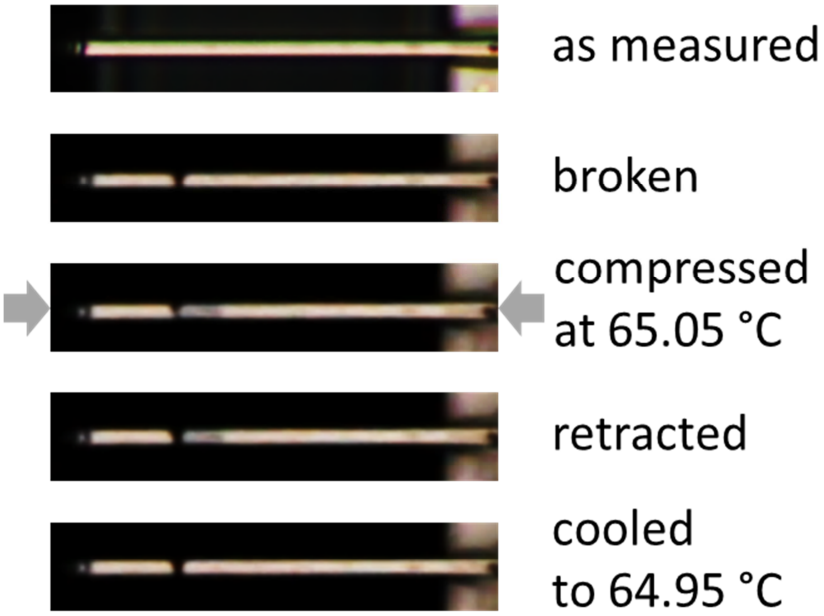

Figure 5-6 Opposing cantilevers after breaking a nanobeam. The transition temperature T_c at zero stress is measured by finding the temperature above which the metallic phase (darker) becomes stable in a cantilever, as illustrated here (device P8) It is found to be equal to the triple point temperature.

Device	$T_{R\rightarrow M1}$ (°C)	$T_{M1\rightarrow R}$ (°C)	
P4B	64.92	67.44	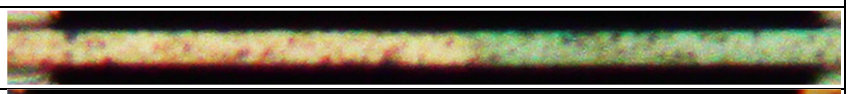
P7	65.20	65.70	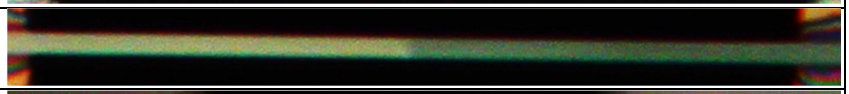
P8B	64.99	65.20	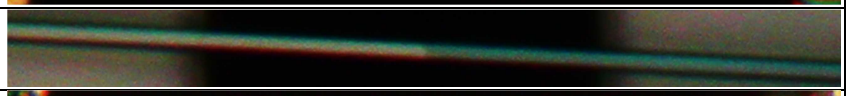
P10C	65.07	67.46	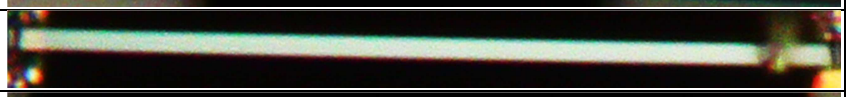
P12	64.93	65.32	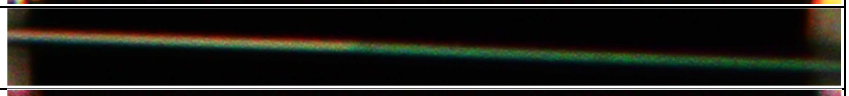
P14	64.98	65.26	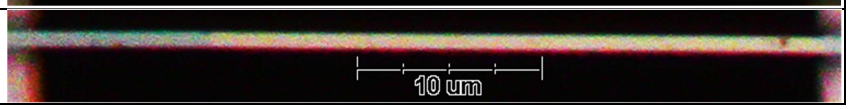

Table 5-1 Jump temperatures and images in metal-insulator coexistence of six of the devices. P8b is across a 20 μm slot; the others are across 40 μm slots.

5.3 Construction of the phase diagram

Figure 5-7 shows the phase diagram of VO_2 inferred from measurements on ten nanobeams. As discussed in section 2.6, the $P_c(T)|_{ij}$ were deduced from measurements of y_{ij} (i,j =M1,M2,R) versus T. Since the stress in coexistence must take the phase equilibrium value, consideration of the variation of the strain $\eta = P_c/E$ with T (E is the Young's modulus, taken to be 140 GPa for every phase[59]) yields[38]

$$\frac{1}{E}\frac{\partial P_c}{\partial T}\Big|_{ij} = \frac{d\eta}{dT}\Big|_{ij} = -\frac{\alpha_{ij}}{L_0}\frac{dy_{ij}}{dT} - \Delta K \qquad (1)$$

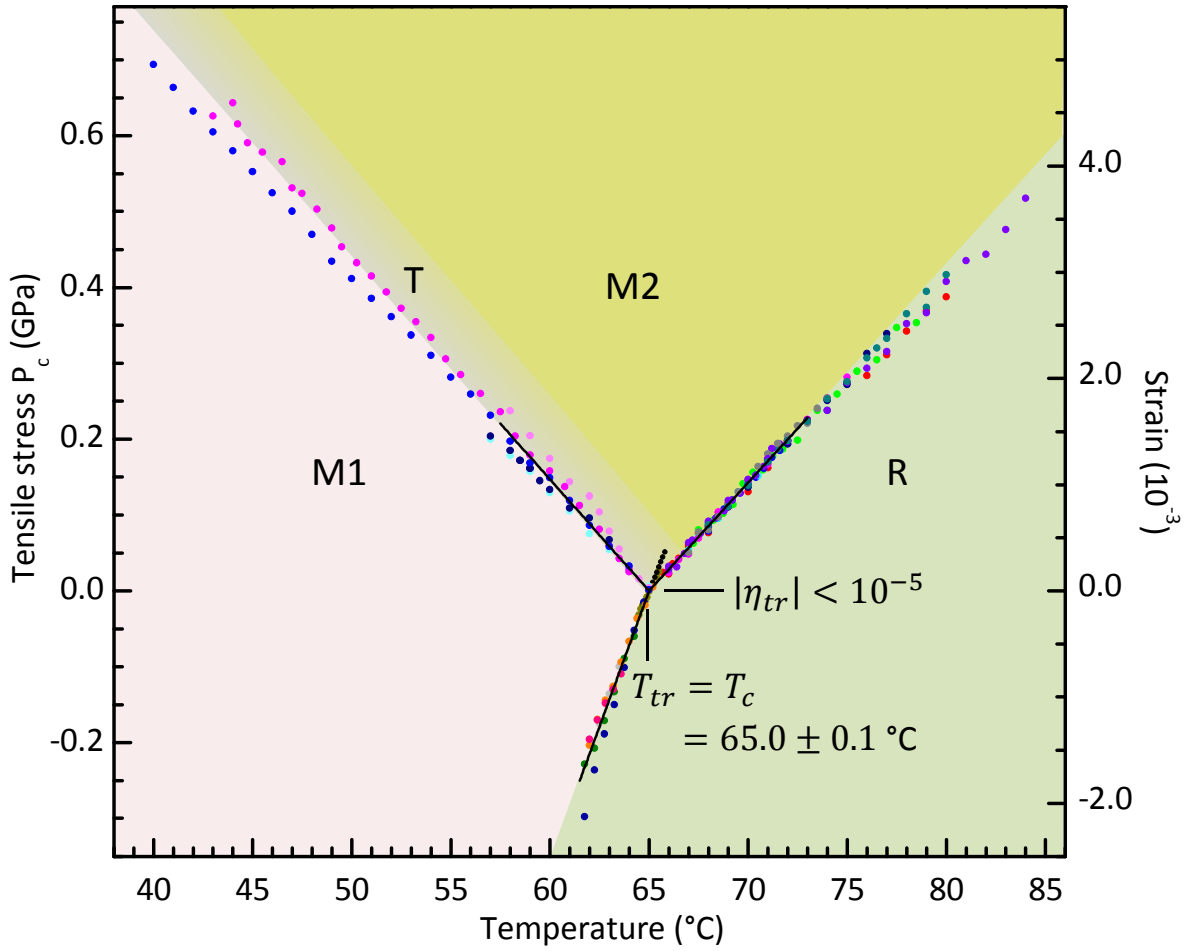

Figure 5-7 Deduced stress-temperature phase diagram. The samll black filled circles are for the superheated M1 phase. The grey shadedstrip is where a metastable T phase can occur.

The first term on the right is the change due to movement of the interface. To obtain $\eta(T)$ for each boundary from the y_{ij} measurements using Eq. 1 we first subtracted a constant from each $y_{ij}(T)$ dataset so as to set $y_{ij} = 0$ at $T_{tr} = 65.0$ °C. We then divided the results by the gap width L_0 which was close to either 20 or 40 μm (some allowance was made for a slightly different apparent clamping length). Only measurements on devices with a clear single moving

interface were used. The deduced boundary slopes at the triple point, shown by the solid straight lines in figure 5-7, were constrained to be consistent with

$$\alpha_{\mathrm{M2M1}} \left.\frac{\partial \eta}{\partial T}\right|_{M2M1} + \alpha_{M1R} \left.\frac{\partial \eta}{\partial T}\right|_{M1R} = \alpha_{M2R} \left.\frac{\partial \eta}{\partial T}\right|_{M2R} \quad (2)$$

This results from the relevant Clausius-Clapeyron relations,

$$\left.\frac{\partial P_c}{\partial T}\right|_{ij} = \frac{S_j - S_i}{b^2(a_i - a_j)} \approx \frac{S_j - S_i}{\alpha_{ij} V} \quad (3)$$

where S_i is the entropy per vanadium pair. Here $b = 4.55$ Å is the base length and $V = b^2 a_R = 59$ Å^3 is the volume of the tetragonal unit cell. Eliminating the entropies, using Eq. 1 taking ΔK and E to be constants, and using $\alpha_{\mathrm{M2R}} \approx \alpha_{\mathrm{M2M1}} + \alpha_{\mathrm{M1R}}$ gives Eq. 2. (see section 2.6) The stress P_c was then obtained by multiplying by $E = 140$ GPa. The second, $\Delta K = K_{\mathrm{VO_2}} - K_{\mathrm{Si}}$, is the thermal expansion mismatch between nanobeam and silicon substrate, which produces a correction of 5-10 %, where $K_{\mathrm{Si}} = 0.03 \times 10^{-4}$ °C^{-1}. (The slot expands with temperature along with monolithic silicon chip that it is etched in.) For the monoclinic phases[52], $K_{\mathrm{VO_2}} \approx 0.12 \times 10^{-4}$ °C^{-1} giving $\Delta K \approx 0.09 \times 10^{-4}$ °C^{-1}. For the R phase[52], $K_{\mathrm{VO_2}} \approx 0.30 \times 10^{-4}$ °C^{-1}, but we typically perform measurements with about half the nanobeam metallic, in which case $\Delta K \approx 0.2 \times 10^{-4}$ °C^{-1}. Hence ΔK gives a correction to the phase boundary slope of less than 10 %. As the interface moves and the fraction of R phase increases this correction increases and its magnitude can account for the slight downward curvature of the phase boundary measurements plotted in figure 5-7. We chose not to attempt to compensate for the effect because the thermal expansion coefficients are not known accurately and the effect is not larger than the spread in the measurements between devices. In fact, we can determine the

difference in $\mathrm{K_{VO_2}}$ between phases i and j by comparing measurements made for the nanobeam mainly in phase i with those for it mainly in phase j. For example, figure 5-8 shows measurements in M2-R coexistence on device P14 ($L_0 = 40$ μm) in which T was varied while simultaneously varying L so as to keep y_{M2R} constant, with (i) the suspended section mostly R, and (ii) with it 75% M2 (ie, with the interface close to either one contact or the other). The difference between the slopes obtained, about 0.5 nm °C^{-1}, according to Eq. 1 results solely from the difference between K_{R} and K_{M2}, and should be about $0.75L_0 \times (K_R - K_{M2})$. From this we get $(K_R - K_{M2}) \approx$ (0.5 nm °C^{-1})/(30 μm) $\approx 0.17 \times 10^{-4}$ °C^{-1}, in good agreement with the literature values given above.

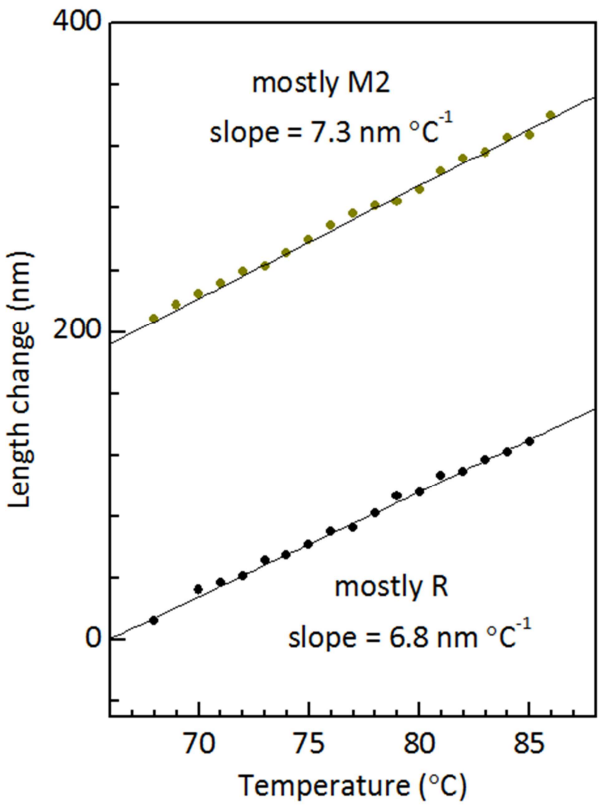

Figure 5-8 Measurements of length change needed to maintain a fixed M2-R interface position. (device P14)

The straight line fit to the M1-R phase boundary shown in figure 5-7 has slope $\partial P_c/\partial T|_{M1R} = 71$ MPa °C^{-1} which corresponds to a specific latent heat $T_c(S_R - S_{M1})/V = 1020$ cal/(mole formula unit) that is the same as measured previously[61] for the MIT in a macroscopic crystal. The deduced phase boundaries are straight, with uncertainties in their slopes of 5-10%.$\partial P_c/\partial T|_{M2R} = 29$ MPa °C^{-1} corresponds to 710 cal/mole; and $\partial P_c/\partial T|_{M2M1} = -29$ MPa °C^{-1}. From the results we deduce entropy differences $S_{\mathrm{R}} - S_{\mathrm{M1}} = (3.0 \pm 0.3)\, k_B$ and $S_{\mathrm{R}} - S_{\mathrm{M2}} = (2.1 \pm 0.1)\, k_B$. The equality of T_{tr} and T_c to within $\delta T \approx 0.05$ °C implies that the strain η_{tr} at the triple point is smaller than $\delta T \times d\eta/dT|_{\mathrm{M2R}} = 1.0 \times 10^{-5}$, where $d\eta/dT|_{\mathrm{M2R}} = 2.0 \times 10^{-4}$ °C^{-1}, and this is also indicated on the phase diagram. We believe the assumption made in Eq. 1 of a single Young's modulus for the three all phases is justified because the nature of the bonding in the material does not differ much between the phases, and because it leads to consistent results. A recent experiment[59] based on measurements of a nanobeam reported possible evidence of a difference between M1 and M2 at the 10-20% level, which would not significantly affect any of our results. Moreover, even if E were substantially different between phases it would make the equations more complicated and could alter the phase boundary slopes somewhat but would have no effect on our main conclusions. To stress the implication of these results we sketch in figure 5-9 the T dependence of the Gibbs free energies G_i of the phases of unstrained VO_2, setting $G_{\mathrm{R}} = 0$. The slopes are the entropies $S_i = -dG_i/dT$ at zero stress. Precisely at the MIT the insulating M1 and M2 phases are simultaneously degenerate with the metallic R phase. This and other facts revealed by our measurements are not explained by current models of the transition, but will be crucial ingredients of the correct theory. For example, further development and application of the

Landau theory[43] of VO_2 should be prompted by our results. The striking new insights we have gained into this important solid-state phase transition will be critical for both understanding and mastering the MIT in VO_2.

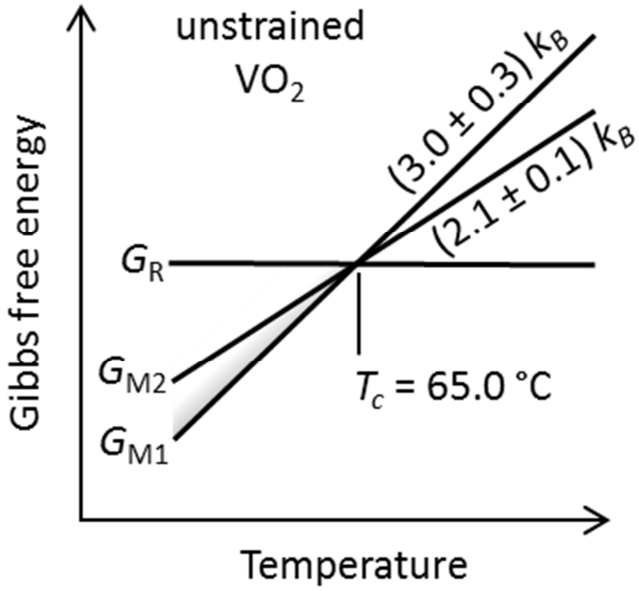

Figure 5-9 The free energies of all the phases in VO2 near T_c. The results imply that the free energies of all the phases are degenerate at T_c in unstrained pure VO_2.

Resistance versus length measurements also yield other useful information. Here we elaborate on the analysis of the measurements of resistance R_n vs length L and temperature T in figure 5-6. The electrical contacts to device P10 were made by drawing molten indium at the edges of the slot using a nanomanipulator, and there was a substantial contact resistance R_c, probably because the indium partially oxidized. R_c was determined to be $0.9\ \mathrm{M\Omega}$ from the value of the resistance when the nanobeam was in the fully metallic R state (since the resistivity of R is 10^4 times smaller than M1 or M2, $\rho_{\mathrm{R}} \approx 3 \times 10^{-4}\ \Omega$ cm) and was subtracted from R_n.

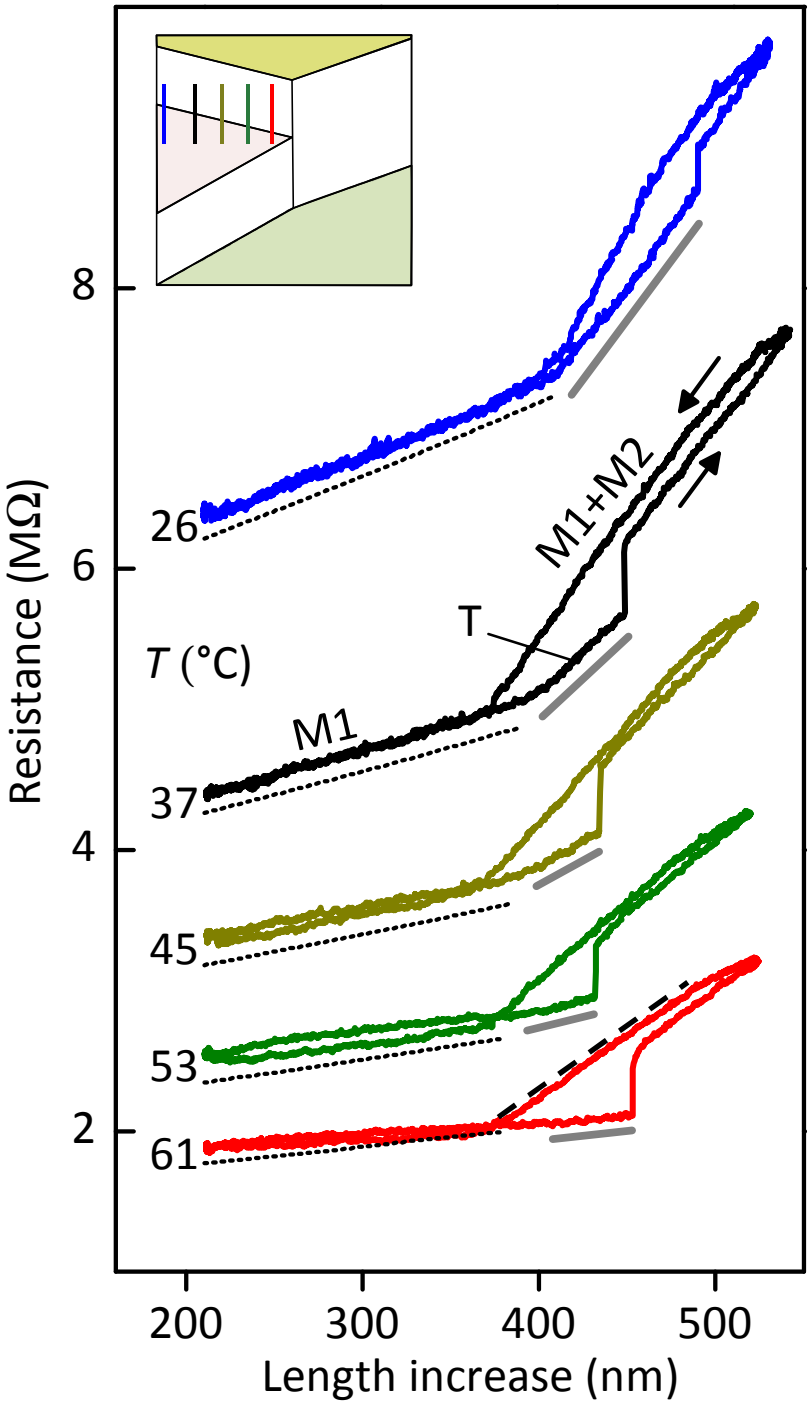

Figure 5-10 The variation of the resistance with L and T. The variation is due to a strain-dependent activation energy in the M1 phase (dotted lines, offset by $-0.15\ \mathrm{M\Omega}$ for clarity) and to conversion of M1 to M2 in coexistence (dashed line). Grey lines indicate an additional resistance rise attributed to the T phase.

First, the variation of the resistance of the M1 state with *L* and *T* is explained by a linear increase in the activation energy of the resistance with tensile strain. The conductivities of M1 and M2 are known to be activated, though their values vary somewhat in the literature. In earlier work[38] we found the resistivity of M2 to have a well defined value of $\rho_{\mathrm{M2}} \approx 12\ \Omega$cm at the MIT, and its activation energy in unstrained (buckled) nanobeams to be $\Delta_{M2} = 0.30 \pm 0.01$ eV. The variation of R_n in the M1 state in figure 5-6 is consistent with a linear variation of the activation energy with strain, i.e.:

$$R_n = R_{\mathrm{M1}} = R_0 \exp(\Delta_{\mathrm{M1}}/kT)\ ,$$

with

$$\Delta_{\mathrm{M1}} = \Delta_0 + \gamma\eta\ .$$

Here $\eta = (L - L_0)/L_0$, where L_0 is the natural effective clamped length, and Δ_0 is the gap at $\eta = 0$. We determine the slot width *L* at $\eta = 0$ using our knowledge that the triple point is at zero strain (it is at length increase ≈ 300 nm in figure 5-6). We obtain the best fit to the entire dataset, shown by the dotted lines in figure 5-6 (which are offset by -0.15 MΩ for clarity), with parameter values $\Delta_0 = 0.31$ eV, $\gamma = 0.77$ eV, and $R_0 = 40.5$ MΩ. The uncertainty is about 0.01 eV in Δ_0 and 10% in γ. From optical images we roughly estimate the cross-sectional area of the nanobeam as $A \approx 1\ \mu\mathrm{m}^2$, putting $\rho_{M1} = R_n A/L_0$ in the ballpark of (2 MΩ)(1 μm^2)/(40 μm) ~ 5 Ωcm.

Second, from the variation of R_n in M1+M2 coexistence (such as indicated by the dashed line) we can deduce that $\rho_{M2}/\rho_{M1} = 2.3 \pm 0.2$ and that the activation energies of M1 and M2 are the same to within a few percent. The variation of R_n in the M1+M2 state in figure

5-10 is due to the change in the interface position y_{M2M1} from 0 to L_0 as the nanobeam gradually converts from M1 to M2. We can deduce the ratio of their resistivities using

$$R_n = R_{\mathrm{M1}} + (R_{\mathrm{M2}} - R_{\mathrm{M1}})\frac{y_{\mathrm{M2M1}}}{L_0},$$

from which we have

$$\frac{1}{R_{M1}}\frac{dR_n}{dL} = \left(\frac{R_{M2}}{R_{M1}} - 1\right)\frac{1}{L_0}\frac{dy_{\mathrm{M2M1}}}{dL} = \left(\frac{\rho_{\mathrm{M2}}}{\rho_{\mathrm{M1}}} - 1\right)\frac{1}{L_0}\frac{1}{\alpha_{\mathrm{M2M1}}}$$

and thus

$$\frac{\rho_{\mathrm{M2}}}{\rho_{\mathrm{M1}}} = 1 + \frac{\alpha_{\mathrm{M2M1}}L_0}{R_{\mathrm{M1}}}\frac{dR_n}{dL}.$$

For example, using the data at 61 °C we have $\frac{dR_n}{dL} = 8.6$ MΩ/μm (the slope of the dashed line in figure 5-10), $R_{M1} = 2.0$ MΩ (taken from R_n at the foot of the dashed line where $y_{\mathrm{M2M1}} = 0$), $\alpha_{\mathrm{M2M1}} = 0.0074$, and $L_0 = 40$ μm, which gives $\rho_{\mathrm{M2}}/\rho_{\mathrm{M1}} = 2.3$ with about 10% uncertainty. This ratio has not been determined accurately before. This again gives $\rho_{\mathrm{M1}} =$ (12 Ωcm)/2.3 ≈ 5 Ωcm. In addition, we find that $\rho_{\mathrm{M2}}/\rho_{\mathrm{M1}}$ does not change by more than 5% between 26 and 64 °C, implying that the activation energies are equal, $\Delta_{\mathrm{M2}} = \Delta_{\mathrm{M1}}$, to within a few percent.

Third, a distinct additional rise in R_n, indicated by the solid gray lines, precedes the nucleation of M2 from M1. This can be explained by a continuous distortion of M1 into the T phase, which we immediately infer has a higher resistivity than M1 and is unstable relative to M2 at all temperatures from T_{tr} to below 26 °C. Finally, the finding that the T phase is metastable with respect to M2 is indicated by a gray shaded strip within the M2 stability region.

6 Conclusion

A unique, novel experimental approach to controlling the length of a suspended nanostructure is presented. A simple and compact design of the setup allows simultaneous transport and optical measurements under a microscope while actively controlling both the temperature and the length of the nanobeam, in this case a crystal of VO_2, with the precision of ±0.05 °C and ~1 nm respectively. Using this approach, the first accurate measurement of a triple point in VO_2 is made and the intrinsic phase stability diagram is constructed.

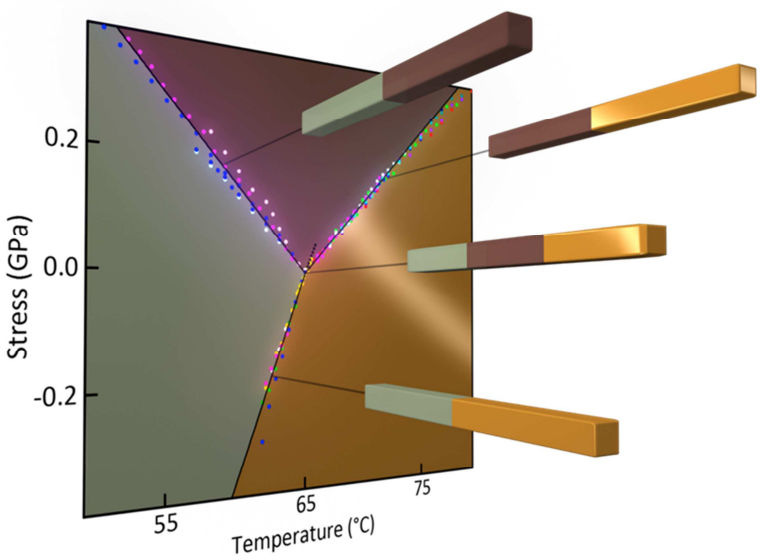

Figure 6-1 Phase diagram of VO_2. (Illustration courtesy of Serkan Kasirga)

Appendix A: Earlier Versions of the strain device

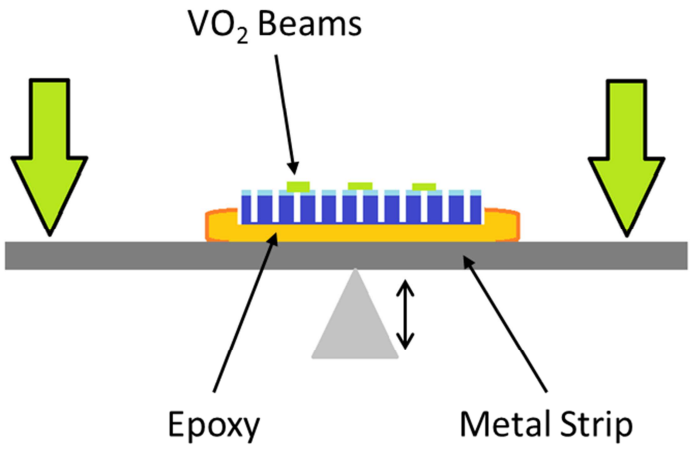

Figure A-1 Schematic of three point bending method.

One of the most common ways to induce stress is to use three-point bending setup as in figure A-1. In many cases, a plastic or soft substrate is used that can either be stretched or bent. At the budding stage of this project before the technology of transferring VO_2 was developed, a soft substrate was out of question since it was not compatible with a high temperature growth process. Also as mentioned in chapter 4, there are many advantages of working with silicon wafers. In order to achieve this, silicon chips with deep trenches were designed and fabricated. Starting with a standard 4-inch 500-550 µm thick Si wafer, an array of 20 µm wide strips was patterned and etched. The cross-sectional view of the wafer is as shown on the figure A-2. After the chips were fabricated, the VO_2 nanobeams could be grown across a slit as shown on figure A-3. The chance of growing a nanobeam across the slit was low so a large number of trenches were prepared. The photolithography was done at the UW Nanofabrication Facility (formerly

UW Nanotechnology Center) and dry etched at the UCSB Nanofabrication Facility. (Ning Cao) One clear advantage of this method was its simplicity of fabrication.

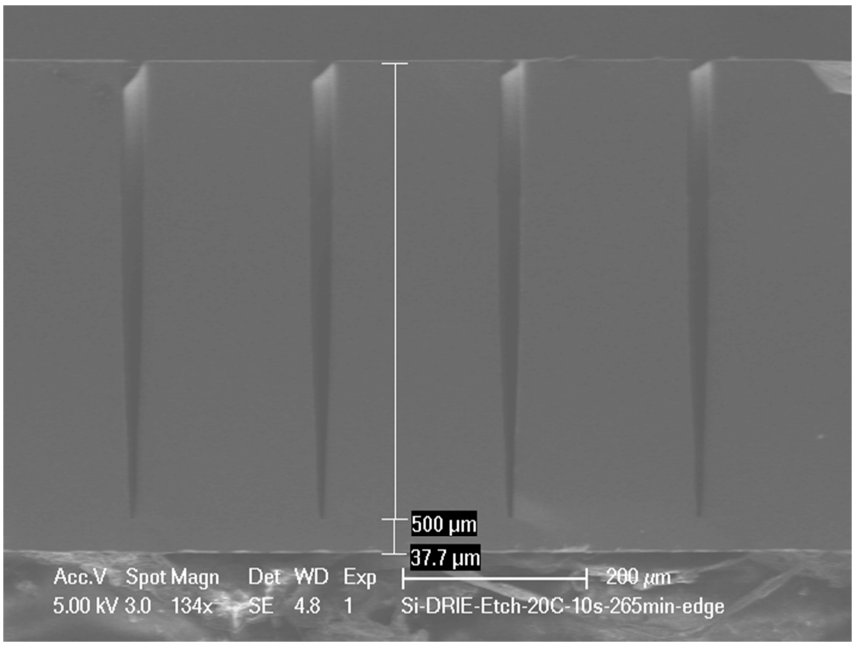

Figure A-2 SEM image of the wafer cross-section showing trenches. 20 µm wide and 500 µm deep trenches were prepared by a single run of DRIE. By bending the wafer slightly, the gap width can be controlled.

Several difficulties prevented further development of this method: i) The chips fabricated in this method were extremely fragile, even more so than the paddles. ii) It was not clear under what load the chip would break. With a paddle chip, it could bend only so much and it was possible to visually inspect the macroscopic bending. But these chips with trenches showed no sign of the point at which they break. (of course, this would be why one would use soft substrates) iii) Widening the gap can be easily achieved by pushing from the bottom of the chip. But it was not straightforward how to close the gap. The implementation of this seemed more difficult than the paddle chip design. iv) Though this may be small effect, the nanobeam

would shift away from the optical focal plane as the wafer bends from the applied stress. v) The change in gap width would have been inferred from using geometry and fitting rather than a direct measurement. For these reasons and some more, three point bending approach was abandoned in favor of the Si paddle chip design, which bends in-plane.

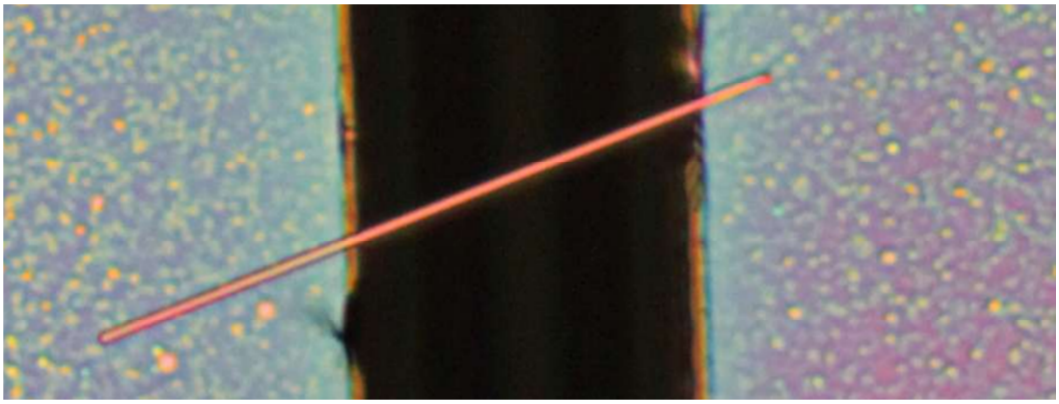

Figure A-3 VO_2 nanobeam grown across a 20 µm trench. As mentioned in section 4.4, the orientation of a nanobeam across slit is uncontrollable. The yield is too low to be practical for device fabrication.

At the budding stage of the project, there was a brief collaboration with Zenghui Wang at Cornell, who was developing an approach, quite more difficult and advanced, to applying controlled strain on a graphene. He fabricated state-of-art silicon-on-insulator (SOI) chips with comb drives that utilize electrostatic forces to actuate. The working principle is simple. When applying a voltage bias V between two spatially separated sets of combs, see figure A-4, the total energy of the system can be written as $E = \frac{1}{2}CV^2$, where C represents the capacitance between the two sets of combs. Assuming a parallel plate capacitance, C is simply proportional to Δx, which is the overlap length of the comb fingers. Following through the calculation for the force,

$$\frac{\partial E}{\partial \Delta x} = F_{\Delta x} = \frac{1}{2}\frac{nt\epsilon_o\epsilon_r V^2}{d}$$

where F is the force applied in the direction of shuttle motion, V is the applied electric potential, n is the number of pairs of comb fingers, t is the thickness in the out of plane direction of the comb fingers, d is the gap between comb fingers, ϵ_o is the permittivity of free space, and ϵ_r is the relative permittivity of the dielectric.

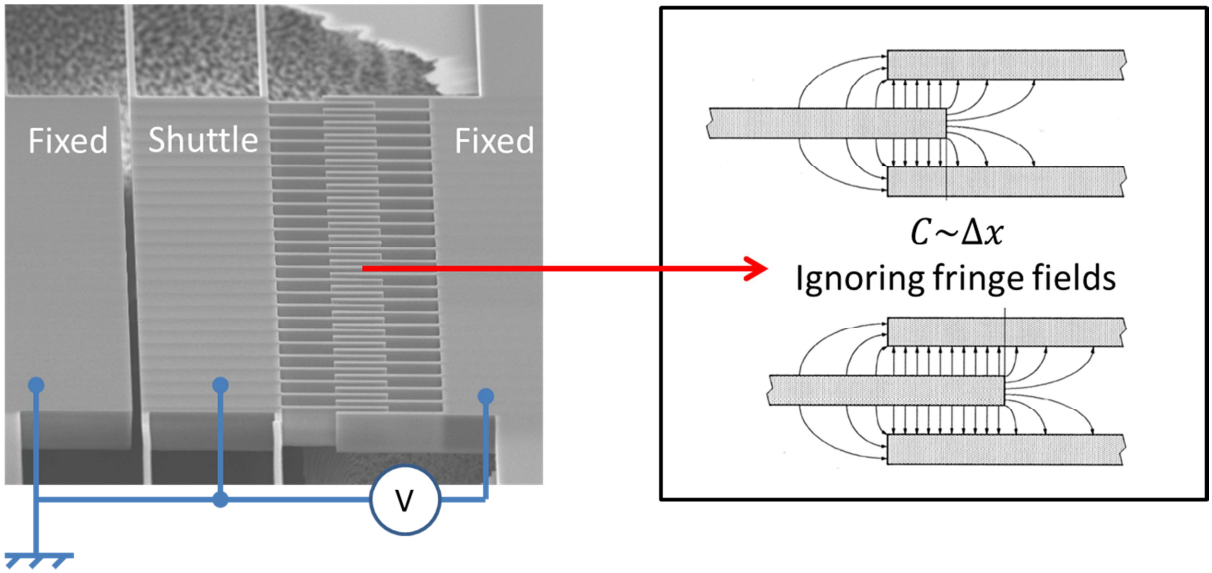

Figure A-4 Comb drive working principle. An applied bias as shown would shift the shuttle toward the right due to an electrostatic force, applying tension on a nanobeam if it were suspended over the left slit.

The main problem with this approach is that it is not ideal for applying a large force. The magnitude of applicable force is limited by the dielectric breakdown voltage, which is quite low in air. (~ 3 V/μm) In other words, you can apply up to about 6 V in air with $t = 10$ μm and $d = 2$ μm. At a moderate voltage, the force equates to 88.5 pN/n at 2 V. The uniaxial pressure required to stretch a VO_2 nanobeam by one percent is $E\eta = (140\text{ GPa})(0.01) = 1.4\text{ GPa}$. For a

nanobeam with a cross-section of about $1\ \mu m^2$, that translates to 1.4 mN. The device needs about 10^7 comb fingers to function properly give or take an order of magnitude. Though application of stress to induce a phase transition was not a viable option, we went ahead and tested whether such a device could be interfaced with a separated piezo-controlled pusher to actuate the shuttle. Figure A-5 shows this attempt.

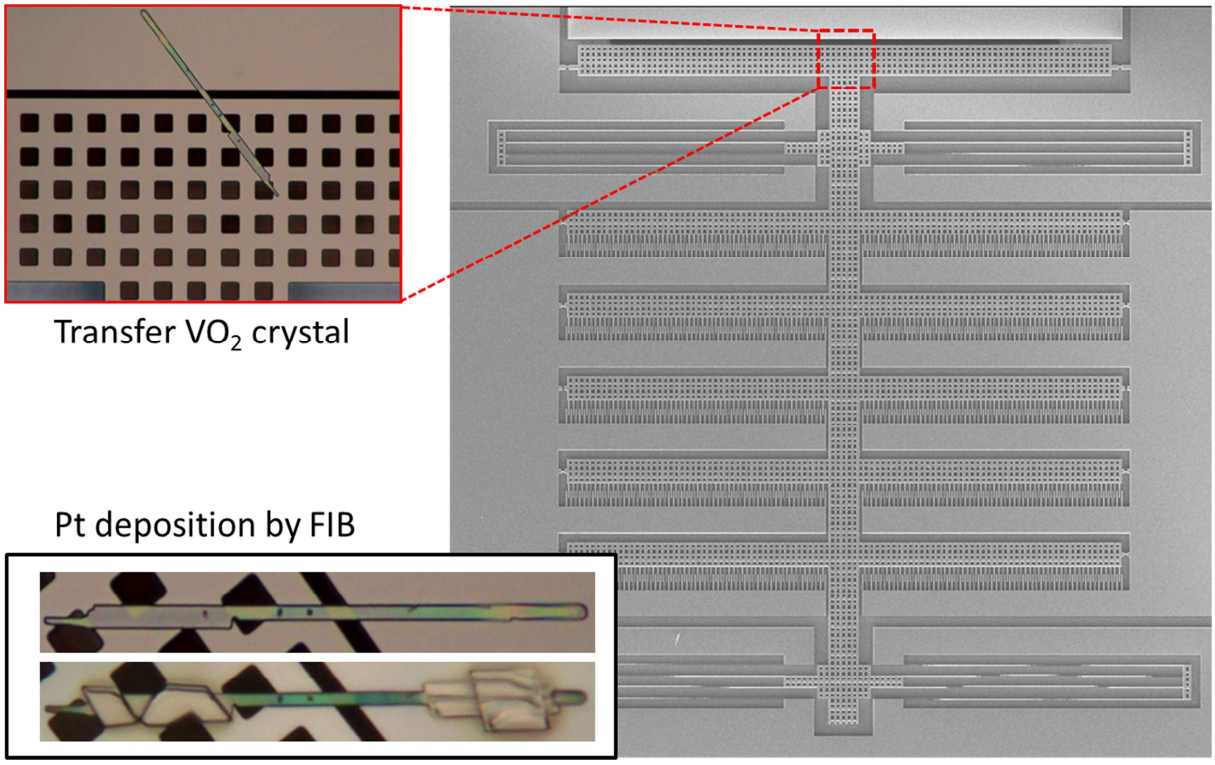

Figure A-5 Comb drive device. A VO_2 nanobeam is transferred onto a device chip and clamped by Pt deposition using a FIB. Coexistence was observed and some actuation was done by pushing the shuttle with a needle mounted on a nanomanipulator.

Besides the obvious problems, this approach was costly in terms of fabrication expense, labor, logistics, and process development. Comb drives are also quite fragile and above all, they

are very intricate devices, requiring nearly flawless execution at every step along the fabrication procedure. So again, the paddle chip design was chosen.

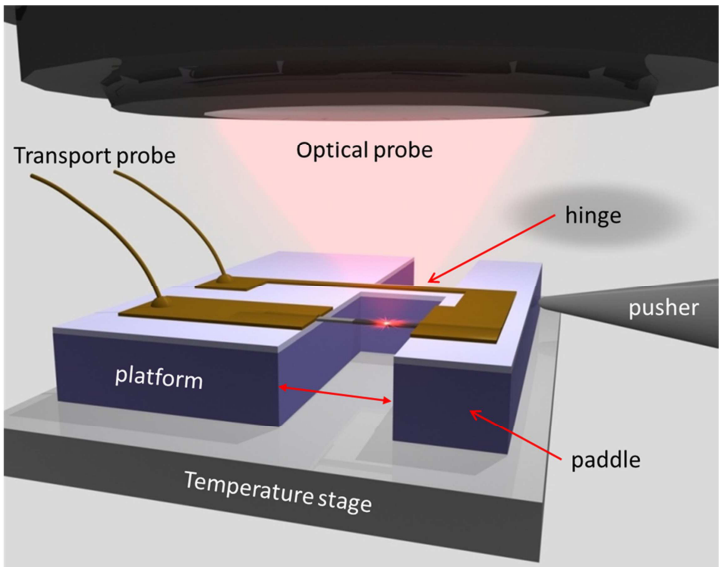

Figure A-6 Concept art of the strain apparatus. (Illustration courtesy of Serkan Kasirga)

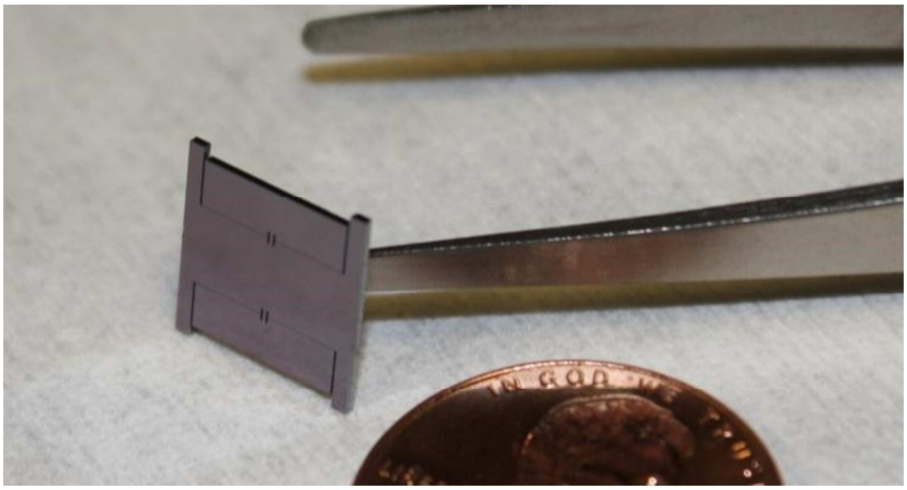

Figure A-7 An earlier version of the paddle chip. Two paddles per chip were patterned to provide more slits to suspend nanobeams at first. The chip design was updated to allow for larger metal contacts.

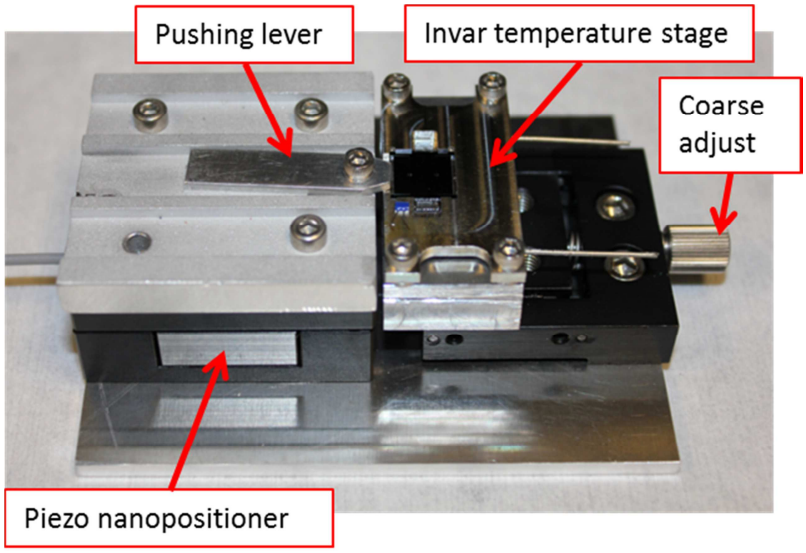

Figure A-8 Earlier version of the strain apparatus. ("pre-laser setup") Initially the position of closed-loop piezo was thought to be sufficient for characterizing the gap width by using geometry, simulation, and some fitting parameters. No serious measurement, however, could be performed.

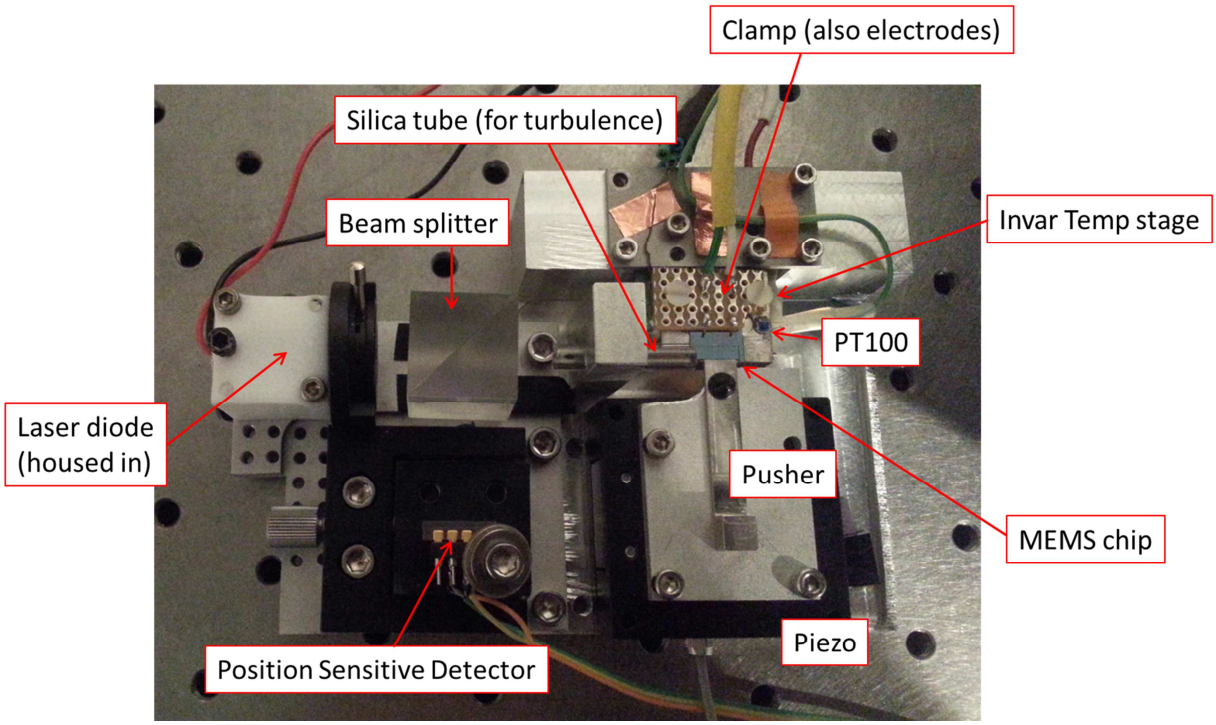

Figure A-9 Strain apparatus. There is another PT100 sensor (not shown) embedded inside the invar temperature stage. This was always supposed to be a prototype before putting together a 'serious' one. But it worked well.

Appendix B: Fabrication Procedure

4-inch Si wafers, 500 µm thick, double-side polished, 2 µm thermal oxide

Photolithography Procedure

1) Wafer clean: soaked in acetone (2 min) and methanol (1 min) in ultrasonic bath; DI rinse and N_2 gun blow-dry.

2) Wafer's front-side dehydration at 115 °C for 5 min.

3) Applying HMDS: dropping HMDS onto wafer's front-side, waiting for 30 s, and spinning at 3000 RPM for 30 s.

4) Applying PR: dropping SPR220-3 onto wafer's front-side, and spinning at 3000 RPM for 30 s.

5) PR soft bake at 115 °C for 90 s.

6) PR exposure with the front-side-pattern mask and an exposure dose of 430 mJ/cm^2 using Karl-Suss MA-BA-6 Mask/bond Aligner with backside optics.

7) Post-exposure-bake at 115 °C for 90 s.

8) Pattern development in AZ-726MIF for 70 s.

9) O_2 plasma descum at 300 mT / 100 W for 45 s.

10) Pattern transfer into the SiO_2 layer (2 µm) using Panasonic ICP etcher (Model: E640) with the parameters of 0.5Pa, 200/900 W, CHF_3 flow-rate=40 sccm, and etch time=9 min.

11) Removing the remaining PR: soaked in PRX-127 Striper for 30 min+10 min (a fresh one) on an 80 °C hot plate; soaked in acetone (5 min)+methanol(1 min) in ultrasonic bath; DI rinse and N_2 gun blow-dry.

12) O_2 plasma descum at 300 mT/200 W for 2 min.

13) Wafer's back-side dehydration at 115 C for 2 min.

14) Applying HMDS: dropping HMDS onto wafer's back-side, waiting for 30 s, and spinning at 3500 RPM for 30 s.

15) Applying PR: dropping SPR220-7 onto wafer's back-side, and spinning at 3500 RPM for 30 s.

16) PR soft bake at 115 °C for 2 min.

17) PR exposure with the back-side-pattern mask and an exposure dose of 585 mJ/cm^2 using Karl-Suss MA-BA-6 Mask/bond Aligner with backside optics (aligning the front-side pattern to the back-side-pattern mask).

18) Waiting for 5 min.

19) Pattern development in AZ-726MIF for 80 s.

20) O2 plasma descum at 300 mT/100W for 60 s.

21) Pattern transfer into the SiO_2 layer (2 µm) using Panasonic ICP etcher (Model: E640) with the parameters of 0.5 Pa, 200/900 W, CHF3 flow-rate=40 sccm, and etch time=9 min.

22) Removing the PR on the edge of the wafer using acetone-soaked Q-tips.

23) Wafer's back-side deep Si etch at 20 °C using Plasma- therm SLR SiRIE Etcher and the modified Bosch process (see the process detail below) for 220 min.

24) Removing the remaining PR: soaked in PRX-127 Striper for 30 min+10 min (a fresh one) on an 80 °C hot plate; soaked in acetone (5 min)+isopropanol(1 min) in ultrasonic bath; N^2 gun blow-dry.

25) O_2 plasma descum at 300 mT/200W for 2 min.

26) Mounting the wafer onto a 4" Si sacrificial wafer using the pump oil.

27) Wafer's front-side deep Si etch at 20 °C using Plasma- therm SLR SiRIE Etcher and the modified Bosch process for 30 min.

The modified Bosch process:

1) Deposition step: 23 mT, 0.1/825W, C_4F_8/SF_6/Ar flow-rate=70/0.5/40 sccm, and step time=5 s;

2) Etch step A: 23 mT, 9/825W, C_4F_8/SF_6/Ar flow-rate=0.5/50/40 sccm, and step time=2 s;

3) Etch step B: 23 mT, 9/825W, C_4F_8/SF_6/Ar flow-rate=0.5/100/40 sccm, and step time=10 s.

References

1. Anderson, P. W. More Is Different. *Science (80-.).* **177,** 393–396 (1972).

2. Novoselov, K. S. *et al.* Two-dimensional gas of massless Dirac fermions in graphene. *Nature* **438,** 197–200 (2005).

3. Mourik, V. *et al.* Signatures of Majorana fermions in hybrid superconductor-semiconductor nanowire devices. *Science* **336,** 1003–7 (2012).

4. Endres, M. *et al.* The “Higgs” amplitude mode at the two-dimensional superfluid/Mott insulator transition. *Nature* **487,** 454–8 (2012).

5. Lee, P. a. & Wen, X.-G. Doping a Mott insulator: Physics of high-temperature superconductivity. *Rev. Mod. Phys.* **78,** 17–85 (2006).

6. Imada, M., Fujimori, A. & Tokura, Y. Metal-insulator transitions. *Rev. Mod. Phys.* **70,** 1039–1263 (1998).

7. Stewart, G. R. Heavy-fermion systems. *Rev. Mod. Phys.* **56,** 755–787 (1984).

8. Sachdev, S. Quantum Criticality: Competing Ground States in Low Dimensions. *Science (80-.).* **288,** 475–480 (2000).

9. Morin, F. J. Oxides which show a Metal-to-Insulator Transition at the Neel Temperature. *Phys. Rev. Lett.* **3,** 34–36 (1959).

10. Guiton, B. S., Gu, Q., Prieto, A. L., Gudiksen, M. S. & Park, H. Single-crystalline vanadium dioxide nanowires with rectangular cross sections. *J. Am. Chem. Soc.* **127,** 498–9 (2005).

11. Ladd, L. A. & Paul, W. OPTICAL AND TRANSPORT PROPERTIES OF HIGH QUALITY CRYSTALS OF V_20_4 NEAR THE METALLIC TRANSITIONTEMPERATURE. *Solid State Commun.* **7,** 425–428 (1969).

12. Verleur, H. W., Barker, JR., A. S. & Berglund, C. N. Optical Properties of VO_2 between 0.25 and 5 eV. *Phys. Rev.* **172,** 788–798 (1968).

13. Qazilbash, M. *et al.* Correlated metallic state of vanadium dioxide. *Phys. Rev. B* **74,** 1–5 (2006).

14. Zhou, Y. *et al.* Voltage-Triggered Ultrafast Phase Transition in Vanadium Dioxide Switches. *IEEE Electron Device Lett.* **34,** 220–222 (2013).

15. Strelcov, E., Lilach, Y. & Kolmakov, A. Gas Sensor Based on Metal-Insulator Transition in VO_2 Nanowire Thermistor 2009. *Nano Lett.* **9,** 2322–2326 (2009).

16. Becker, M. F., Buckman, A. B., Walser, R. M., Georges, P. & Brun, A. Femtosecond laser excitation dynamics of the semiconductor-metal phase transition in VO_2. **79,** (1996).

17. Hilton, D. *et al.* Enhanced Photosusceptibility near Tc for the Light-Induced Insulator-to-Metal Phase Transition in Vanadium Dioxide. *Phys. Rev. Lett.* **99,** 226401 (2007).

18. Kübler, C. *et al.* Coherent Structural Dynamics and Electronic Correlations during an Ultrafast Insulator-to-Metal Phase Transition in VO_2. *Phys. Rev. Lett.* **99,** 1–4 (2007).

19. Qazilbash, M. *et al.* Mott Transition in VO_2 Revealed by Infrared Spectroscopy and Nano-Imaging. *Science (80-.).* **318,** 1750–1753 (2007).

20. Jones, A. C., Berweger, S., Wei, J., Cobden, D. & Raschke, M. B. Nano-optical investigations of the metal-insulator phase behavior of individual VO_2 microcrystals. *Nano Lett.* **10,** 1574–81 (2010).

21. Nakano, M. *et al.* Collective bulk carrier delocalization driven by electrostatic surface charge accumulation. *Nature* **487,** 459–462 (2012).

22. Biermann, S., Poteryaev, a., Lichtenstein, a. & Georges, a. Dynamical Singlets and Correlation-Assisted Peierls Transition in VO_2. *Phys. Rev. Lett.* **94,** 026404 (2005).

23. Eyert, V. VO_2: A Novel View from Band Theory. *Phys. Rev. Lett.* **107,** 016401 (2011).

24. Jeong, J. *et al.* Suppression of Metal-Insulator Transition in VO_2 by Electric Field-Induced Oxygen Vacancy Formation. *Science (80-.).* **339,** 1402–1405 (2013).

25. Wei, J., Ji, H., Guo, W., Nevidomskyy, A. H. & Natelson, D. Hydrogen stabilization of metallic vanadium dioxide in single-crystal nanobeams. *Nat. Nanotechnol.* **7,** 357–62 (2012).

26. Paul, W. THE PRESENT POSITION OF THEORY AND EXPERIMENT FOR VO_2. *Mat. Res. Bull.* **5,** 691–702 (1970).

27. Hearn, C. J. Phonon softening and the metal-insulator transition in VO_2. *J. Appl. Phys.* **5,** 1317–1334 (1972).

28. Zylbersztejn, A. & Mott, N. F. Metal-insulator transition in vanadium dioxide. *Phys. Rev. B* **11,** 4383–4395 (1975).

29. Eyert, V. The metal-insulator transitions of VO_2 : A band theoretical approach. *Ann. Phys.* **11,** 650–702 (2002).

30. M., H. J. & L., V. Z. L. THE METAL-INSULATOR TRANSITION IN SELECTED OXIDES. *Annu. Rev. Mater. Sci.* **8574,** 225–280 (1975).

31. Andersson, G. Studies on Vanadium Oxides. *Acta Chem. Scand.* **8,** 1599–1606 (1954).

32. Macchesney, J. B. & Guggenheim, H. J. GROWTH AND ELECTRICAL PROPERTIES OF VANADIUM DIOXIDE SINGLE CRYSTALS CONTAINING SELECTED IMPURITY IONS. *J. Phys. Chem. Solids* **30,** 225–234 (1969).

33. Villeneuve, G., Bordet, A., Casalot, A. & Hagenmuller, P. Physical properties and structural phase of $Cr_xV_{1-x}O_2$. *Mat. Res. Bull.* **6,** 119–130 (1971).

34. Marezio, M., McWhan, D. B., Remeika, J. P. & Dernier, P. D. Structural Aspects of the Metal-Insulator Transitions in Cr-Doped VO_2. *Phys. Rev. B* **5,** 2541–2551 (1972).

35. Villeneuve, G., Drillon, M. & Hagenmuller, P. Structural Study of $V_{1-x}Cr_xO_2$ Phases. *Mat. Res. Bull.* **8,** 1111–1122 (1973).

36. Pouget, J. P., Launois, H., D'Haenens, J. P., Merenda, P. & Rice, T. M. Electron Localization Induced by Uniaxial Stress in Pure VO_2. *Phys. Rev. Lett.* **35,** 873–875 (1975).

37. Cao, J. *et al.* Extended Mapping and Exploration of the Diagram. *Nano Lett.* **10,** 2667–2673 (2010).

38. Wei, J., Wang, Z., Chen, W. & Cobden, D. H. New aspects of the metal – insulator transition in single-domain vanadium dioxide nanobeams. *Nat. Nanotechnol.* **4,** (2009).

39. Goodenough, J. B. The Two Components of the Crystallographic Transition in VO_2. *J. Solid State Chem.* **3,** 490–500 (1971).

40. Rice, T. M., Launois, H. & Pouget, J. P. Comment on "VO_2: Peierls or Mott-Hubbard? A View from Band Theory."*Phys. Rev. Lett.* **73,** 3042 (1994).

41. Sohn, J. I. *et al.* Surface-stress-induced Mott transition and nature of associated spatial phase transition in single crystalline VO_2 nanowires. *Nano Lett.* **9,** 3392–7 (2009).

42. Zhang, S., Chou, J. Y. & Lauhon, L. J. Direct correlation of structural domain formation with the metal insulator transition in a VO_2 nanobeam. *Nano Lett.* **9,** 4527–32 (2009).

43. Tselev, a *et al.* Symmetry relationship and strain-induced transitions between insulating M1 and M2 and metallic R phases of vanadium dioxide. *Nano Lett.* **10,** 4409–16 (2010).

44. Mott, N. F. The Basis of the Electron Theory of Metals, with Special Reference to the Transition Metals. *Proc. Phys. Soc. A* **62,** 416–422 (1949).

45. Wentzcovitch, R. M., Schulz, W. W. & Allen, P. B. VO_2: Peierls or Mott-Hubbard? A View from Band Theory. *Phys. Rev. Lett.* **72,** 3389–3392 (1994).

46. Haverkort, M. W. *et al.* Orbital-Assisted Metal-Insulator Transition in VO_2. *Phys. Rev. Lett.* **95,** 196404 (2005).

47. Weber, C. *et al.* Vanadium Dioxide: A Peierls-Mott Insulator Stable against Disorder. *Phys. Rev. Lett.* **108,** 256402 (2012).

48. Kim, S., Kim, K., Kang, C.-J. & Min, B. I. Correlation-assisted phonon softening and the orbital-selective Peierls transition in VO_2. *Phys. Rev. B* **87,** 195106 (2013).

49. Tselev, A. *et al.* Interplay between ferroelastic and metal-insulator phase transitions in strained quasi-two-dimensional VO_2 nanoplatelets. *Nano Lett.* **10,** 2003–11 (2010).

50. Fillingham, P. J. Domain Structure and Twinning in Crystals of Vanadium Dioxide. *J. Appl. Phys.* **38,** 4823 (1967).

51. Blaauw, C., Leenhouts, F., Woude, F. van der & Sawatzky, G. A. The metal-non-metal transition in VO_2 : x-ray photoemission and resistivity measurements. *J. Phys. C Solid State Phys.* **8,** 459–468 (1975).

52. Kucharczyk, D. & Niklewski, T. Accurate X-ray Determination of the Lattice Parameters and the Thermal Expansion Coefficients of VO_2 near the Transition Temperature Institute for Low Temperature and Structure Research , Polish Academy of Sciences , 50-950 Wroctaw , Poland. *J. Appl. Cryst.* **12,** 370–373 (1979).

53. Allen, B., Renata, M., Schulz, W. W. & Canfield, P. C. Resistivity of the high-temperature metallic phase of VO_2. *Phys. Rev. B* **48,** 4359–4363 (1993).

54. Tselev, A. *et al.* Mesoscopic metal-insulator transition at ferroelastic domain walls in VO_2. *ACS Nano* **4,** 4412–9 (2010).

55. Wu, J. *et al.* Strain-Induced Self Organization of Metal − Insulator Domains in Single-Crystalline VO_2 Nanobeams. *Nano Lett.* **6,** 2313–2317 (2006).

56. Cao, J. *et al.* Constant threshold resistivity in the metal-insulator transition of VO_2. *Phys. Rev. B* **82,** 1–4 (2010).

57. Cao, J. *et al.* Strain engineering and one-dimensional organization of metal-insulator domains in single-crystal vanadium dioxide beams. *Nat. Nanotechnol.* **4,** 732–7 (2009).

58. Fan, W. *et al.* Superelastic metal-insulator phase transition in single-crystal VO_2 nanobeams. *Phys. Rev. B* **80,** 241105 (2009).

59. Guo, H. *et al.* Mechanics and dynamics of the strain-induced M1-M2 structural phase transition in individual VO_2 nanowires. *Nano Lett.* **11,** 3207–13 (2011).

60. Strelcov, E., Davydov, A. V, Lanke, U., Watts, C. & Kolmakov, A. In situ monitoring of the growth, intermediate phase transformations and templating of single crystal VO_2 nanowires and nanoplatelets. *ACS Nano* **5,** 3373–84 (2011).

61. Berglund, C. N. & Guggenheim, H. J. Electronic Properties of VO_2 near the Semiconductor-Metal Transition. *Phys. Rev.* **185,** 1022–1033 (1969).

62. Guntersdorfer, M. The Conductivity Anomaly in VO_2. *Solid State Electron.* **13,** 355–367 (1970).

63. Tsai, K.-Y., Chin, T.-S. & Shieh, H.-P. D. Effect of Grain Curvature on Nano-Indentation Measurements of Thin Films. *Jpn. J. Appl. Phys.* **43,** 6268–6273 (2004).

64. Sepúlveda, N., Rúa, A., Cabrera, R. & Fernández, F. Young's modulus of VO_2 thin films as a function of temperature including insulator-to-metal transition regime. *Appl. Phys. Lett.* **92,** 191913 (2008).

65. Rúa, A. *et al.* Phase transition behavior in microcantilevers coated with M1-phase VO_2 and M2-phase VO2:Cr thin films. *J. Appl. Phys.* **111,** 104502 (2012).

66. Bongers, P. F. Anisotropy of the Electrical Conductivity of VO_2 Single Crystals. *Solid State Commun.* **3,** 275–277 (1965).

67. Rao, K. V., Naidu, S. V. & Iyengar, L. Thermal Expansion of Tetragonal Phase of VO_2. *J. PH* **23,** (1967).

68. McWhan, D. B., Marezio, M., Remeika, J. P. & Dernier, P. D. X-ray diffraction study of metallic VO_2. *Phys. Rev. B* **10,** 490–495 (1974).

69. Atkin, J. *et al.* Strain and temperature dependence of the insulating phases of VO_2 near the metal-insulator transition. *Phys. Rev. B* **85,** 3–6 (2012).

70. Cox, P. A. *Transition Metal Oxides*. (Oxford, 1992).

71. Schwingenschlögl, U. & Eyert, V. The vanadium Magnéli phases V_nO_{2n-1}. *Ann. Phys.* **13,** 475–510 (2004).

72. Kasırga, T. S. *et al.* Photoresponse of a strongly correlated material determined by scanning photocurrent microscopy. *Nat. Nanotechnol.* **7,** 723–7 (2012).

73. Sahana, M. B., Subbanna, G. N. & Shivashankar, S. a. Phase transformation and semiconductor-metal transition in thin films of VO_2 deposited by low-pressure metalorganic chemical vapor deposition. *J. Appl. Phys.* **92,** 6495 (2002).

74. Partlow, D. P., Gurkovich, S. R., Radford, K. C. & Denes, L. J. Switchable vanadium oxide films by a sol-gel process. *J. Appl. Phys.* **70,** 443 (1991).

75. Chae, B.-G. *et al.* Highly Oriented VO_2 Thin Films Prepared by Sol-Gel Deposition. *Electrochem. Solid-State Lett.* **9,** C12 (2006).

76. Kim, D. H. & Kwok, H. S. Pulsed laser deposition of VO_2 thin films. **3188,** 2–5 (1994).

77. Ji, S., Zhao, Y., Zhang, F. & Jin, P. Direct formation of single crystal VO_2(R) nanorods by one-step hydrothermal treatment. *J. Cryst. Growth* **312,** 282–286 (2010).

78. Fuls, E. N. Reactively Sputtered Vanadium Dioxide Thin Films. *Appl. Phys. Lett.* **10,** 199 (1967).

79. Sambi, M., Sangiovanni, G. & Granozzi, G. Growth and the structure of epitaxial VO_2 at the TiO2 (110) surface. **55,** 7850–7858 (1997).

80. Muraoka, Y. & Hiroi, Z. Metal–insulator transition of VO_2 thin films grown on TiO_2 (001) and (110) substrates. *Appl. Phys. Lett.* **80,** 583 (2002).

81. Azrak, R. G. & Angell, C. L. Study of Alcohol-Silica Surface Reactions via Infrared Spectroscopy. *J. Phys. Chem.* **77,** 3048–3052 (1973).

82. Maki, H., Sato, T. & Ishibashi, K. Direct observation of the deformation and the band gap change from an individual single-walled carbon nanotube under uniaxial strain. *Nano Lett.* **7,** 890–5 (2007).

83. Wei, B. *et al.* Size-dependent bandgap modulation of ZnO nanowires by tensile strain. *Nano Lett.* **12,** 4595–9 (2012).

84. Lugstein, a, Steinmair, M., Steiger, a, Kosina, H. & Bertagnolli, E. Anomalous piezoresistance effect in ultrastrained silicon nanowires. *Nano Lett.* **10,** 3204–8 (2010).

85. Wu, B., Kumar, A. & Pamarthy, S. High aspect ratio silicon etch: A review. *J. Appl. Phys.* **108,** 051101 (2010).

86. Laermer, F. & Urban, A. Challenges , developments and applications of silicon deep reactive ion etching. **68,** 349–355 (2003).

87. Jones, R. V. Some developments and applications of the optical lever. *J. Sci. Instrum.* **38,** 37–45 (1961).

88. Jones, A., Park, J. H., Coy, J., Cobden, D. & Xu, X. Ultrafast Spectroscopy and Optically-Induced Phase Transitions of Single Crystal VO2. in *APS March Meet.* (2012). at <http://meetings.aps.org/link/BAPS.2012.MAR.D5.6>

89. Dean, C. R. *et al.* Boron nitride substrates for high-quality graphene electronics. *Nat. Nanotechnol.* **5,** 722–6 (2010).

90. Fisher, B. Moving boundaries and travelling domains during switching of VO_2 single crystals. *J. Phys. C Solid State Phys.* **8,** 2072–2076 (1975).

91. Minomura, S. & Nagasaki, H. The Effect of Pressure on the Metal-Insulator Transition in VO_2 and V_2O_3. *J. Phys. Soc. Japan* **19,** 131–132 (1964).

92. Kawakubo, T. & Nakagawa, T. Phase Transition in VO_2. *J. Phys. Soc. Japan* **19,** 517–519 (1964).

93. Sasaki, H. & Watanabe, A. A New Growing Method for VO_2 Single Crystals. *J. Phys. Soc. Japan* **19,** 1748 (1964).

94. Rosevear, W. H. & Paul, W. Hall Effect in VO_2 near the Semiconductor-to-Metal Transition. *Phys. Rev. B* **7,** 2109–2111 (1973).

95. Jeong, J. *et al.* Suppression of metal-insulator transition in VO_2 by electric field-induced oxygen vacancy formation. *Science* **339,** 1402–5 (2013).